ANDREA SÁNCHEZ FERNÁNDEZ | Microstructural evolution analysis during the Near Solidus Forming process: the case of AISI 316

Mondragon Unibertsitatea

DOCTORAL THESIS

MICROSTRUCTURAL EVOLUTION ANALYSIS DURING THE NEAR SOLIDUS FORMING PROCESS: THE CASE OF AISI 316

ANDREA SÁNCHEZ FERNÁNDEZ | Arrasate-Mondragón, 2023

Microstructural evolution analysis during the Near Solidus Forming process: the case of AISI 316

Mechanics and Industrial Production Department

Mondragon Unibertsitatea
Goi Eskola Politeknikoa
Faculty of Engineering

To obtain the title of

DOCTOR IN APPLIED ENGINEERING

Presented by

ANDREA SÁNCHEZ FERNÁNDEZ

Supervised by

DR. IÑAKI HURTADO,
DR. CARL SLATER AND DR. GORKA PLATA

In ARRASATE in 2022

"The roots of education are bitter, but the fruit is sweet."

— Aristotle

A ti Andrés, por haber siempre creído en mí.

DECLARATION OF ORIGINALITY

Hereby I, Andrea Sánchez Fernández, declare, that this paper is my original authorial work, which I have worked out by my own. All sources, references and literature used or excepted during elaboration of this work are properly cited and listed in complete reference to the due source.

Yo, Andrea Sánchez Fernández declaro que esta tesis doctoral es original, fruto de mi trabajo personal, y que no ha sido previamente presentado para obtener otro título o calificación profesional. Las ideas, formulaciones, imágenes, ilustraciones tomadas de fuentes ajenas han sido debidamente citadas y referenciadas.

Arrasate, 2022

LABURPENA

Fabrikazio-prozesuen gaur egungo joera, piezak fabrikatzeko egin beharreko urratsak murriztea eta erabilitako lehengaiak gutxitzea du helburu. Horretarako, altzairua bezain fusio-puntu altuko aleazioekin prozesu berri bat definitu da Near Solidus Forming (NSF), prozesu erdi-solidoen baitan dagoena. Altzairuzko pieza konplexuak teknika honen bidez fabrikatu dira, forja bidez lortzen diren antzeko propietate mekanikoak lortuz, beharrezko urratsak bakar batera eramatea lortuz eta beraz, energia eta lehengaien kontsumoa murriztuz. Lan honetan, NSF prozesua industrian asko erabiltzen den AISI 316 altzairuarentzat aztertu da.

Arlo honetan egindako aurrerapenez gain, oraindik ez dira ezagutzen portaera honen arrazoiak, eta hau da lan honen zergatia. Lehenik eta behin, materiala termomekanikoki karakterizatu da NSF prozesuaren adierazgarri diren baldintzetan. Analisi honek altzairu herdoilgaitz austenitikoaren portaera solidus egoeratik gertu dauden tenperaturetan aldatzen dela frogatu du. Solidus tenperatura DSC analisiaren bidez zehaztu da, hau 1435°C-koa izanik eta FactSage simulazioaren bidez lortutakoarekin bat eginez. Adibidez, aktibazio-energia literaturan agertzen denaren gertu egon arren, delta ferrita formazioaren ondorioz %20 altuagoa izango dela ezarri da, rekristalizazio prozesua oztopatu dela adieraziz. Gainera, NSF baldintzak kontuan hartuta Hansel-Spittel ekuazioaren bidez lortutako tentsio-deformazio portaera optimizatu da, iragarpenen errorea erdira murriztuz. Era berean, rekristalizazioa gertatzen dela frogatu da, ale-tamaina txikiagoko piezak lortzea ahalbidetuz, nahiz eta delta ferrita sortu. DSC analisiek delta ferrita 1410°C-tik aurrera agertzen dela jakinarazten duten arren, oreka-baldintzarik gabe, delta ferrita 1300°C-tik gora agertzen dela frogatu da. Honek, piezaren propietate mekanikoetan eragiten du, mikrogogortasun neurketak frogatu duten bezala.

Prozesuaren simulazioari dagokionez, literaturan dauden legeak NSF baldintzetara arte estrapolatzeak huts egiteko joera duela frogatu da, materialaren portaera aldatzen baitoa solidus tenperaturara hurbiltzen den heinean. Espero zitekeenaren aurka rekristalizatutako aleen tamainak tenperaturarekin baldintza estandarretan (NSF) ia konstante mantentzen direla ikusi da, delta ferritak nahiko denbora baitu austenita aleen mugetan metatzeko. Bukatzeko, altzairu herdoilgaitzezko pieza konplexuak fabrikatzeko NSF prozesuaren gaitasuna aztertu da. Horretarako osagai jasotzaile bat fabrikatu da solidus tenperaturatik gertu. Jakina denez delta ferrita kaltegarria izan daitekeela amaierako piezaren propietateentzat, bi tenperatura ezberdin frogatu dira. Ondorioz, altzairu herdoilgaitzezko piezak fabrikatzean nahi den amaierako mikroegitura lortzeko NSF prozesua erabiliz, tenperatura ez ezik, berotze abiadura ere faktore garrantzitsua dela egiaztatu du ikerketa honek.

ABSTRACT

The current trend in manufacturing processes aims for the reduction of steps and the decrease of raw material used. In order to achieve this with high melting point alloys such as steels, a new process was defined under the umbrella of semi-solid called Near Solidus Forming (NSF). Complex steel parts have been manufactured by using this technique, obtaining similar mechanical properties to forged material, reducing the number of steps to one and decreasing both energy and raw material consumption. In this work, the process was analysed for AISI 316 a widely used steel in industry.

Despite the advances made in this field, the reasons which explain the behaviour are still unknown, thus defining the scope of this work. First, the material was thermomechanically characterized under the conditions representative of the NSF process as a noticeable gap was observed in the literature, proving that material behaviour of austenitic stainless steel changes at temperatures close to the solidus. The solidus temperature was determined using DSC analysis to be 1435°C, the results being in agreement with those reported through FactSage simulation. For instance, although the activation energy was close to the one reported in the literature, it was set to be around 20% higher due to delta ferrite formation, meaning that recrystallization was hampered. In addition, flow stress behaviour according to the Hansel-Spittel equation was optimized taking into account NSF conditions, reducing error in the predictions by more than half.

Also, recrystallization was proven to occur allowing the obtention of parts with smaller grain sizes despite delta ferrite formation. Although the DSC analysis reported that delta ferrite tended to appear at temperatures around 1410°C for this alloy, under no equilibrium conditions, it was demonstrated that delta ferrite appeared at temperatures over 1300°C, influencing the mechanical properties as was proven through microhardness measurements.

Regarding the simulation of the process, it was demonstrated that extrapolation using the existing laws in the literature up to NSF conditions tended to fail as material behaviour changes at temperatures close to the solidus. In contrast to what might have been expected, recrystallized grain sizes remained almost constant with temperature under commercial conditions, as delta ferrite had enough time to nucleate along austenite grain boundaries.

Finally, the capacity for the NSF process in manufacturing complex stainless steel parts was established by manufacturing a lifting gear component. However, delta ferrite is known to be detrimental to the properties of the final part, that is why two different temperatures were tested. It was demonstrated that not only the temperature but the heating rate are also important factors in obtaining the desired microstructure in the final part when manufacturing stainless steel parts using the NSF process.

RESUMEN

La tendencia actual en los procesos de fabricación busca reducir las etapas y la materia prima utilizada. Para aleaciones de alto punto de fusión, como los aceros, se definió un nuevo proceso denominado *Near Solidus Forming* (NSF). Mediante este proceso se han fabricado piezas complejas de acero, obteniendo propiedades mecánicas similares a las de la forja, en una sola etapa y disminuyendo tanto el consumo de energía como el de materia prima. El material analizado ha sido un acero inoxidable austenítico, el AISI 316, de gran relevancia en la industria.

A pesar de los avances realizados en este campo, aún se desconocen las razones que explican su comportamiento, definiendo así el alcance de este trabajo. En primer lugar, se caracterizó termomecánicamente el material en las condiciones representativas del proceso NSF, ya que se observó un *gap* en la bibliografía, demostrando que el comportamiento del material cambia a temperaturas próximas al *solidus*. La temperatura de solidificación se determinó mediante análisis DSC, siendo 1435°C, y los resultados coinciden con los obtenidos mediante simulación en FactSage. Por ejemplo, aunque la energía de activación era próxima a la indicada en la bibliografía, se obtuvo un valor aproximadamente un 20% superior debido a la formación de ferrita delta, lo que significa que la recristalización se vio dificultada. Además, se optimizó el comportamiento de la ley de fluencia según la ecuación de Hansel-Spittel, teniendo en cuenta las condiciones de NSF, reduciendo el error de predicción más de la mitad.

Asimismo, se comprobó que tenía lugar la recristalización, lo que permite obtener piezas con tamaños de grano pequeños a pesar de la formación de ferrita delta. Aunque el análisis DSC reportó que la ferrita delta tendía a aparecer a temperaturas en torno a 1410°C, en condiciones de no equilibrio, se demostró que la ferrita delta se forma a temperaturas superiores a 1300°C, influyendo en las propiedades mecánicas, como se comprobó mediante medidas de microdureza.

En cuanto a la simulación del proceso, se demostró que la extrapolación utilizando las leyes existentes en la bibliografía hasta las condiciones de NSF fallaba, ya que el comportamiento del material cambia a temperaturas cercanas al *solidus*. A diferencia con lo que cabría esperar, los tamaños de grano recristalizados se mantuvieron casi constantes con la temperatura a las condiciones comerciales (NSF), ya que la ferrita delta tuvo tiempo suficiente para nuclearse a lo largo de los límites de grano.

Por último, se demostró la capacidad del proceso NSF para fabricar un gancho elevador con acero inoxidable. Sin embargo, la ferrita delta es perjudicial para las propiedades mecánicas de la pieza final, por lo que se realizaron pruebas a dos temperaturas diferentes. Se demostró que no sólo la temperatura, sino también la velocidad de calentamiento, son factores importantes para obtener la microestructura deseada en la pieza final cuando se fabrican piezas de acero inoxidable mediante el proceso NSF.

GLOSSARY

T_{m}	Melting temperature (°C)
σ	True Stress (MPa)
σ_{c}	Critical Stress (MPa)
σ_{p}	Peak Stress (MPa)
σ_{s}	Steady-State Stress (MPa)
ε	True Strain
ε_{c}	Critical Strain
ε_{p}	Peak Strain
ε_{s}	Steady-State Strain
$\dot{\varepsilon}$	Strain rate (s^{-1})
Q	Activation energy (J/mol)
R	Gas constant ($\mathrm{J}/(\mathrm{mol} \cdot \mathrm{K})$)
α, β, b, n, A	Material constants
D_0	Initial grain size (µm)
d_{DRX}	Dynamic recrystallized grain size (µm)
k	Avrami material constant
$n^{'}$	Avrami exponent
X	Recrystallized volume fraction
θ	Work hardening rate (MPa)
T_{set}	Set temperature of the furnace (°C)
T_{th}	Thermocouple temperature (°C)
t	Time (s)
F	Force (N)
h_0	Initial height of the sample (mm)
d	Compressive displacement (mm)
ϕ_0	Initial diameter of the sample
η	Triaxiality parameter
p	Hydrostatic pressure (MPa)
q	Equivalent stress (MPa)

Z	The Zener-Hollomon parameter
t_{50}	The time for 50% softening (s)

NSF	Near Solidus Forming
SSM	Semisolid Metal
SSP	Semisolid Forming Processes
PSCT	Plane Strain Compression Test
RX	Recrystallization
SRX	Static Recrystallization
DRX	Dynamic Recrystallization
dDRX	Discontinuous Dynamic Recrystallization
cDRX	Continuous Dynamic Recrystallization
MDRX	Metadynamic Recrystallization
DRV	Dynamic Recovery
SFE	Stacking Fault Energy
DSC	Differential Scanning Calorimetry
TDC	Top Dead Centre
GRG	Generalized Reduced Gradient
FEM	Finite Element Method
SEM	Scanning Electron Microscope
EBSD	Electron Backscatter Diffraction
KAM	Kernel Average Misorientation
XRF	X-ray Fluorescence

ACKNOWLEDGEMENTS

Aunque parezca mentira, toda etapa, por bonita que sea, llega a su fin para abrir paso a nuevos retos y es el momento de agradecer a todas aquellas personas que han compartido este camino.

En el ámbito personal, a mis padres María José y Germán por haberme apoyado desde pequeña y no haberme dejado rendirme ante ningún reto, ya que gracias a ellos hoy soy quien soy. A mi hermana pequeña Lucía, que siempre ha estado a mi lado a pesar de nuestras riñas y enfados. A mis abuelos por su ayuda y haber soportado la distancia. También a Ascen y Domi.

Gracias a todos los compañeros de MU por haber estado ahí en todo momento, tanto para celebrar los logros alcanzados como para arrimar el hombro. Gracias a los desayunos en Ogi-Berri, ese *Lunch Time* con Aurea, Ainara, Laura y David. También a las comidas en Garaia con el *Ekipo Machining* y nuestras charlas distendidas en el Urrin con un café (con su bien de piedra de hielo). Destacar el apoyo emocional aportado por *les Flojes*, Gorka, Maitane, Xabi LZK, Sandra, Asier y Ainhoa ya fuese en Vitoria, Donosti, Jaca o Asturies. No olvidaré nunca la práctica de deporte regional (picar piedra) hasta en mi boda.

Por supuesto, no me olvido de los momentos de ofi en Garaia y las largas y laboriosas tardes/noches de producción de piezas de NSF vestidos de astronauta. Aquí, hacer mención especial a mis directores (uno de ellos con adopción tardía), Iñaki y Gorka, y a una persona especial que me hizo adentrarme en el mundo NSF y que se ha echado de menos, JLA. Dentro del grupo destacar a mis compañeros Juanjo, Pablo, Xabi, Olaia y Sajjad, que han hecho los días más sencillos por la ofi. Además, destacar el compañerismo de Dani, que sabiendo todos los problemas ajenos (COVID y Brexit), me facilitó siempre la realización de ensayos.

I don't forget about my supervisor Dr. Carl Slater who accompanied and supported me during these three years. Also, I would want to acknowledge the accommodation during the time I was in Warwick although, due to COVID and Brexit, it could not be as long as we would want but it was so profitable. Apart from the academic part, I will never forget the barbecue (with special mention to the grilled corn) and my sportive skills playing squash, so enjoyable!

No me quiero olvidar del profesor de la Universidad de Oviedo que me habló de MU y gracias al cual hoy estoy aquí, así como, a los profesores del máster y al servicio de secretaría académica al que hemos mareado todo el tiempo.

Por último, pero no menos importante, a ti, Andrés. Por el apoyo, tanto emocional como académico, no sé quien tenía más ganas de que terminase si tu o yo! Bromas a

parte, poco puedo decir que no te haya dicho, pero espero que sigamos compartiendo este camino para repetírtelo.

CONTENTS

LIST OF FIGURES

LIST OF TABLES

1

INTRODUCTION

In many countries the industrial sector represents more than 50% of the primary energy use and, likewise, more than 50% of CO_2 emissions. Within the industrial sector, iron and steel production represents one of the main sources of energy consumption (Price et al., 2002).

As Figure 1.1 shows, the global tendency of steel demand is increasing day by day. For instance, it was close to one billion tonnes in 2005 whereas in 2015 it increased to 1.5 billion tonnes (Nidheesh and Kumar, 2019).

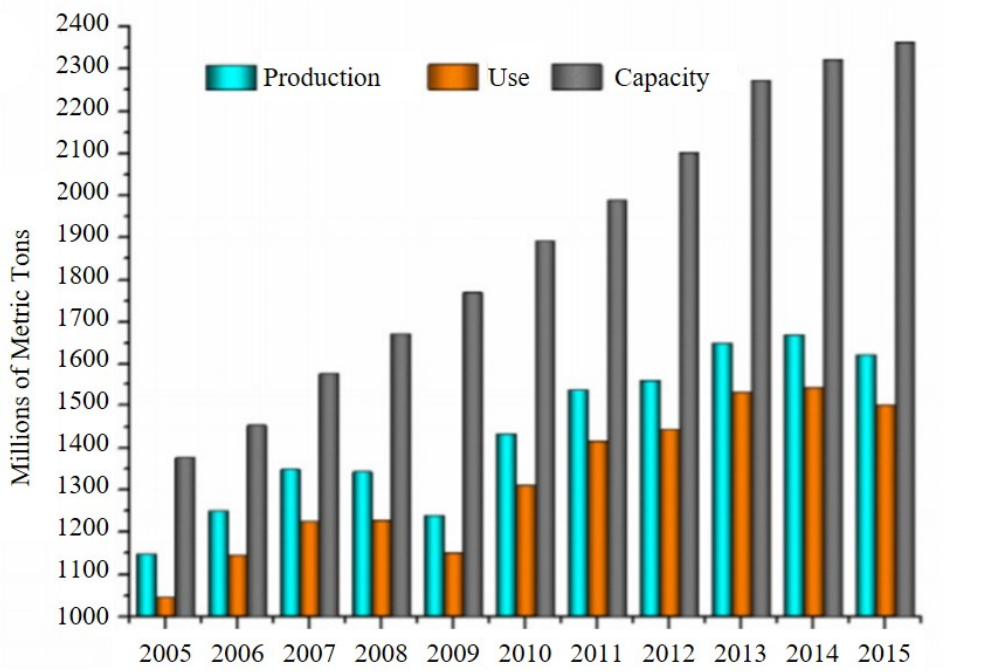

Figure 1.1: Tendency on steel production between 2005 and 2015 (Nidheesh and Kumar, 2019)

Environmental sustainability of the primary industry is a global challenge. Nevertheless, mechanical industry is usually characterized by high energy consumption, high waste rates, low production efficiencies and high level of emissions. For instance, processes such as casting, forging and heat treatments represent around 60-80% of all the energy consumption (Shan et al., 2012). In addition, flash and poor surface finishing require a final machining operation which increases product waste. Machining operations

represent, every year, 100 million tonnes of wasted metal which translates to 250 billion dollars (Shan et al., 2012).

Moreover, to try to reduce global emissions, other materials like light metals or composites are used in aerospace, military applications and in the automotive industry. For instance, new materials could improve the performance of aircraft and aircraft engines by 70% and their weight could be reduced by up to 80% (Shan et al., 2012).

In this aspect, it is noted that manufacturing processes are responsible for high levels of energy consumption, so addressing this problem should be a priority. Also, material waste is another relevant issue to be looked into.

In this sense, Semi-Solid Forming Processes (SSP) could be a possible choice to solve or, at least, reduce these problems. SSP represents a family of innovative techniques in which liquid and solid material coexist. This implies that this option falls between traditional casting and forging processes (Kirkwood, 1994). As a consequence, after the application of a shear stress to the semi-solid state particles lower process loads are employed. These techniques allow complex-shape parts to be manufactured in one step by reducing energy costs and minimizing raw material consumption (Lozares et al., 2020).

1.1 MOTIVATION

Consequently, in recent decades researchers from Mondragon University have studied the semi-solid process. The first attempts were carried out considering thixoforming, with a special focus on aluminium alloys (Azpilgain et al., 2006; Blanco et al., 2010) due to their low melting point and their relevance to industry thanks to their low density.

Thixoforming routes were proven to be able to properly manufacture aluminium parts. Following this research line Lozares et al., 2020 proposed a novel process under the umbrella of semi-solid called Near Solidus Forming (NSF) which is carried out at high temperatures close to the solidus. The main aim of this process is to obtain parts assuring as forged mechanical properties while saving energy and reducing the raw material. In addition, it was proven to be a real competitor to traditional hot forging, demonstrated great potential to reduce manufacturing costs. NSF provides the possibility of achieving complex geometries in a single step even with austenitic stainless steel. Among all stainless steels, austenitic stainless steel represents more than 65% (Koç, Mahabunphachai, and Billur, 2011).

The first attempt to analyse NSF was made by Plata, 2018. He studied possible phenomena which could explain NSF behaviour. The incipient melting phenomenon was studied to analyse the generation of liquid during deformation. Moreover, through compression and tensile tests a softening effect was noted which could allow the grain decohesion. This could be explained by the presence of sulphur which forms MnS sulphides. After the analysis, it was established that sulphur content and incipient melting could influence steel deformation without being the principal reason.

In spite of the great potential shown by NSF there is still a clear lack of knowledge about how or why the NSF process works. To fill this gap, NSF studies should be focused more deeply on the material being deformed, analysing different possibilities such as microstructural changes, material behaviour and recrystallization. Therefore, it is necessary to carry out a comprehensive study of the material in terms of microstructure and flow behaviour. As the materials used in previous investigations had microstructural changes induced during the process, they were difficult to analyse. The heating and cooling of the initial billet may cause phase changes which do not facilitate the understanding of the process.

Thus, the present study shows an in depth analysis of the material behaviour of austenitic stainless steel subjected to extreme hot working conditions representative of the NSF process. In addition, possible restoration mechanisms such as recrystallization were analysed as they could have a relevant influence on the microstructure of the manufacturing part and, thus, on the mechanical properties of this part. This scientific knowledge has been employed to predict the mentioned microstructure in a real industrial part of austenitic stainless steel manufactured following the NSF route.

1.2 STRUCTURE OF THE DOCUMENT

This document is organized as follows:

- *Chapter 2-Literature review*

  A summary and critical analysis of the main research work from a general point of view is set out, including the discussion of these references and the identification of the research opportunities. These research opportunities define the objectives.

- *Chapter 3-Objectives*

  The general aim is summarized in this chapter together with all the research objectives addressed during this research work

- *Chapter 4-Methodology*

  Different experimental devices were employed to carry out this research. For instance, thermomechanical characterization was done through dilatometer and Gleeble tests, together with a DSC characterization and furnace trials. The NSF cell is also explained and the preliminary numerical analysis is shown.

- *Chapter 5-Thermomechanical behaviour of AISI 316*

  First, DSC analysis is used to determine the solidus temperature. Then, the influence of temperatures, strain rates and heating profile is analysed in order to provide a more in-depth knowledge of the material behaviour and to optimize Hansel-Spittel

law to increase the accuracy on the predictions. Finally, flow stress curves are employed to determine the onset for DRX initiation, results validated in the following chapter.

- *Chapter 6-Recrystallization analysis*

  The material was firstly thermo-physically characterized to measure grain growth kinetics. Then, the possible transition between DRX and MDRX regimes was studied. The analytical measurements were validated by using optical microscope and Electron Backscatter Diffraction (EBSD). Recrystallized grain sizes were measured and compared with literature results, proving the necessity of characterizing the material under these conditions.

- *Chapter 7-Lifting gear component analysis*

  The capability of the NSF process of manufacturing stainless steel parts was deeply analysed from experimental results (loads, material filling into the dies) to microstructural observations, together with numerical simulations.

- *Chapter 8-Conclusions*

  The conclusions of this study are summarized in this chapter.

- *Chapter 9-Future lines*

  New questions arisen after all the research work, that is why this chapter summarizes some perspectives for further research.

- *Chapter 10-Possibilities of the NSF process*

  The possibilities of the NSF process to manufacture other complex geometries with stainless steel and bimetal parts were analysed.

The document structure is summarized in Figure 1.2.

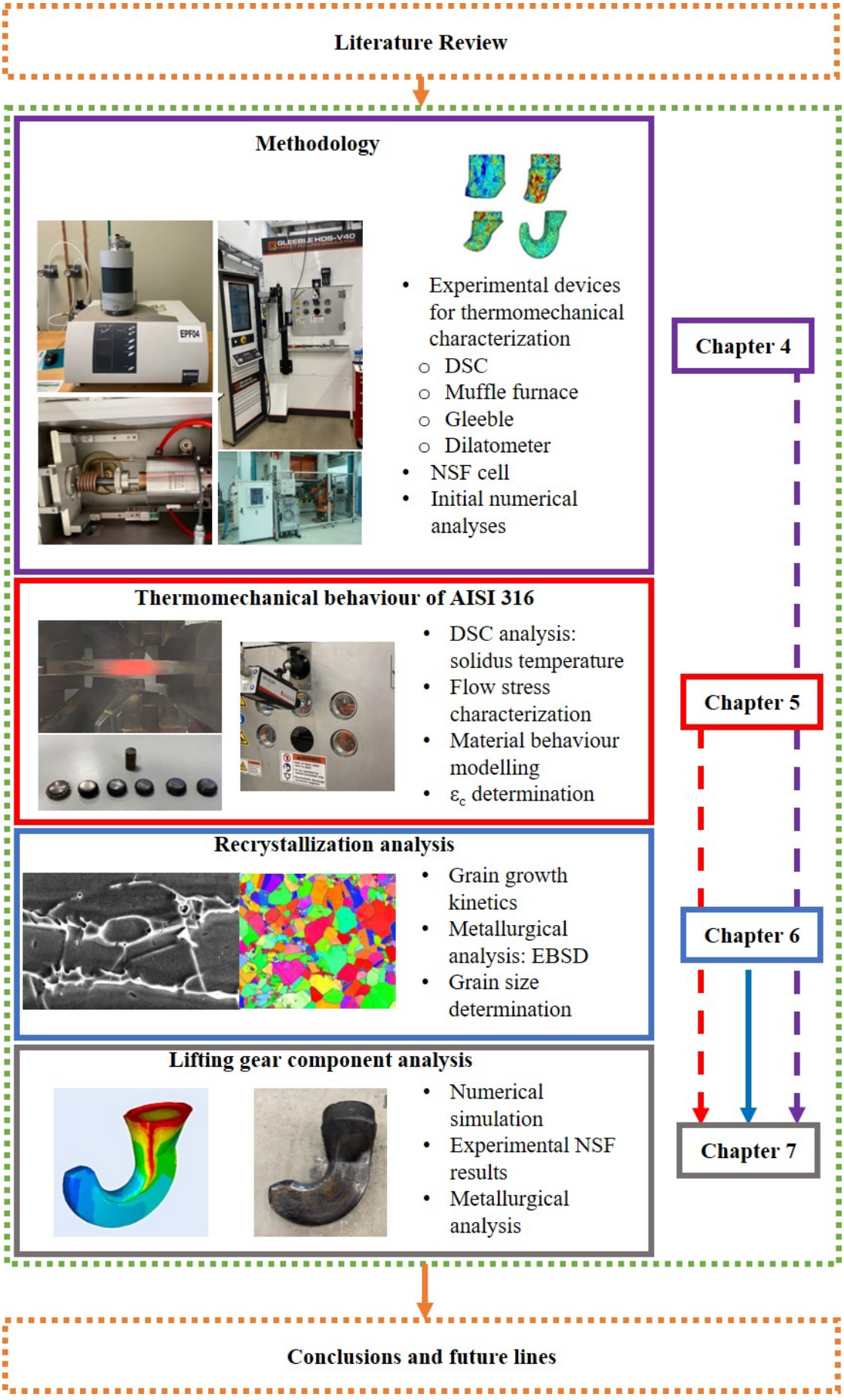

Figure 1.2: Dissertation structure

2

LITERATURE REVIEW

Hot processes are usually divided into two main groups, hot forging-like processes or casting-like processes. Hot forging is commonly chosen in order to ensure good mechanical properties whereas casting-like processes are capable of manufacturing more complex parts.

Near Solidus Forging (NSF) is a novel process under the umbrella of semi-solid processes which works at temperatures near the solidus obtaining properties similar to those obtained in hot forging. However, in spite of the great potential of this novel process, it is necessary to understand the reasons why this process works. The NSF process was able to take the advantages from the above mentioned techniques as was proven by Lozares et al., 2020 and Plata et al., 2020.

Therefore, during this chapter, hot forging and semi-solid processes have been analysed highlighting the differences between these traditional processes and the novel NSF process. These differences open a gap to research because of the extreme conditions under which the material is subjected during this process.

First, it would be of great interest to understand the material behaviour under these extreme conditions. Although material behaviour is one of the most widely studied issues related to forming processes, the conditions usually reached in the literature are still far from those.

Then, due to the high temperature and strain at which the material is exposed, different restoration processes could take place such as dynamic recovery or recrystallization. Among all, recrystallization would be the desired one as it allows microstructures with small grain sizes to be obtained. This is assumed to be beneficial for the mechanical properties of the final part. Therefore, an in depth analysis of recrystallization processes was carried out.

Finally, as it was mentioned in Chapter 1, austenitic stainless steel is of great interest to be studied not only for its industrial relevance but also for the absence of phase changes which could facilitate the analysis. Nevertheless, although there is a vast amount of research studying flow behaviour under hot working conditions for this family of materials, there is a lack of studies focused on the extreme conditions under which the NSF process works.

2.1 THE NSF PROCESS

The Near Solidus Forming process is a new manufacturing technique which presents some characteristics in common with the hot forming processes. For instance, depending

on process temperature, different forming processes can be defined. Cold forming works between room temperature and $0.25T_m$ (T_m being the melting temperature) the formability usually being low and, thus, the forces needed higher, manufacturing small parts. Warm forming is carried out at temperatures between 0.25 to 0.6 times T_m, manufacturing final parts which do not exceed 50 kg. Then, hot forming works at temperatures in the range of 0.6 to $0.87T_m$ (Douglas and Kuhlmann, 2000), requiring low forming forces and allowing heavy final parts to be obtained (Mohanty, 2017). The typical temperatures used in hot forming for the different alloys are shown in Table 2.1 and the forgeability of different alloys is also shown in Figure 2.1. However, the NSF process works at very high temperatures (around 0.95 times the solidus temperature as stated Lozares et al., 2020).

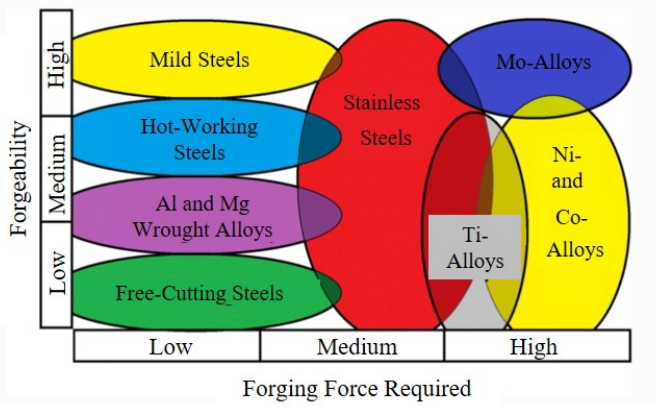

Figure 2.1: Forgeability and forces for different materials (Adapted from Bell et al., 2019)

Table 2.1: Temperature range for metals and alloys in hot forming (Rathi and Jakhade, 2014)

Metal or alloy	**Temperature Range (°C)**
Aluminium alloys	400-550
Magnesium alloys	250-350
Copper alloys	600-900
Carbon and low-alloy steels	850-1150
Martensitic stainless steels	1100-1250
Austenitic stainless steels	1100-1250
Titanium alloys	700-950
Iron-base superalloys	1050-1180
Cobalt-base superalloys	1180-1250
Nickel-base superalloys	1050-1200

Lozares et al., 2020 designed the equipment to carry out NSF tests (see Figure 2.2). In addition, they demonstrated the capacity for the process in manufacturing steel components (high-melting point alloys). This process, in comparison with hot forging, presents different advantages such as the decrease of the amount of material wasted and a reduction in energy consumption as summarizes Table 2.2.

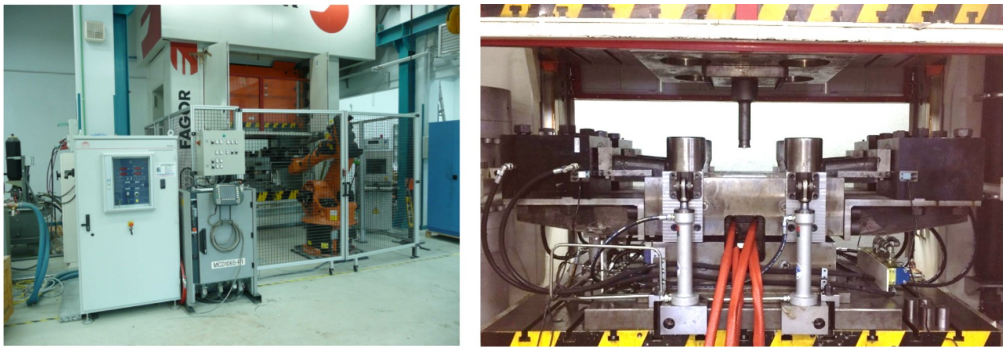

(a) (b)

Figure 2.2: (a) NSF cell (b) NSF tooling designed for high-melting-point alloys (Lozares et al., 2020)

Table 2.2: Comparison between traditional hot forging and the novel NSF process for two different industrial components (Adapted from Lozares et al., 2020)

Component	Process	Steps	Press Capacity (t)	Peak Force (t)	Material (kg)
C.1	HF	$3+1$	2500	1200	3.5
C.1	NSF	1	400	300	2.8
C.2	HF	$3+1$	3500	2100	3
C.2	NSF	1	400	280	2.4

A complex geometry was manufactured to demonstrate the capacity for the process. NSF only needed a single step to manufacture it whereas three steps were necessary in traditional hot forging as well as one flash removal operation (see Figure 2.3).

However, in spite of all the progress made in the past and all the advantages shown by the NSF process, different gaps have been identified (Plata, 2018). The material behaviour under the extreme conditions employed in the process is still far to be perfectly understood as it will be further analysed in this chapter. In addition, although the process has been proven to successfully work with high melting point alloys as steels, there is not a clear optimum window. To define it, it will be necessary to take into account not only filling capability (mechanical issues) but also how material behaves under NSF conditions in terms of microstructural issues.

On this basis, the heating process is key to ensure process performance. It can be done by gas, electrical or induction and is an important parameter to be controlled as it

Figure 2.3: (a) classical hot forging (b) NSF process in the case of a H spindle geometry (Lozares et al., 2020)

can cause defects such as overheating or burning during the forging process (Douglas and Kuhlmann, 2000; Nisbett, 2005). Temperature increase results in a decrease in strength and the load required to deform the material, while ductility increases. However, at high temperatures grain size tends to increase causing a decrease in mechanical properties. This behaviour is known as overheating (see Figure 2.4) and it should be controlled to increase die life (Douglas and Kuhlmann, 2000).

Another typical defect in hot forging is burning. It is characterized by a substantial growth in grain size and grain boundary oxidation. This damage is total and permanent, the steels losing their ductility during deformation (Nisbett, 2005).

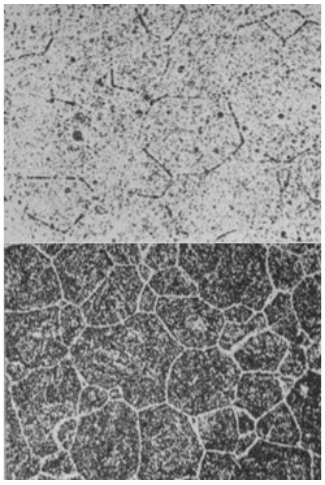

Figure 2.4: Overheated steel (Adapted from Tsun, 1953)

Other relevant consideration lie in die design to improve the quality of the final part. An inappropriate geometry or a badly positioned billet (Hawryluk and Jakubik,

2016) could lead to high production costs due to the presence of flash and other defects generated, such as underfills or folds (as shown in Figure 2.5).

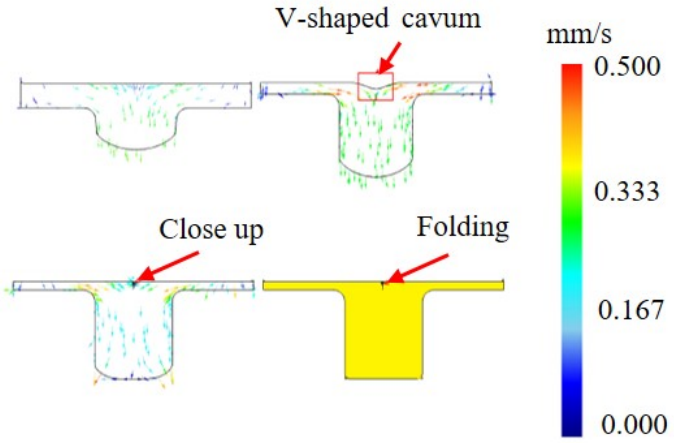

Figure 2.5: Speed distribution and defects (Adapted from Gao et al., 2019)

To overcome the generation of these defects, NSF has been proven to be a potential technique when the optimum process parameters are chosen for each material as stated by Plata et al., 2020. An example of a complex geometry manufactured through NSF without observable defects is shown in Figure 2.6.

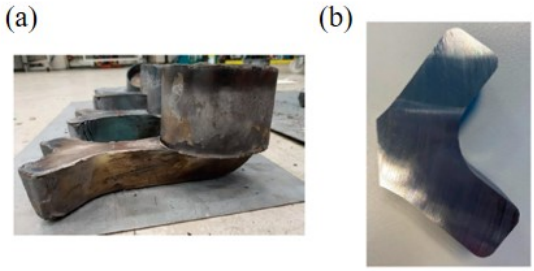

Figure 2.6: Examples of NSF components: (a) Cup part completely filled, (b) Slice of the part (Adapted from Plata et al., 2020)

To conclude, it is worth noting that a reduction in energy consumption, manufacturing cost and raw material wasted was achieved. It was demonstrated that NSF is capable of producing complex geometries in a single step, demonstrating its great potential. In addition, the forces needed were substantially lower than in traditional hot forging. Nevertheless, despite the great potential shown by the process, further research is needed to understand why and how the process works. That is why, first an overview about semisolid and hot forging processes was carried out as their were proven to show similarities with the NSF process.

2.2 SEMI-SOLID

As has been previously stated, the idea of NSF was born from semisolid studies. That is why, this behaviour was deeply analysed in the past as a possible reason to explain why NSF process works. Therefore, even if Plata, 2018 concluded that metal alloys behave closer to a solid way, it would be necessary to analyse this process to completely understand the reasons which lead the NSF process to work.

The beginning of semi-solid metal forming was studied by Spencer, Mehrabian, and Flemings, 1972. They studied semi-solid behaviour carrying out viscosity experiments related to hot tearing in Sn- Pb alloys. The material behaved as a liquid when shear forces were applied and, after enough time, it thickened again (Fan, 2002). Figure 2.7 describes these flow characteristics.

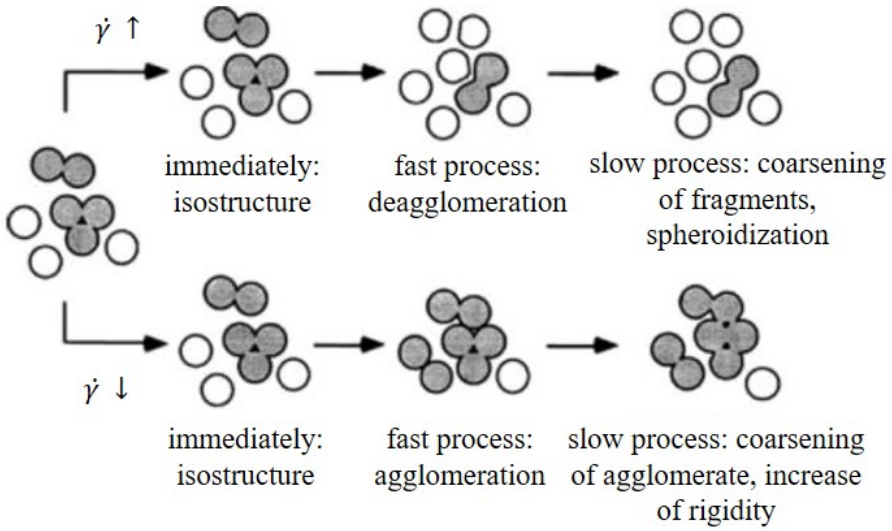

Figure 2.7: Schematic model describing the fast and slow processes in a semi-solid material after shear rate up and down jumps (Adapted from Plata, 2018)

There are two types of semi-solid metal forming processes called rheo-routes and thixo-routes. Rheo-routes involve the preparation of material from liquid phase (Flemings, Riek, and Young, 1976; Flemings, 1991 and Nafisi and Ghomashchi, 2016). This requires a non-dendritic SSM slurry. Then, metal alloys are stirred during solidification and are transferred to the die. This process requires specific equipment to cool and stir at the same time which results in a high cost. In the case of thixo-routes, a three-step process is needed to work, involving material preparation with equiaxed or globular microstructure, reheating the material to temperatures between solidus and liquidus and final forming (Nafisi and Ghomashchi, 2016).

Depending on the liquid fraction, semi-solid metal forming processes can be classified into casting and forging. When the liquid fraction is approximately 50%, the process is

close to casting, but if the liquid fraction is lower, the process is close to forging. The high liquid content could result in porosity due to turbulent mould filling (Becker et al., 2010). In Figure 2.8 different types of semisolid processes, depending on the component's geometrical complexity, are shown.

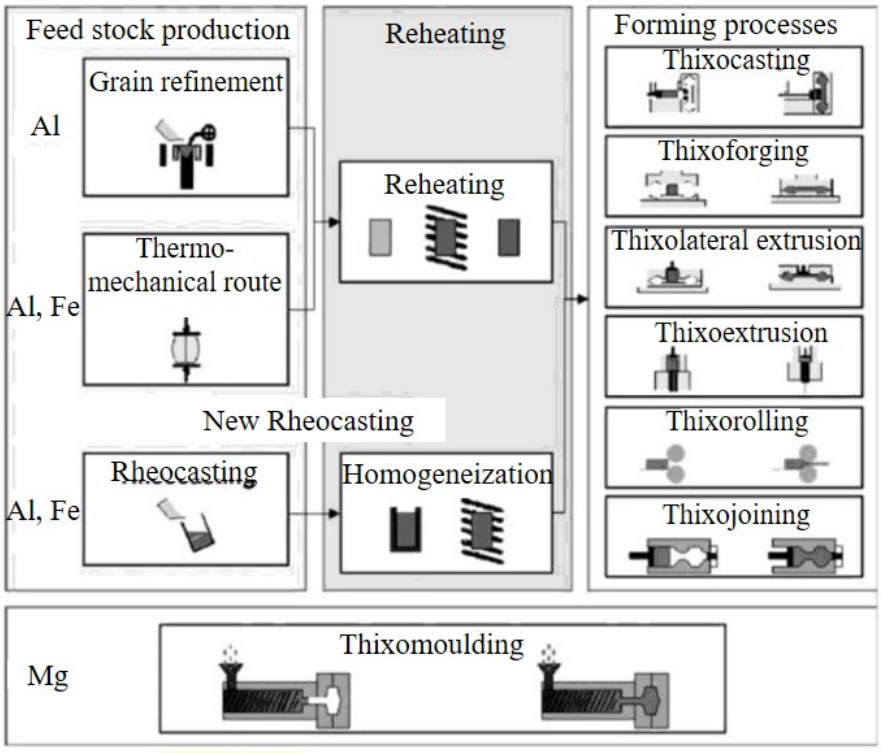

Figure 2.8: Different types of SSM processes (Adapted from Hirt and Kopp, 2009)

During the first stages of the semi-solid forming, only low melting point alloys were studied. In the middle of 1990s, thixoforming became the focus of research after demonstrating the feasibility of manufacturing steels. Kapranos, Kirkwood, and Sellars, 1993 and Hirt and Kopp, 2009 developed thixoforged parts with a complex geometry using steel, in the first attempt with high solid fraction. These high melting point alloys presented difficulties due to the high temperature range, such as appropriate tools, the heating technology and the process control (Hirt and Kopp, 2009). However, it was attractive due to the low forging force involved, the complex shapes with less forming steps in production or manufacturing components with less porosity (Omar et al., 2005). Different research into mechanical properties and heat treatments concluded that thixoforged cog wheels made from a M2-tool steel had better mechanical properties than the same material from traditional routes (Kapranos, Kirkwood, and Sellars, 1993 and Puettgen et al., 2007).

Semi-solid forming, as stated above, has several advantages over traditional forming processes such as its performance and mechanical properties. However, it should be noticed that there are some processing parameters that must be controlled to reduce or eliminate defects in the final component.

For instance, for high liquid content, the effect of piston velocity leads to the production of turbulent flow because of high speed. Turbulent flow results in porosity formation. Piston speed could be decreased to avoid this type of defect (Moradi et al., 2009). However, Cho and Kang, 2000 observed internal defects in semi-solid processes which may have an effect on mechanical properties, such as porosity in the case of lower die temperatures. These problems may be solved by using higher injection speeds (Cho and Kang, 2001).

Another parameter which may impact the final part is the die temperature. Moradi et al., 2009 characterized the microstructure of thixoformed specimens with low and high die temperatures. A low die temperature leads to porosity and microscopic cracks due to a high thermal gradient between the billet and the die (see Figure 2.9). Nevertheless, in contrast to the low die temperature, by using a high die temperature the slurry moves more easily but porosity still exists in all the parts (see Figure 2.10).

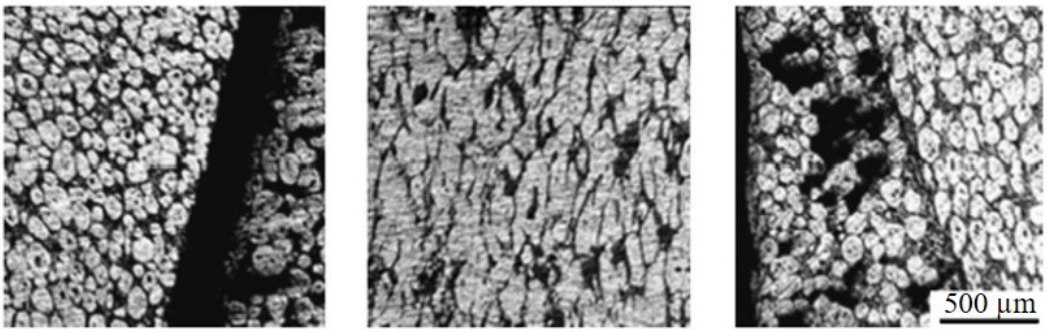

Figure 2.9: Microstructures at low die temperature (Adapted from Moradi et al., 2009)

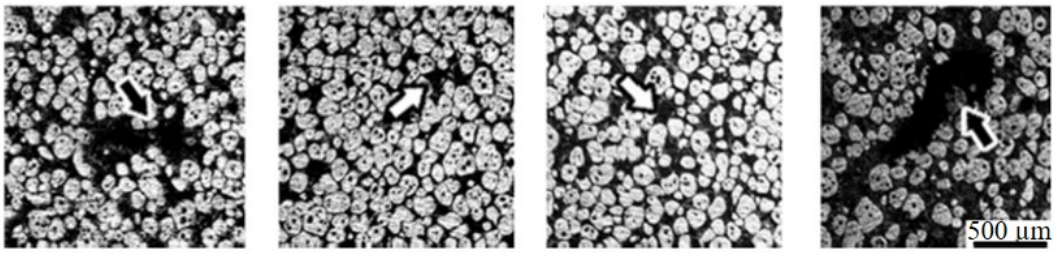

Figure 2.10: Microstructures at high die temperature (Adapted from Moradi et al., 2009)

Moreover, Li et al., 2017 also analysed the influence of die temperature. Cold shut is another defect related to metal flow problems. This defect is located on the surface in casting when the die temperature is low, so the material solidification is not completed (see Figure 2.11). Curle, Wilkins, and Govender, 2011 studied cold shuts in rheocasted callipers, determining that by adjusting the injection piston speed at the start, cold shuts could be eliminated.

Figure 2.11: Cold shuts (Adapted from Janudom et al., 2010)

Furthermore, Chen, Du, and Cheng, 2012 studied the presence of segregation and porosities in thixoformed samples. Solidification shrinkage and tensile deformation may cause different microporosities and microcracks in regions 2 and 4 (see Figure 2.12-b and d). However, microcracks may be filled using liquid metal (Chen, Du, and Cheng, 2012).

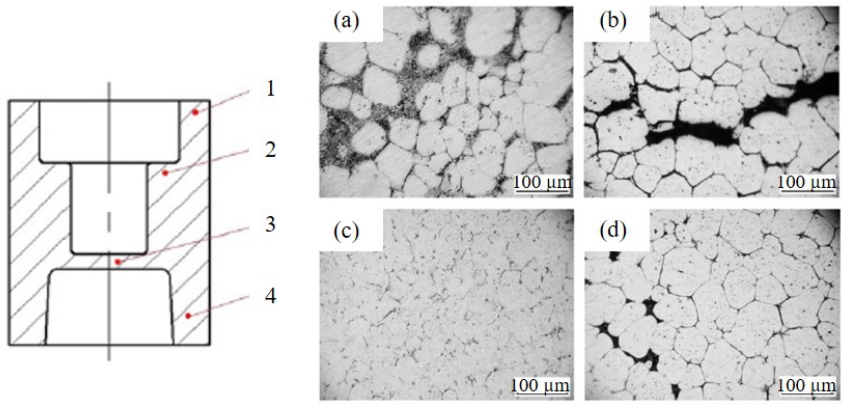

Figure 2.12: Microstructure of: (a) Region 1 (b) Region 2 (c) Region 3 (d) Region 4 (Adapted from Chen, Du, and Cheng, 2012)

On the other hand, for high solid fractions, process which may be closer to the NSF process as stated by Plata, 2018, cracking was observed (Kareh et al., 2017). For example, according to Nagira et al., 2014, when the solid fraction increases a decrease in the liquid

pressure occurs as it seems to be difficult for liquid to flow, explaining the cracking. In the particular case of high solid fractions during shear deformation, the grain boundaries are not coalesced and the absence of grain-grain cohesion causes the presence of liquid films as Figure 2.13 shows.

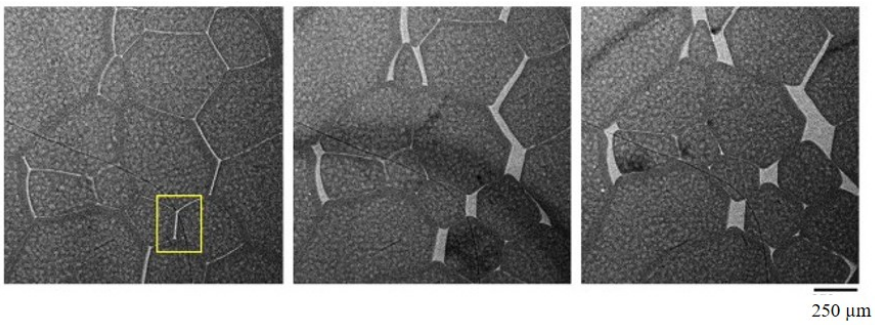

Figure 2.13: Radiographs of the shear-induced dilatation (Adapted from Kareh et al., 2017)

Thus, although more similarities could be expected between semisolid processes and the novel NSF process, it was demonstrated by Plata, 2018 that, because of the absence of liquid under these conditions, the material behaviour could not be approximated to a semisolid one. That is why, more similarities were found with hot die forging as stated in previous section.

2.3 HOT FORGING

Among all the forming processes, the main similarities of NSF were found with closed die hot forging, although this is carried out at temperatures up to $0.75T_m$. According to Biswal and Tripathy, 2021, even under these conditions it is difficult to quantitatively explain the phenomena behind this process. With closed die hot forging, it is possible to manufacture complex parts with good dimensional accuracy, reducing material waste and the force needed. These advantages are also taken by the NSF process (Lozares et al., 2020; Slater et al., 2020), reducing the steps needed to manufacture the part and obtaining good mechanical properties.

2.3.1 *Material characterization: flow behaviour*

As mentioned above, the viability of the NSF process has been demonstrated in manufacturing steel components (Lozares et al., 2020). However, a more in depth study into the material behaviour is necessary to understand it.

During the NSF process, the material is subjected to high temperature, strain and strain rate. Hardening and softening during deformation due to temperature, strain or strain rate are the mechanisms which determine the quality of the forged product

(Chadha, Shahriari, and Jahazi, 2018). Flow stresses at room temperature are highly dependent on temperature and strain rate whereas at high temperatures the behaviour becomes more complex and possible couplings between temperature, strain and strain rate effects may appear. In hot compression, materials which has strain hardening at low values become softer at strains higher than the peak value (Razali, Irani, and Joun, 2019).

The typical flow stress curve for steel at high temperature is shown in Figure 2.14. Three distinct stages consisting of strain hardening until the peak value, followed by a softening and, finally, a steady-state is observed. This peak is usually observable at low strain rates whereas at high strain rates it could not appear.

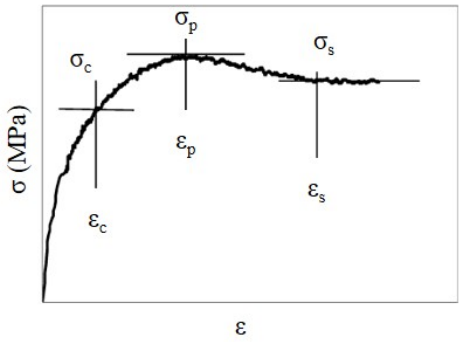

Figure 2.14: Typical flow behaviour of steel at high temperatures: σ_c (critical stress), σ_p (peak stress), σ_s (steady-state), ε_c (critical strain), ε_p (peak strain), ε_s (steady-state strain) (Adapted from Poliak and Jonas, 2003a)

For instance, Sun, Zhao, and Wu, 2017 investigated the effect of strain rate on the work-hardening rate using a high-Mn steel. Figure 2.15 shows how strain rate plays an important role in the work-hardening rate. In addition, Gronostajski et al., 2017 analysed the effect of strain rate on the strength and plasticity of different steels. The strength increases with the strain rate.

Another example is the research developed by Bayramin, Şimşir, and Efe, 2017. These authors studied the flow behaviour of a dual-phase steel under different conditions with strain rates between 0.0001 and 1 s^{-1} and temperatures from 100 to 400°C. Pandre et al., 2019 investigated this steel under the same conditions, and they showed how the flow stress decreases when the temperature increases. Under the conditions analysed, the strain hardening effect is seen, which is followed by necking and failure at low temperatures.

Based on the analysis carried out at high temperatures, steels show a typical behaviour composed by an initial zone of hardening (strain hardening) until the peak strain value, especially at low strain rates. After this zone, a slight softening was observed maybe due to dynamic recrystallization process. In addition, a notable thermal softening was observed at temperatures higher than 400°C (see Figure 2.16).

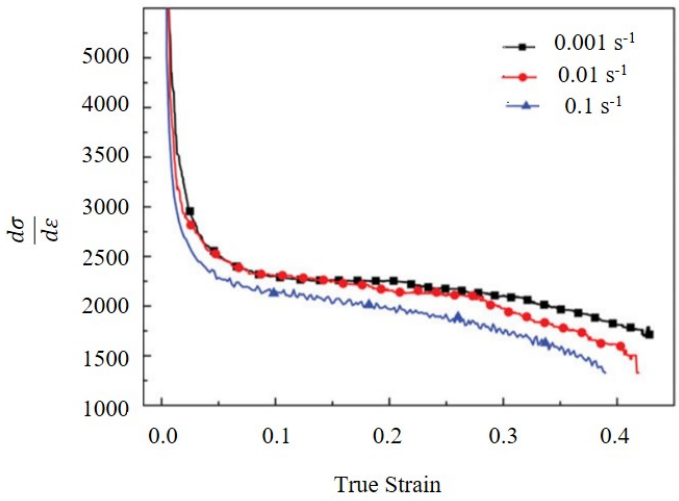

Figure 2.15: Work hardening rate-true strain curves at different strain rates (Adapted from Sun, Zhao, and Wu, 2017)

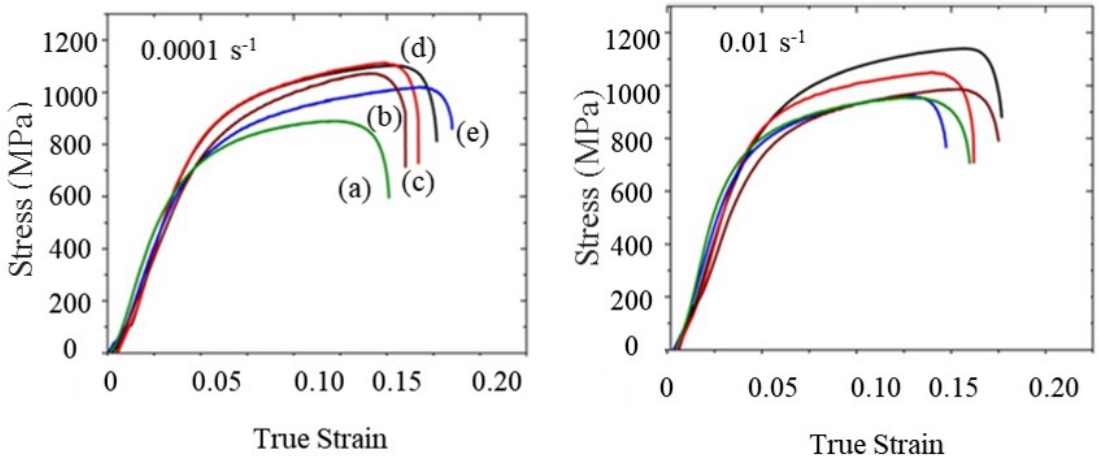

Figure 2.16: True stress-strain curves. Upper image: strain rate of 0.0001 s^{-1} Lower image: strain rate of 0.01 s^{-1}. (a) 400°C (b) 300°C (c) 100°C (d) Room temperature (e) 200°C (Adapted from Pandre et al., 2019)

However, a clear lack of knowledge was found as the conditions tested in literature are usually far from those reached in the NSF process, in general, the materials being characterized up to 1200°C. That is why, it is necessary to understand the material behaviour under more extreme conditions in order to test the possibility of extrapolating the information available.

2.3.2 *Material characterization configurations*

To characterize the material behaviour under close to forging process conditions, thermomechanical tests can be carried out. There are dissimilar ways to characterize the material behaviour, from uniaxial and biaxial tensile tests to compression tests (including plane strain). Firstly, due to the simplicity, the uniaxial tensile test is commonly used at low strain and strain rates. However, as the aim is to be as close as possible to NSF conditions, uniaxial tensile tests are not considered to be a possible option as the strains reached are notably lower than those observed in the NSF process as has been observed in the numerical simulations (Plata et al., 2020). Therefore, hot compression tests are preferred instead of high temperature tension tests (Anoop et al., 2020).

In terms of compression tests, the plane strain compression test (PSCT) is usually used to study flat rolling due to the stress-strain mode. In addition, PSCT is also used to determine mechanical properties and analyse the microstructure (Slater, Tamanna, and Davis, 2021). Plane strain compression tests have several advantages in comparison with other types of deformation modes. For instance, the material could be deformed to higher strains at high strain rates, facilitating the study of microstructural evolution. They usually involve plastic strain between 1 and 3 and strain rates from 10^{-2} to 100 s^{-1} (Drozd et al., 2011). One of the main problems of PSCT is the lack of uniformity in the flow material due to rigid specimen ends, that is why the curves could be influenced by the sample and the punch geometry (Aksenov, 2009). Based on this brief analysis, PCST appears as a promising approach to characterize material behaviour under close to NSF conditions. However, traditional plane strain compression tests tend to have non uniformity in the strain distribution, as stated by Tamanna, Slater, and Davis, 2022. An example of this mode of deformation can be seen in Figure 2.17. To overcome these limitations, a modified PSCT with 20 mm-wide anvils has been proposed to provide much greater strain uniformity and a large area suitable for microstructural analysis (Tamanna, Slater, and Davis, 2022).

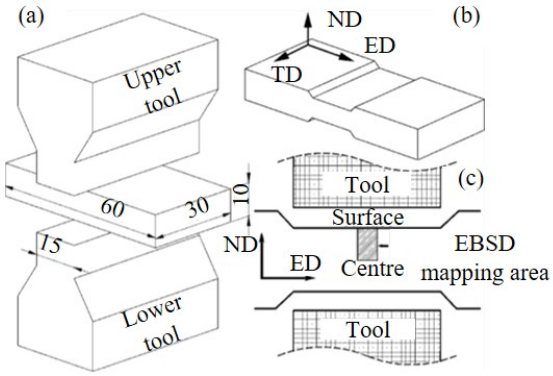

Figure 2.17: (a) Plane strain sample (b) Deformed plane strain sample (c) Location of EBSD maps (Adapted from Sun et al., 2010)

Similarly, uniaxial compression tests are widely used to characterize material behaviour at high temperatures. In this kind of test, cylindrical samples are used and they allow to cover a wide range of temperatures, strain and strain rates, similar to those reached with PSCT. Nevertheless, barrelling effect is one of the main issues, causing the sample to expand in the out of plane direction. Therefore, these tests, after applying the proper correction of the stress-strain curve, can be used to analyse material behaviour but they may not be the best option to analyse microstructural issues due to these inhomogeneities in the strain field (Slater, Tamanna, and Davis, 2021; Tamanna, Slater, and Davis, 2022), as can be seen in Figure 2.18.

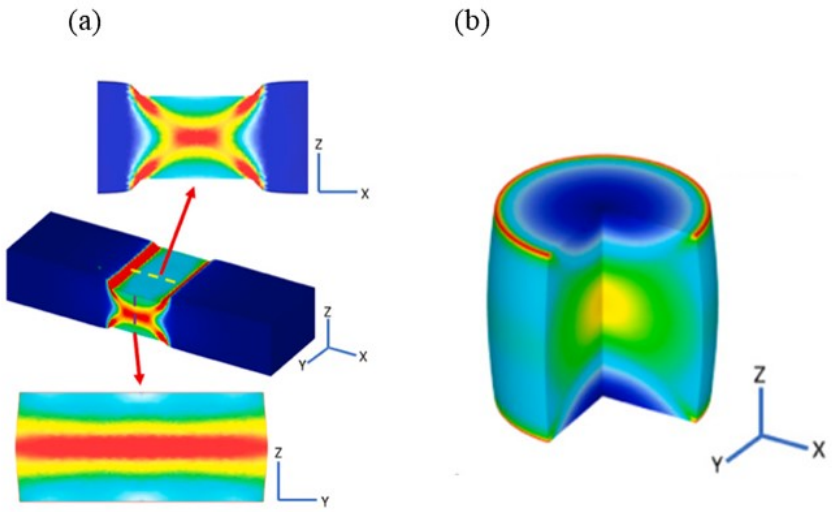

Figure 2.18: Strain fields: (a) Plane strain (b) Uniaxial compression tests (Adapted from Slater, Tamanna, and Davis, 2021)

To determine true stress-strain data from hot compression it is necessary to do some corrections as zero offset, machine compliance, increase in testpiece breadth and friction (which can be reduced using graphite, glass or Teflon) (Loveday et al., 2002).

To sum up, it is worth mentioning that the aim of the section was to briefly summarize the principal configurations commonly employed in material characterization. Based on the literature review it can be concluded that hot uniaxial compression is useful to study material behaviour from a macroscopic point of view based on flow stress-strain data, whereas for microstructural characterization the modified PSCT appears as a potential solution.

2.3.3 *Material behaviour modelling*

The flow behaviour of metals could be modelled by using different equations (Lin, Chen, and Zhong, 2008; Mandal et al., 2009; Lei et al., 2019). For instance, Hansel-Spittel law is typically used to simulate forging processes (see Equation (1)).

$$\sigma = A_0 e^{m_1 T} \varepsilon^{m_2} \dot{\varepsilon}^{m_3} e^{\frac{m_4}{\varepsilon}} (1+\varepsilon)^{m_5 T} e^{m_7 \varepsilon} \dot{\varepsilon}^{T m_8} T^{m_9} \tag{1}$$

where A_0 is a material constant, σ is stress, ε is strain, $\dot{\varepsilon}$ is strain rate and T is deformation temperature. The variables m_1 and m_9 describe the material sensitivity to temperature, m_5 defines the coupling between temperature and strain, m_8 represents the coupling between temperature and strain rate, m_2,m_4 and m_7 define the material sensitivity to strain and m_3 is the material sensitivity to strain rate. Constants m_8 and m_9 are usually taken as zero.

Figure 2.19 shows an example of the comparison between experimental (red curve) and the numerical one predicted using the Hansel-Spittel law (blue one).

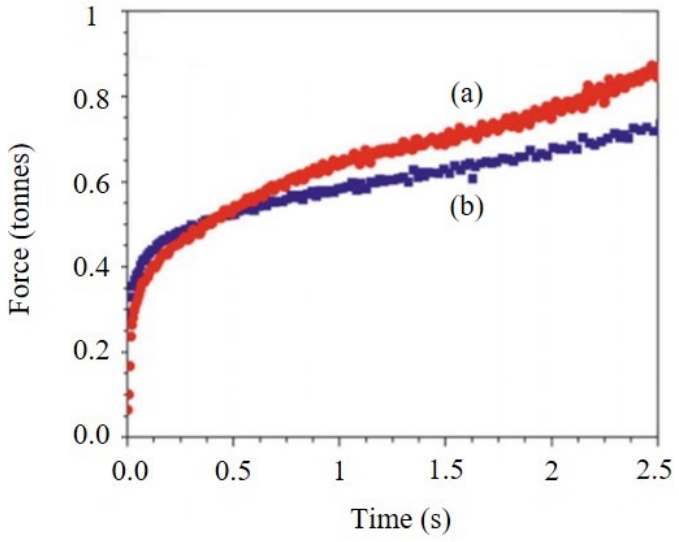

Figure 2.19: Force (tonnes) vs time at 0.25 s^{-1}: (a) Gleeble test (b) Simulation with Hansel Spittel Constitutive Model (Adapted from Chadha, Shahriari, and Jahazi, 2018)

Also, flow stress could be approximated through the hyperbolic law according to Arrhenius equation (see Equation (2)) using the Zener Hollomon parameter (see Equation (3)). This parameter shows the effect of temperature and strain rate on deformation.

$$\dot{\varepsilon} = A_i F(\sigma) \exp\left(-\frac{Q}{RT}\right) \tag{2}$$

$$Z = \dot{\varepsilon} \exp\left(\frac{Q}{RT}\right) \tag{3}$$

where Q is the activation energy $(\mathrm{J/mol})$, R is gas constant $(\mathrm{J/(mol \cdot K)})$, T is the absolute temperature (K) and $\dot{\varepsilon}$ is strain rate. α, β, b, n, A_i are material constants where $\alpha = \beta \ / \ b$.

The Arrehnius equation (see Equation (2)) can be written as Equation (4), (5) and (6). The parameter $F(\sigma)$ depends on the stress regime Equation (4) being valid for all σ, Equation (5) for $\alpha\sigma < 0.8$ (low stress) and Equation (6) for $\alpha\sigma > 1.2$ (high stress).

$$\dot{\varepsilon} = A_3[\sinh(\alpha\sigma)]^{\mathrm{n}} \exp\left(-\frac{Q}{RT}\right) \tag{4}$$

$$\dot{\varepsilon} = A_1 \sigma^b \exp\left(-\frac{Q}{RT}\right) \tag{5}$$

$$\dot{\varepsilon} = A_2 \exp(\beta\sigma) \exp\left(-\frac{Q}{RT}\right) \tag{6}$$

To determine all the material parameters the following procedure can be used. Firstly, taking the logarithm of both sides of Equation (4), (5) and (6), the following Equations can be obtained (7), (8) and (9). Secondly, α, β and b can be determined using Equation (8) and (9). Then, n can be calculated at a specific temperature taking into account Equation (7).

$$\ln \dot{\varepsilon} = \ln A_3 - Q/RT + n \ln[\sinh(\alpha\sigma_p)] \tag{7}$$

$$\ln \dot{\varepsilon} = \ln A_1 + b \ln \sigma_p - Q/RT \tag{8}$$

$$\ln \dot{\varepsilon} = \ln A_2 + \beta\sigma_p - Q/RT \tag{9}$$

Finally, the activation energy can be determined for a particular strain rate plotting $\ln[\sinh(\alpha\sigma)]$ versus $1/T$ using Equation (7). Thus, Q is calculated as the average value at different strain rates. For a more in depth explanation, see Wang et al., 2016a.

Other laws could be mentioned, one of the most commonly used laws is the one proposed by Johnson-Cook (Johnson and Cook, 1983). The law takes into account strain and strain rate hardening and thermal softening. However, Johnson-Cook does not consider the coupling between strain, strain rate and temperature, couplings which are taken into account in Hansel-Spittel equation. That is why, Calamaz, Coupard, and Girot, 2008 proposed a correction to Johnson-Cook model adding a new term with the coupling between temperature and strain effect.

The laws previously presented are usually based on empirical data. In order to improve the accuracy of the predictions, Zerilli and Armstrong, 1987 developed a dislocation based constitutive law. The model considers strain hardening, temperature softening, strain rate hardening and coupling effects.

It is worth highlighting that Hansel-Spittel equation is widely used as it includes not only the effect of temperature, strain and strain-rate, but also different possible couplings and it is of great interest to be studied as it is used in numerical software such as Forge NXT®.

2.4 RECRYSTALLIZATION AND RECOVERY

Manufacturing of steel requires having good mechanical properties. To attain that objective, hot-deformation processes are a relevant tool to improve the microstructure thus enhancing these mechanical properties. Therefore, recrystallization is a relevant way to refine the microstructure resulting in good mechanical properties during industrial processes (Shaban and Eghbali, 2010).

Hardening (dislocation storage) and softening (dislocation elimination) mechanisms could operate together in hot forming processes (López and Rodriguez-Ibabe, 2012). Recrystallization, recovery and grain growth take place due to temperature, strain rate and strain produced during deformation. It is widely known that at temperatures higher than 0.5 times melting temperature (in Kelvin), dissimilar processes due to plastic deformation occur such as dynamic recovery and recrystallization.

As López and Rodriguez-Ibabe, 2012 stated, recrystallization is a process in which the formation and migration of high-angle grain boundaries, driven by the stored deformation energy, occurs. Recrystallization can be classified in three major groups: static (SRX), dynamic (DRX) and metadynamic (MDRX) depending on the conditions under which the process occurs.

It is worth mentioning that there are two types of DRX, discontinuous (dDRX) and continuous DRX (cDRX) (see Table 2.3, being SFE stacking fault energy). The main difference between those processes is the conditions under which they occur (Babu et al., 2021). At the beginning, the grains formed by dDRX present curved boundaries and dislocation substructures. Moreover, the new grains appear along the boundaries as Figure 2.20 shows, whereas cDRX grains are developed due to the increase in sub-boundary misorientation as a result of continuous accumulation of the dislocations introduced by the deformation (see Figure 2.21) (Sakai et al., 2014). Another typical characteristic of cDRX is the large strains at which is developed. dDRX causes new grains during deformation which results in softening and a reduction in the hardening rate.

Table 2.3: Characteristics of discontinuous and continuous dynamic recrystallization (Adapted from Sakai et al., 2014)

Types of DRX	dDRX	cDRX
Strain	Strain lower than 1	Strain higher than 3
T/T_m	Above 0.5	0-1
SFE	Low and medium	Low to high
Critical strain	Depending on temperature and strain rate	Not dependent on temperature or strain rate

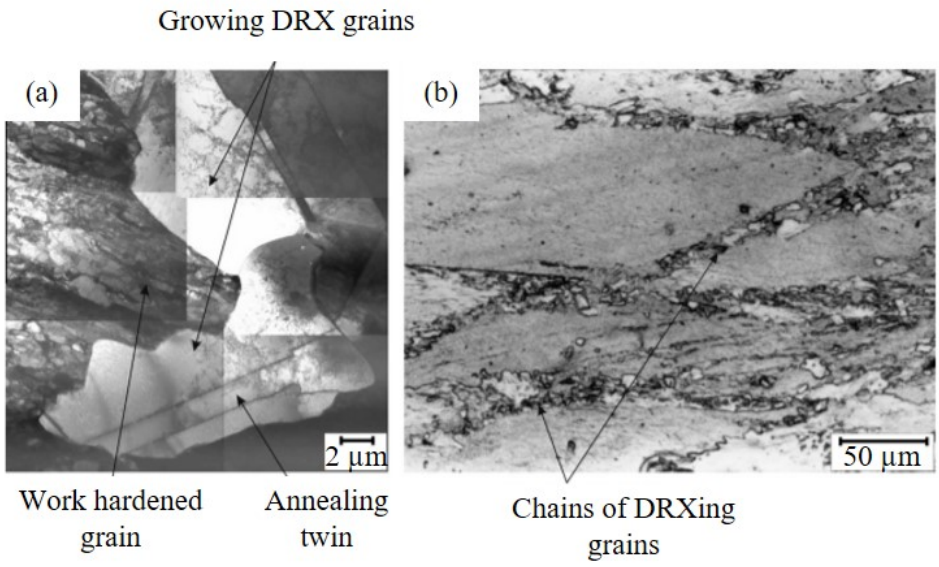

Figure 2.20: An example of dDRX using pure Cu (a) growing grains at 623 K under deformation conditions (b) the typical necklace microstructure during compression at 573 K (Adapted from Sakai et al., 2014)

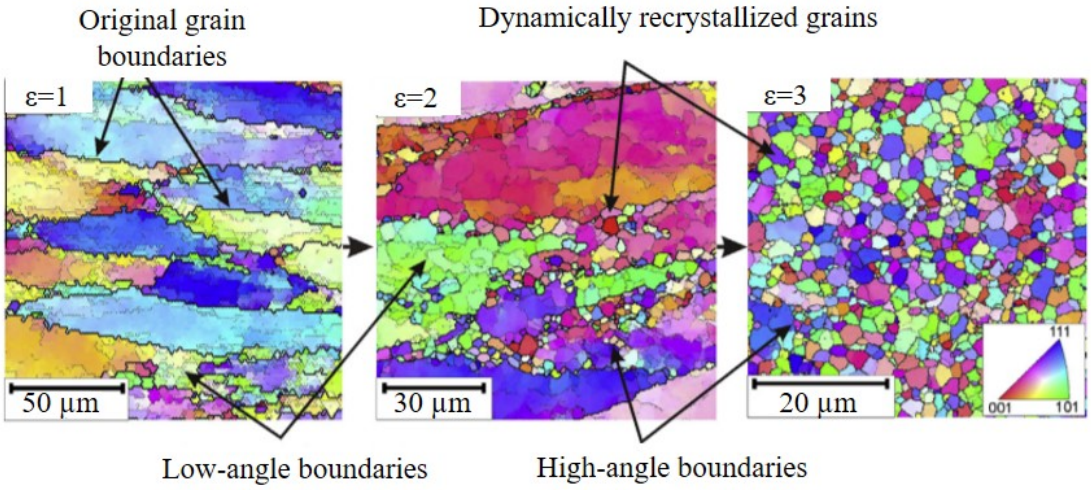

Figure 2.21: An example of cDRX using aluminium alloy deformed continually by ECAP under (a) 1 (b) 2 (c) 3 of strain (Adapted from Sakai et al., 2014)

Then, another deformation behaviour under high temperature conditions is DRV, which is defined by a continuous increase in flow stresses during plastic working. Then, the rate of strain hardening decreases with deformation and approaches zero, leading to a steady state (Sakai et al., 2014). Materials can be classified under DRV or dDRX mechanisms according to their stacking fault energy. For example, austenitic Fe and their alloys are low to medium SFE whereas aluminium or ferritic iron are high SFE. There are some materials such as aluminium alloys in which work hardening and dynamic recovery (DRV) can stabilize the flow curve generating a plateau. Nevertheless, in other materials, for example, the austenite phase of steels, the low kinetics of DRV make it impossible to stabilize the curve just taking into account DRV (Mirzadeh et al., 2011). As a result, the existence of such plateau could be an indicator of recrystallization (mainly DRX). It has been recognized that DRX is one of the most important softening mechanisms in hot deformation, having effects on the microstructure, grain size and flow stress (Mirzadeh, Najafizadeh, and Moazeny, 2009).

According to different researchers (Sellars and McTegart, 1966; McQueen, Wong, and Jonas, 1967) hot working can be considered as a thermally activated process which can be modelled based on strain rate equations. True stress-true strain data are obtained through hot compression tests using a thermo-mechanical simulator. From this data, DRX behaviour could be observed as a peak value and a posteriori steady state stress (see Figure 2.14). When the strain rate is fixed, the peak stresses decrease when temperature increases (see Figure 2.22). In addition, maintaining a constant temperature, flow stresses increase as the strain rate increases.

As shown in Figure 2.14, DRX starts when strain is higher than critical strain ε_c. It is worth highlighting that the critical strain in dDRX is dependent on temperature,

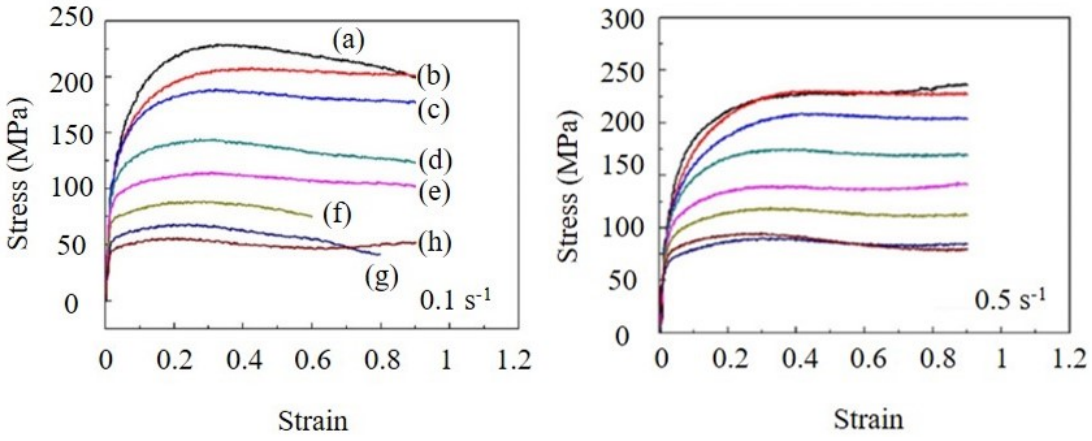

Figure 2.22: Stress-Strain curves at: (a) 0.1 s^{-1} (b) 0.5 s^{-1}. (a) 900°C (b) 950°C (c) 1000°C (d) 1050°C (e) 1100°C (f) 1150°C (g) 1200°C (h) 1250°C (Adapted from Wang et al., 2016a)

strain rate and the initial grain size (see Figure 2.23). Furthermore, the critical strain in the case of dDRX decreases with the increment of temperature and the decreasing of the strain rate. Grains could nucleate in triple points and grain boundaries (Kim and Yoo, 2001).

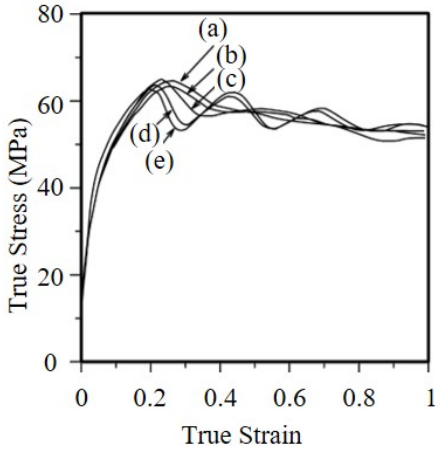

Figure 2.23: Stress-Strain curves at 1173 K and 1.4e-3 using 0.06C-1.43Mn steel (a) 375 (b) 270 (c) 150 (d) 90 (e) 60 µm (Adapted from Sakai et al., 2014)

2.4.1 *Effect of different parameters on recrystallization*

El Wahabi et al., 2005 analysed the influence of initial grain size on dynamic recrystallization using two different AISI 304. The main difference between them was the carbon content. To attain this aim, these researchers carried out tests using different initial grain sizes at dissimilar temperatures between 850 and 1100°C under low strain rate conditions (0.001 s^{-1}) as Figure 2.24 shows.

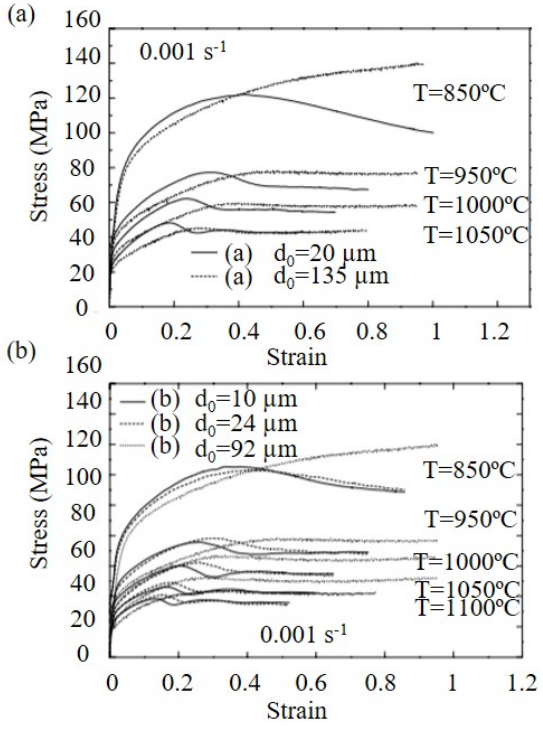

Figure 2.24: Stress-Strain curves at (a) material with ultra-high purity (b) material with high purity (Adapted from El Wahabi et al., 2005)

The flow curve (Figure 2.24a) exhibits at 1000 and 1050°C the same steady state whereas the dDRX initiation of both materials started later in the case of large initial grain size. It is worth mentioning that this behaviour gives more time for recovery processes to take place. Thus, when dDRX occurs, dynamic recovery could achieve an advanced stage. Consequently, this effect is observed in both materials with large initial grain sizes due to the low fraction of grain boundaries. In Figure 2.25 the initial grain size for both materials depending on temperature is shown. One of the alloys exhibits no differences between two initial grain sizes whereas the other one shows a variation in the case of the larger initial grain size.

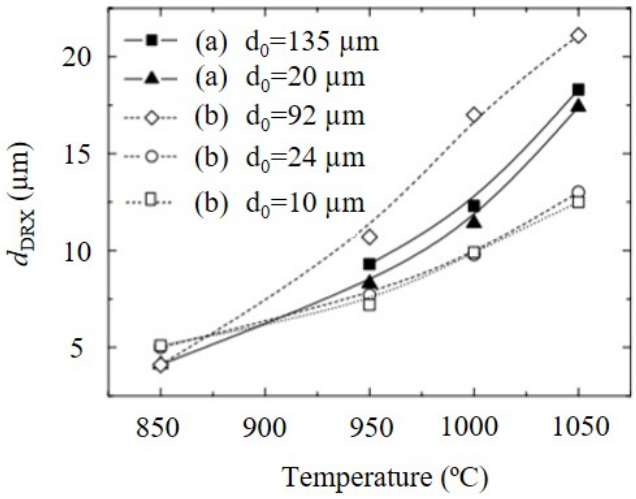

Figure 2.25: Recrystallized grain sizes versus temperature (Adapted from El Wahabi et al., 2005)

Another parameter which could have an effect on dynamic recrystallization is the strain rate. It is widely reported that high strain rate could improve DRX kinetics (Wang et al., 2021). Babu et al., 2018 studied dDRX using super-304H austenitic stainless steel under dissimilar conditions of temperature and strain rate. They observed that the microstructure at high temperature and strain rate (1373 K and 10 s^{-1}) was different in comparison with those obtained at the same temperature and different strain rate (0.1 s^{-1}) (see Figure 2.26). On this basis, high strain rates are assumed to be related with higher DRX kinetics at high temperature which result in an easy formation of more number of nuclei.

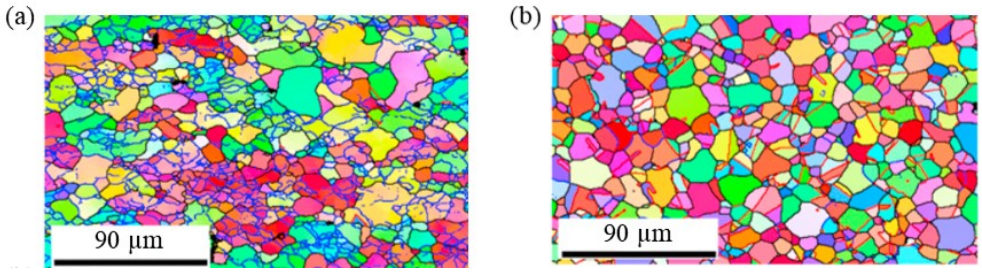

Figure 2.26: Microstructures of super-304H austenitic stainless steel (a) 1373 K and 0.1 s^{-1} (b) 1373 K and 10 s^{-1} (Adapted from Babu et al., 2018)

Finally, it is widely reported that temperature has an important influence on DRX mechanism. Hu et al., 2021 carried out compression tests under dissimilar conditions of temperature and strain rate (900-1200°C and 0.01-10 s^{-1}) using super-austenitic stainless steel. They observed a decrease in the peak stress with the increase of temperature and

the decrease of strain rate (see Figure 2.27). High thermal energy associated with high temperature facilitates dislocations and grain boundaries movement. On this basis, at high temperatures, DRX is enhanced thanks to this higher thermal energy.

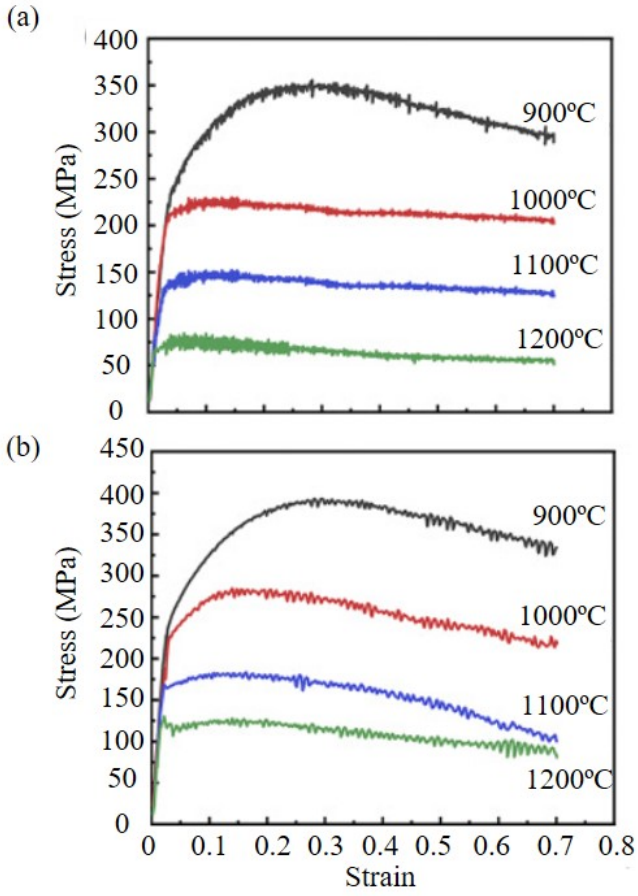

Figure 2.27: Flow stress curves of superaustenitic stainless steel (a) 0.01 s^{-1} (b) 0.1 s^{-1} (Adapted from Hu et al., 2021)

Among all the restoration processes analysed, recrystallization could play a relevant role in the NSF process as it occurs at high temperatures and strain rates, conditions which are representative of the NSF process. Despite this process is widely studied in the literature, no research work was found covering these extreme conditions.

2.4.2 *Recrystallization kinetics*

As DRX could have a considerable influence on flow stress under hot working conditions, the prediction of its kinetics is of great interest, not only for modelling purposes but also for industrial hot working processes.

One of the main characteristics of the flow stress curves is the peak strain. That is, the strain at which the flow stress curve reaches the maximum stress. Here, it is worth mentioning that the presence of a peak could be a sign of recrystallization but it could also occur for conditions under which this peak is not observable.

When the peak can be easily measured, it is usually modelled according to Equation (10). Peak strain is easier to be experimentally measured than the critical one, that is why these two parameters are commonly related according to Equation (11). It is worth noting that k_1 is generally between 0.5-0.6 for microalloyed and stainless steels (Marchattiwar et al., 2013; Nkhoma, Siyasiya, and Stumpf, 2014; Wang et al., 2016a).

$$\varepsilon_{\mathrm{p}} = A_p \cdot D_0^m \cdot Z^p \tag{10}$$

$$\varepsilon_{\mathrm{c}} = k_1 \varepsilon_{\mathrm{p}} \tag{11}$$

where m,p and A_p are material parameters and D_0 is the initial grain size (López and Rodriguez-Ibabe, 2012).

The kinetics of dynamic recrystallization can be represented by the Avrami equation (see Equation (12)).

$$X = 1 - \exp\left(-k\left(\varepsilon - \varepsilon_c\right)^{n'}\right) \tag{12}$$

where k is the Avrami material constant, and n' is the Avrami exponent, being 2 for dissimilar steels according to different authors (Marchattiwar et al., 2013; Dupin, Yana, and Yanag., 2014).

There are two ways to define the critical strain at which DRX starts, by microstructural observations (metallography) and by the analysis of the flow stress curves. However, the first analysis is very time-consuming because of the high amount of samples needed to analyse and the difficulty in the preparation. Also, some materials have phase changes that could increase this difficulty.

To overcome these limitations, several researchers defined mathematical relations to predict the initiation of DRX (Shaban and Eghbali, 2010). For instance, McQueen, Wong, and Jonas, 1967 proposed the initiation of DRX using the changing in the slope of the strain hardening rate versus flow stress curves (Ryan and McQueen, 1990a) whereas Poliak and Jonas, 2003a suggested the critical stress at which DRX starts as the inflection point in the strain hardening versus stress curve (Jonas and Poliak, 2003). This second method, according to Jafari and Najafizadeh, 2008, to avoid (or at least, reduce) the error in the differentiation, would require modelling as a 9th order polynomial the region of plastic deformation including the peak stress. Also, Najafizadeh and Jonas, 2006

developed a method based on the previous one (Poliak and Jonas method). To develop this approach, a third−order equation is needed to fit the strain hardening rate versus flow stress curves in which the critical stress is the relation between $b_1/3a$ where a and b_1 are two of the four coefficients in the fitting equation (see Equation (13)).

$$\theta = a\sigma^3 + b_1\sigma^2 + c\sigma + d \tag{13}$$

As was mentioned above, the presence of a peak in the flow stress curves is supposed to be a sign of dynamic recrystallization. However, it could be possible to have DRX without the presence of this peak. Different authors such as Lan, Zhou, and Misra, 2019 classified the flow stress-strain curves in two main groups: with and without the peak.

For example, in the first case, the peaks occurred under high temperature, low strain rate combinations whereas this flat top behaviour without a peak is related to low temperatures or high strain rates, leading to the assumption that this behaviour could be considered as dynamic recovery (Taylor and Hodgson, 2011). Nevertheless, metallurgical observations have shown the evidence of recrystallization (Taylor and Hodgson, 2011).

Ryan and McQueen, 1990b determined the critical strain using work hardening rate $\left(\theta = \frac{\delta\sigma}{\delta\varepsilon}\right)$ versus stress as it is shown in Figure 2.28. The reason for using this method lies in the fact that DRX has an observable effect on the shape of the flow curve and, thus, on the associated hardening rates. Moreover, DRX generates new unstrained grains and this can be determined by considering possible changes in the shape of the flow curves (see Figure 2.28).

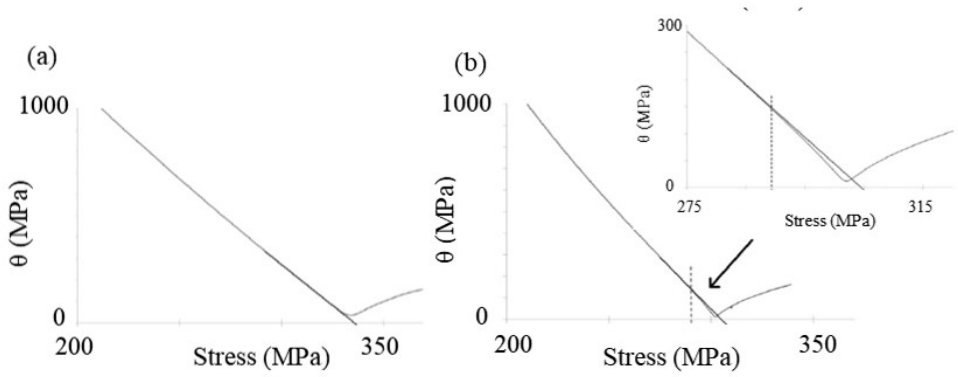

Figure 2.28: Work-hardening versus Stress: (a) No DRX (b) Critical Stress (Adapted from Taylor and Hodgson, 2011)

Several researchers studied this phenomenon through thermomechanical tests. Shaban and Eghbali, 2010 investigated the initiation of DRX under dissimilar compression conditions in a microalloyed steel. To attain this aim, each sample was heated up to

1200°C and then, the material was cooled to 900°C, 1000°C and 1100°C. At each temperature, the material was deformed at 0.01, 0.1 and 1 s^{-1} as Figure 2.29 shows.

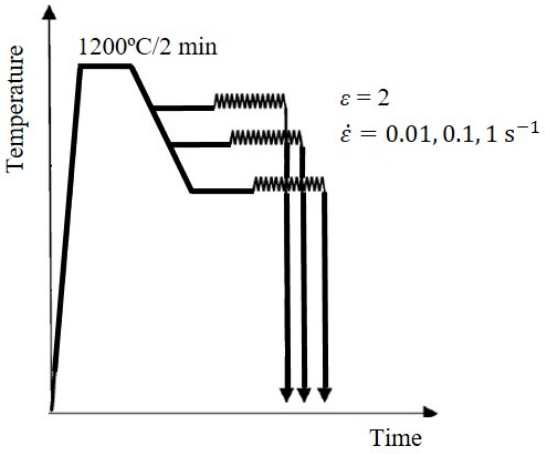

Figure 2.29: Thermomechanical processes using a microalloyed steel (Adapted from Shaban and Eghbali, 2010)

The strain-stress curves showed an increase in the working hardening rate due to the increase of strain rate as Figure 2.30 shows. Moreover, it can be seen that the peak stress and peak strain are dependent on strain rate. For example, at the lowest strain rate no peak was observed at 900°C whereas at the other two temperatures a clear peak appeared.

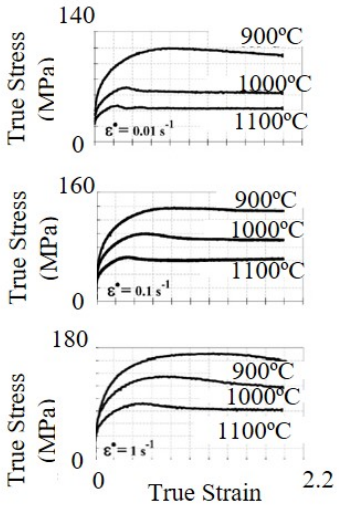

Figure 2.30: True stress-true strain curves under dissimilar conditions (Adapted from Shaban and Eghbali, 2010)

Therefore, dissimilar parameters could be obtained by using work-hardening curves even though a peak is not observed: critical stress and strain, peak stress and strain and steady-state stress and strain. Firstly, from the work hardening rate versus stress plot, the critical stress is defined as the point at which the curve has a deviation, in other words, is a reduction of the flow stress. Then, the peak stress is the value at which the work hardening rate is equal to zero. Finally, the steady-state stress could be determined by the extrapolation of the lower linear segment to θ=0 (Ryan and McQueen, 1990b). Each characteristic point could be seen in Figure 2.31.

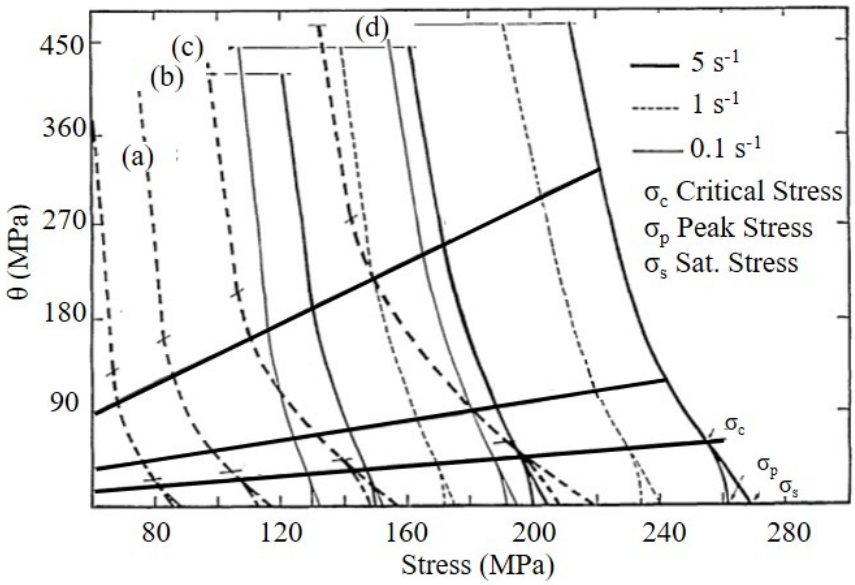

Figure 2.31: Critical, Peak and Saturation Stress. (a) 1200°C (b) 1100°C (c) 1000°C (d) 900°C (Adapted from Ryan and McQueen, 1990b)

Also, the method proposed by Jonas and Poliak, 2003 could be used (Poliak and Jonas, 2003a; Lan, Zhou, and Misra, 2019). This method is based on fitting a third-order polynomial up to the peak value as Equation (13) shows. That is why this method should be employed when the presence of a peak is clear and could lead to wrong values in the cases in which this peak is not appreciable.

The effect of temperature in critical and peak stress can be seen in Figure 2.32. Both curves are the result of testing the material at 0.1 s^{-1}. Concerning the temperature, the material was tested at 1000°C (see upper side) and at 1050°C (the other one). The main difference between them is the reduction observed in the peak and critical stress due to the thermal softening effect.

Nevertheless, these analyses are generally developed at temperatures between 900 and 1200°C, at strain up to 1 and strain rates from 0.001 to 10 s^{-1}. These conditions, although they make the analysis easier, are usually not able to reproduce industrial conditions as, for example, those reached in the NSF process (Lozares et al., 2020).

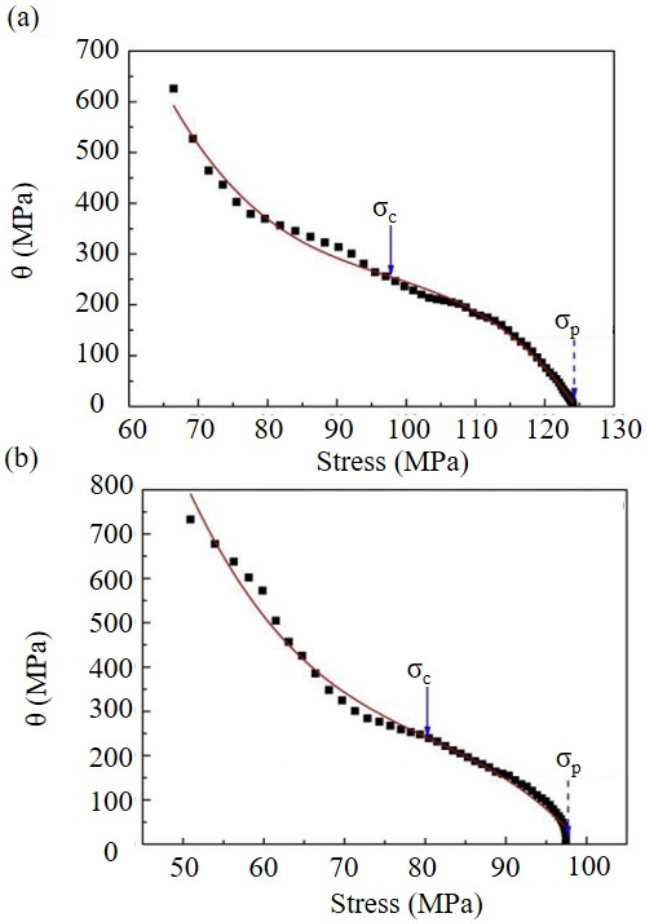

Figure 2.32: Work hardening rate versus Stress: (a) 1000°C 0.1 s^{-1} (b) 1050°C 0.1 s^{-1} (Adapted from Lan, Zhou, and Misra, 2019)

It is worth noting that under NSF conditions, under which strain and temperature are notably high, dynamic recrystallization would be expected. Therefore, among all the possible recrystallization processes, dynamic recrystallization is expected to be the main factor affecting NSF, although MDRX could occur if there is not enough time for recrystallization to occur following DRX mechanism.

2.5 CRITICAL ANALYSIS AND RESEARCH OPPORTUNITIES

Based on the analysis of the literature, the following research opportunities, addressed during this research work, can be summarized. It is worth highlighting that these research gaps cover all the information with regard to the literature review included not only in

this chapter but also in the rest of the document but they have been included here to give a clear overview about the topics addressed during this work:

- NSF has emerged as a promising hot working process to manufacture complex steel parts, reducing the steps needed by manufacturing the part at temperatures close to the solidus. However, although the process showed remarkable results, there is a clear lack of knowledge aiming to explain the reasons which lie this process to work. In principle, at these high temperatures, the final microstructure would be expected to have high grain sizes with poor mechanical properties but this assumption was proven to be not valid in previous works.

- To understand material behaviour, thermomechanical tests are the most widely used tool in order to understand how temperature, strain and strain rate may have an effect on the equivalent stress. Among all the possibilities, material behaviour is usually characterized through uniaxial compression tests. Nevertheless, this test configuration could lead to a non-uniform strain field. That is why, plane strain compression appears also as a possible and very useful tool to characterize the material, together with the fact that it generates more uniform strain, making it more accurate the microstructural analysis.

- According to the literature reviewed, regardless of the compression mode employed in the characterization, extreme conditions reached in the NSF process are usually not analysed in the literature. For instance, the highest temperature found in the literature was 1250°C, which is far from those reported for the NSF process. This issue influences also the accuracy of the predictions through numerical simulations, making extrapolation necessary. Therefore, this opens a clear gap to be filled as it is needed to understand material behaviour under these extreme conditions in order to know what is happening during the NSF process.

- During hot working conditions, different restoration processes, mainly recovery or recrystallization, may occur. As stated above, recrystallization tends to occur in steels when subjected to hot working conditions. Nevertheless, no research work was found analysing the recrystallization phenomenon under the extreme conditions reached during the NSF process. This restoration mechanism could explain the potential observed for the NSF process, as smaller grain sizes than the initial ones are obtained, which would result in better mechanical properties.

- In addition, prediction of final recrystallized grain sizes would also be of great relevance to understand the material behaviour of the final part. However, no agreement was found between researchers with regard to the laws to model recrystallized grain sizes, together with the fact that the majority of the trials were carried out under conditions far from those representative of the NSF process, makes it necessary to determine the grain size evolution subjected to these extreme conditions.

3

OBJECTIVES

The main objective of this research work was to characterize the material's behaviour under the conditions reached during the NSF process (temperature, strain and strain rate) using AISI 316 in order to understand why this process works and optimise it.

To attain this aim, the following research objectives were defined:

1. Characterize the flow behaviour under extreme hot working conditions representative of the NSF process, in order to understand the material behaviour and to optimize the flow stress law to increase the accuracy of the predictions through numerical simulations.

2. Determine analytically the onset for dynamic recrystallization (DRX) initiation under the mentioned extreme conditions representative of the NSF process, taking into account the influence of temperature, strain rate and heating profile.

3. Metallurgical validation through optical and EBSD measurements of the analytical calculus of the onset for DRX, proving that this restoration process could take place under NSF conditions. Also, the study of the possible presence of post-dynamic recrystallization (or metadynamic, MDRX) to be able to model the recrystallized grain size of the manufactured part.

4. Analyse grain growth kinetics of a sample subjected to the heating profile representative of the NSF process to understand the microstructural behaviour of the material before being deformed.

5. Proving the capacity for the NSF process of manufacturing austenitic stainless steel parts, analysing the material flow behaviour through numerical simulations and the final microstructure along the manufactured part.

4

METHODOLOGY

To attain the objectives mentioned in Chapter 3 different experimental devices were needed, first, to characterize the material behaviour under NSF conditions. That is why, the main aim of this chapter is to give an in-depth explanation of all of them used to develop this work.

In addition, an overview of the material to be used during these experimental tests is also given, together with the explanation of the NSF cell used in the industrial validation. This validation was accompanied with numerical simulations using Forge NXT® as it is a widely used software to simulate forming processes.

4.1 EXPERIMENTAL DEVICES FOR THERMOMECHANICAL CHARACTERIZATION

4.1.1 *Differential Scanning Calorimetry*

This section covers the DSC analysis to determine the temperature working window at which the NSF process works. DSC is a method of thermal analysis in which the sample and the reference sample are heating up to a controlled temperature (Höhne, Hemminger, and Flammersheim, 2013). Also, it has the capacity for measuring heat capacity and thermal conductivity. Moreover, DSC is a sensitive technique for determining the phase transition temperatures, solidification onset, activation energy for the grain growth or precipitation (Klančnik, Medved, and Mrvar, 2010).

The thermal characterization was carried out in DSC NIETZCH STA 449 F3 Jupiter® (see Figure 4.1). This equipment uses samples around 50 mg which are heated up at 10°C/min rate to achieve a temperature 30°C higher than the theoretical liquidus. As a result, the heat flux versus time or temperature is obtained. The main characteristics of this curve are:

- The changes of slope, jumps and peaks are the thermal events
- The peak area is the enthalpy variation of the transformation
- The specific heat is calculated from the baseline
- Solidus-liquidus interval could be determined

To obtain the values of interest, the method of partial areas was employed (see Figure 4.2). According to the equilibrium phase diagram, the differences on solid composition change to maintain the equilibrium as the temperature is increased. This makes it difficult

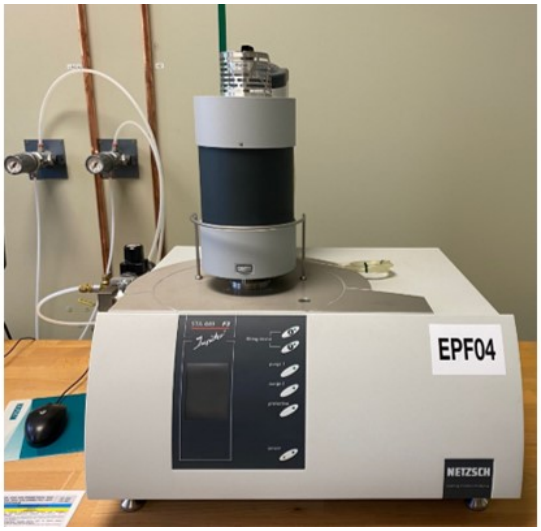

Figure 4.1: DSC equipment

to obtain exact values from the mentioned method. In addition, the melting heat, which means the energy needed to change from solid to liquid, is function of the composition as it depends on atoms distribution.

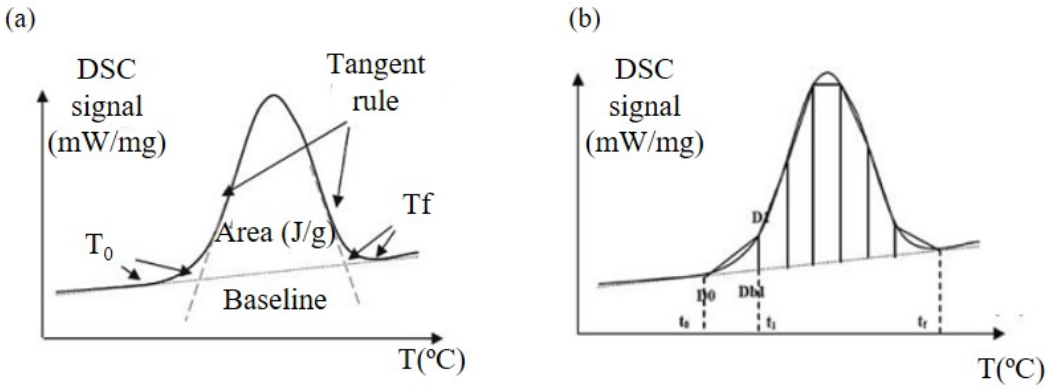

Figure 4.2: (a) Melting peak features (b) Determination of the liquid fraction (Adapted from Lecomte-Beckers et al., 2007)

On this basis, especially when the alloy to be characterized notably differs from the solvent metal, this method reports substantial error as the melting heat is much more different than the latent heat of this solvent metal. Therefore, the partial areas method considers the material as a unique system which is heated in an homogenous

way, not considering, for instance, segregation phenomena although this could lead to modifications in the melting behaviour.

In general, the first drop in the curve is assumed to be related to melting initiation. However, it is difficult to establish the equipment resolution as this drop may be related to the detection of a certain amount of liquid. In addition, it is difficult to ensure the accurate values of solidus and liquidus temperatures as they are widely dependent on the area calculation which could be influenced by the personal appreciation of the end user. Another relevant aspect to be taken into account lies in the fact that the technique is based on equilibrium conditions. Thus, it employs heating rates from 5 to 20°C/min, values notable lower in comparison to those used under real industry conditions.

Although this technique presents some drawbacks (partial areas method assumes the material as a unique system that melts homogeneously, it is hard to estimate the equipment resolution) it is still the best option to estimate the solidus and liquidus temperatures. It was established by Lozares et al., 2020 that the working temperature of the NSF process should be between 0.9 and 0.95 times the solidus. Therefore, it easily gives a great reference point to the NSF process. In addition, this technique allows the existence of phase changes during heating to be determined.

4.1.2 *Furnace trials*

Together with the determination of the solidus temperature it is also necessary to have an accurate control of the heating during the process. This heating determines not only the performance of the test, if the billet is not properly heated the process fails; but also the microstructure of the part which, in the end, defines the final properties of the part.

On this basis, the heating of a billet was characterized using a high temperature muffle furnace equal to the one employed to carry out the NSF parts. This furnace could reach 1600°C using direct resistance heating. To ensure that the sample was at the desired temperature, the heating was calibrated using a S-type thermocouple positioned in the middle of a billet. The sample for the calibration consisted of a cylindrical billet with 65 mm in diameter and 92 mm in height. These dimensions are representative of a typical sample used in the NSF process. The discrepancies between the set temperature and the thermocouple measurements were 50°C at low temperatures and 6°C at high ones. The calibration can be seen in Figure 4.3.

Then, after the calibration, the real heating profile (from now called commercial heating profile) followed by the sample prior to the NSF test was also determined. To define it, a S-type thermocouple was placed in the middle of the billet and the sample was heated up from room temperature to the NSF temperature which was defined using the DSC.

Also, to properly understand material behaviour and the NSF process, it is necessary to have a proper control of the grain sizes. For the analysis of the initial grain sizes under commercial heating conditions, different cylindrical shape samples were used with 10 mm

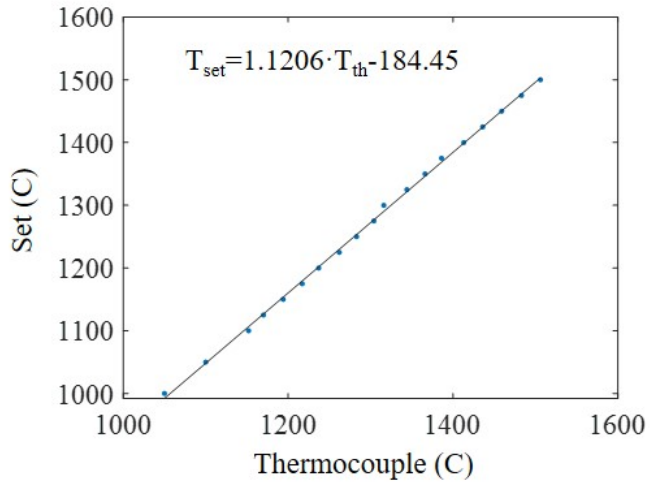

Figure 4.3: Calibration of high temperature muffle furnace

in diameter and in height. These dimensions were low enough to ensure the complete heating of the sample. The material used was the same as for the calibration.

In addition, two dissimilar holding times were selected, being 7 min and 17 min, to understand grain growth kinetics. This last value was based on the time needed to heat the billet in the NSF test. It is worth mentioning that the effect of opening the oven causes an increment of 40°C which delays 2 min to reach the set-temperature. To measure the grain sizes after heating, the samples were quenched using cold water.

Finally, the samples were mounted in a resin and polished up to mirror finishing. Then, they were electro-etched with Oxalic acid to reveal the microstructure. It is worth noting that other reagents as Kallings or Alcohol+HCl+Fe3Cl, among others, were also tested not achieving the desired results. The grain sizes were measured using the intercept method which consists of drawing a random straight line. Then, the number of intersections are counted. The average grain size is determined by dividing this number by the line length (see Figure 4.4).

4.1.3 *Thermomechanical characterization*

This section summarizes the thermomechanical compression tests carried out to characterize material behaviour, consisting of plane strain and uniaxial compression tests, both deformation modes appearing during the NSF process. These tests are widely used to determine material properties under extreme working conditions. In addition, they are also of great interest to study recrystallization behaviour from an analytical point of view.

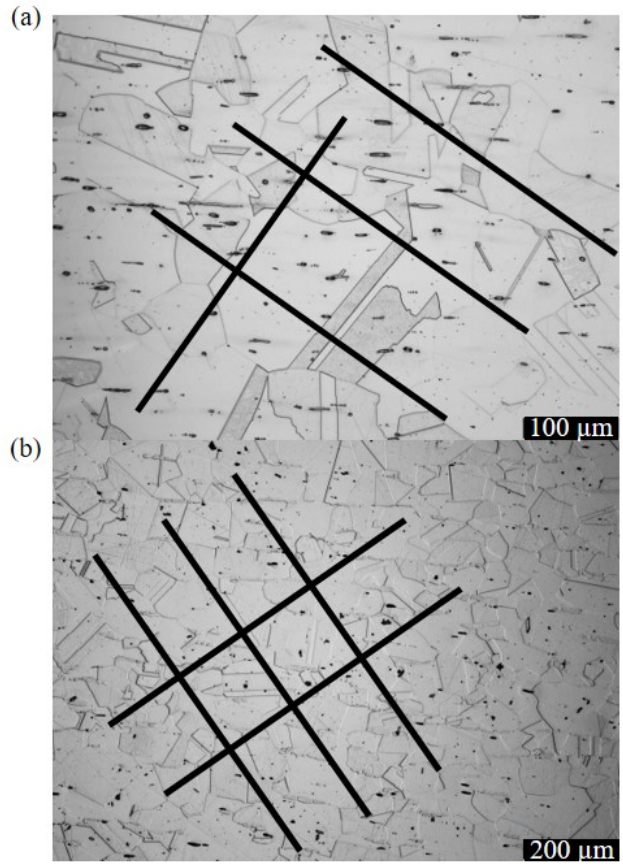

Figure 4.4: An example of the intersection method used to determine the grain sizes

Uniaxial compression tests were mainly used to determine the hot deformation constitutive parameters. Also, the flow curves obtained were used to characterize recrystallization behaviour whereas plane strain compression tests were carried out to validate from a microstructural point of view the analytical results.

4.1.3.1 *Gleeble*

Different tests using two deformations modes (plane strain and uniaxial compression tests) were carried out using the HDS-V40 thermomechanical Gleeble equipment of the Advanced Steel Research Centre of the University of Warwick (see Figure 4.5). This Gleeble has a loading capacity of 40-ton and it can achieve 1.7 m/s of stroke rate. The heating system is by Joule effect.

Plane strain compression tests are a widely used method to understand material behaviour under high conditions of strain rates and temperatures facilitating the study of microstructural evolution (Slater, Tamanna, and Davis, 2021). The dimensions used

Figure 4.5: Gleeble HDS-V40 thermomechanical equipment

in these tests are shown in Figure 4.6. For the uniaxial compression tests, the samples used were 22.5 mm in height and 15 mm in diameter.

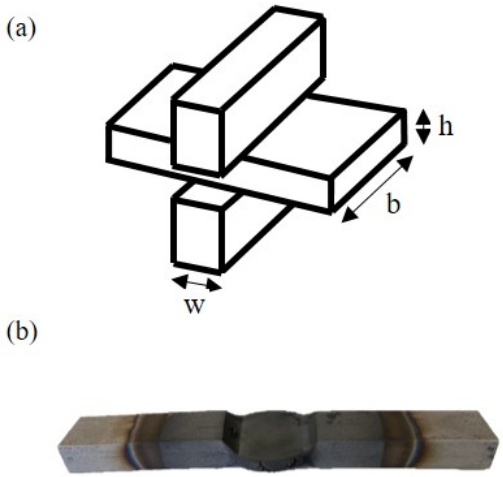

Figure 4.6: Plane strain compression samples (a) w=20 mm h=10 mm b=20 mm (b) After deformation

The samples were placed between two anvils that allowed the passage of electrical current which means the maintenance of the temperature during the tests. The heating system of this Gleeble uses a closed loop to control the temperature. To attain this aim, to do each test the temperature was controlled based on pyrometer measurement.

To carry out the experimental plan is necessary to select temperature, strain rate and heating rate. As mentioned above, the temperature range selected was from the typical range analysed in the literature to the temperatures used in the NSF process whereas for the strain rate the value was chosen according to those obtained in simulations to be representative of the NSF process. Finally, two different heating rates were chosen, one called fast (600°C/min) and the other one commercial with the aim to be as close as possible to the real heating conditions observed during the NSF process (see Figure 4.7 and Figure 4.8). It is worth mentioning that the commercial heating profile is an approximation of the real one observed when heating the billet into the muffle furnace (the real heating profile can be seen in Section 7.1).

The fast heating profile consisted of heating up the sample previously to the NSF temperature at 600°C/min. The aim of heating up the samples to that temperature is to homogenize the microstructure, that is to have the same initial grain sizes, similar to those used in the NSF process. Then the temperature was kept constant during five minutes to ensure the dissolution of precipitates. Finally, the sample was cooled down to the desire temperature at 600°C/min.

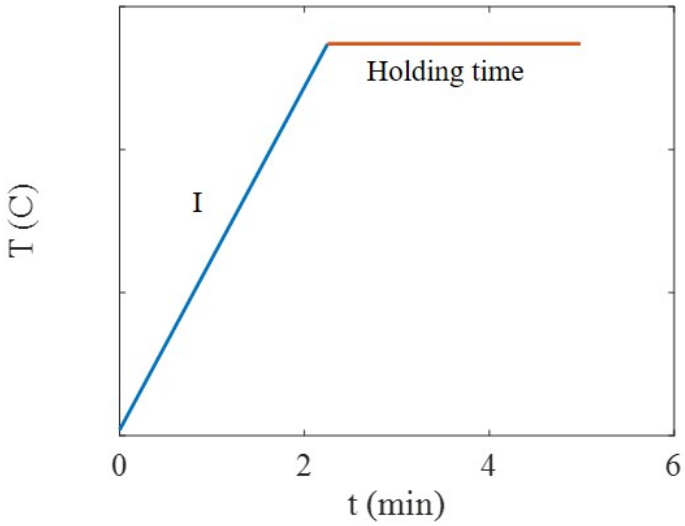

Figure 4.7: Fast heating profile using the Gleeble

The procedure followed using the commercial heating rate is the same as the previous one, changing the time at which the sample was kept at the desired temperature being one minute rather than five minutes.

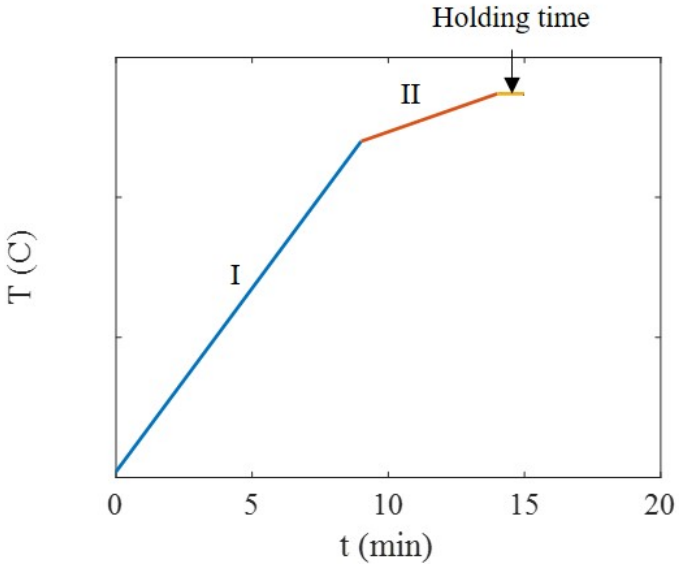

Figure 4.8: Commercial tests heating profile using the Gleeble

4.1.3.2 *Dilatometer*

Compression tests were also done using the dilatometer 805 equipment of the Mondragon University to characterize material behaviour (see Figure 4.9). These trials were complementary to those carried out with the Gleeble.

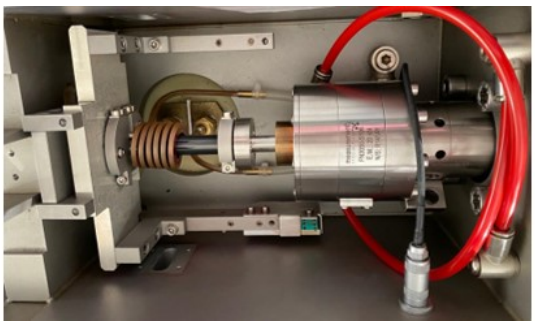

Figure 4.9: Dilatometer 805 equipment

This equipment presents the following technical specifications: 0.2-ton as maximum load and 0.2 mm/s as maximum stroke rate. Also, the heating system is based on inductive heating with constant sinus frequency. The maximum temperature available in this machine is 1700°C, the heating being controlled through a R-type thermocouple welded to the specimen.

The samples consisted of cylindrical ones with 5 mm in diameter and 10 mm in height (see Figure 4.10). They were placed between two anvils and heated based on the principle

Figure 4.10: Dilatomer samples before and after deformation

mentioned above. The tests were done in a vacuum chamber with inert gas. It is worth mentioning that all the samples were quenched with air to freeze the microstructure. The heating rate was faster than in the Gleeble and consisted of 3600°C/min and the holding time was chosen as two minutes (see Figure 4.11).

The true stress against true strain curve were obtained thanks to the force and ram displacement data acquired from the both thermomechanical simulators. The true strain is calculated using Equation (14).

$$\varepsilon = \ln\left(\frac{h_0 - d}{h_0}\right) \tag{14}$$

where h_0 is the initial height of the sample and d is the compressive displacement.

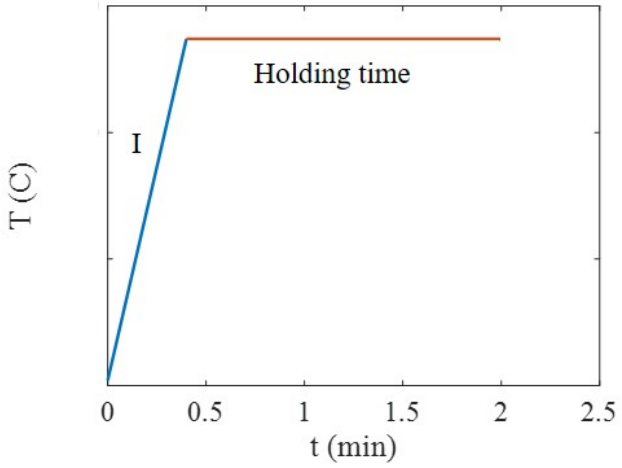

Figure 4.11: Heating profile using the dilatometer

The true stress is calculated considering the sample deformation. Assuming a constant volume of the sample and negligible barrelling, true stress can be determined according to Equation (15).

$$\sigma = \frac{F}{\pi \frac{\phi_i^2}{4}} \tag{15}$$

where the equivalent diameter of the sample at each step is as follows:

$$\phi_i^2 = \frac{\phi_0^2 h_0}{(h_0 - d)} \tag{16}$$

where ϕ_0 is the initial diameter of the sample and F is the force.

4.2 MATERIAL: AISI 316

Austenitic stainless steels present difficulties to be manufactured in comparison with other conventional steels. For instance, a 10% upset reduction in AISI 304 at 1100°C needs two times the force of AISI 1020 or 1.6 times the force of 4340 steel (Balachandran and Balasubramanian, 2013). Stainless steels are highly alloyed and have higher strength than conventional steels which hampers the forging process. Finally, austenitic stainless steels could present delta ferrite which adversely influences the forgeability. That is why a new process to manufacture stainless steel is of great interest for industry and, with the NSF process, complex parts could be obtained reducing the amount of material needed and the force required to deform the sample.

The relevance of this material to industry is not unimportant as it is widely used due to its corrosion resistance and also its formability, its strength and its properties at extreme temperatures. The formability of stainless steels under NSF conditions is expected to increase, therefore making complex designs of functional and cost-effective products in stainless steels seems feasible.

Phase changes both during deformation or quenching could take place in different alloys hampering the analysis. In this sense, austenitic stainless steels could be a possible option to avoid phase changes during the NSF process. Despite this selection, the high strain (see Plata et al., 2020) at which the billet is subjected during the process may cause changes in the material's behaviour due to recrystallization. In addition, it is not possible to harden austenitic stainless steel by heat treatment, that is why grain refinement is a key aspect in its mechanical properties.

On this basis, for this work AISI 316 samples were taken from rolled bars supplied by Acerinox. The chemical composition of the material is shown in Table 4.1.

Table 4.1: Chemical composition of AISI 316

Cr	16.5-18.5 %
Ni	10-13 %
Mn	$\leq$ 2 %
Mo	2-2.5 %
Si	$\leq$ 1 %
N	0.11 %
P	0.045 %
C	$\leq$ 0.07 %
S	0.03 %

The microstructure of the as-received bar was analysed in two directions (longitudinal and radial) and it was observed to be homogeneous. The etch process was carried out according to the procedure explained above. The microstructure consisted of austenite grains with manganese sulphides appearing as black marks. The initial grain size was 15 microns (see Figure 4.12).

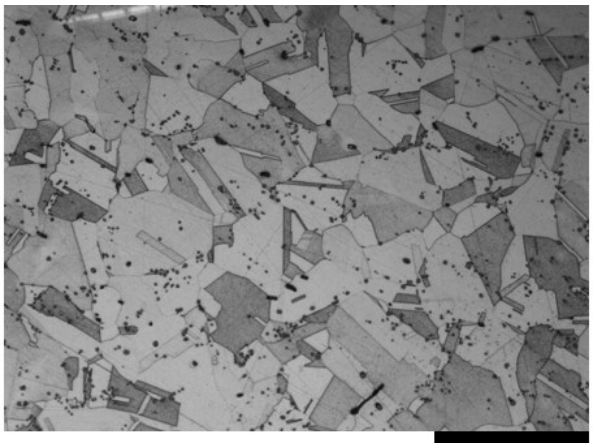

Figure 4.12: Initial microstructure of AISI 316. Scale bar: 100 µm

Therefore, among all the possible materials, austenitic stainless steels are widely used in industry although they are more difficult to be manufactured in comparison to other steels. Thus, a new manufacturing route as the use of NSF would be of great interest for industrial purposes. In addition, in order to understand the process, austenitic stainless steel does not have phase changes during heating, which may facilitate the analysis.

4.3 NSF CELL

Lozares et al., 2020 designed and manufactured the tooling for NSF of high-melting-point alloys. In Figure 4.13, the NSF cell and the tooling are shown.

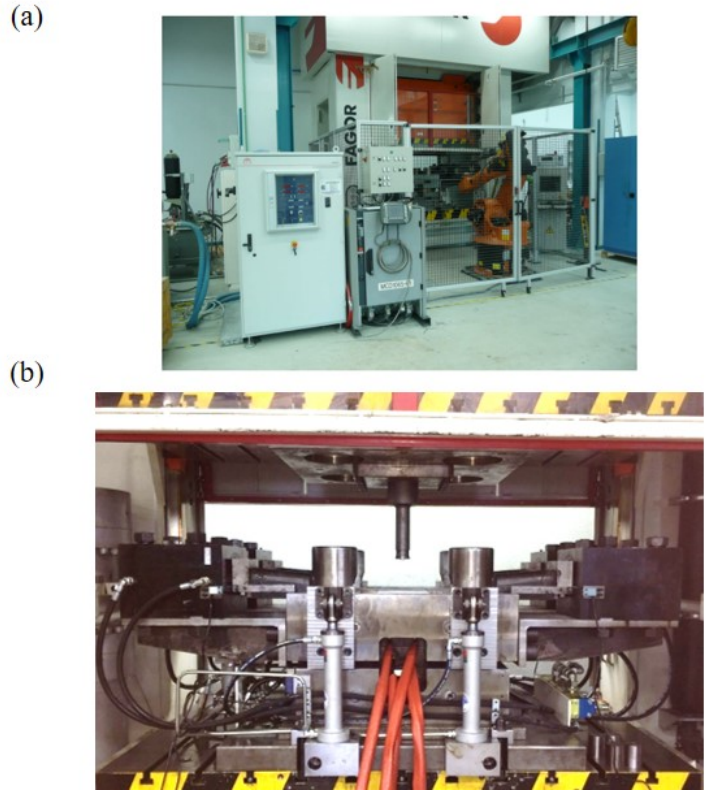

Figure 4.13: (a) NSF cell (b) Tooling for high-melting-point alloys (Lozares et al., 2020)

The press used in the cell is a Fagor servo-mechanical press whose capacity is 400 tonnes. The servo-mechanical press offers benefits such as higher productivity, high product precision and better reliability than a mechanical press. Moreover, the press employed has a flexible ram movement which permits a wide range of working cycles, this being one of the main characteristics of this type of presses. The deformation stage starts with the punch being moved from the top dead centre to the bottom one. It is worth mentioning that the maximum load is only attained in the final position, at which the punch is held for five seconds compressing the material. Table 4.2 shows the press characteristics.

With respect to the tooling, it is composed of an upper and lower die holder connected by four hydraulic cylinders which enable the die to open and close. In addition, other four hydraulic cylinders are located in the upper die holder to prevent die separation during the process. To verify the cylinder movement at the same speed and time, different flow dividers were installed. The tool is shown in Figure 4.14.

Table 4.2: Characteristics of the servo-motor-driven mechanical press

Servo motor driven mechanical press SDM2-400-2400-1200	
Press capacity (kN)	4000 at 20 mm from the Bottom Dead Center
Number of points	2
Working torque max /nominal (Nm)	5500/3000
Max stroke (mm)	400
Max ram speed (mm/s)	800
Die height (mm)	1000 to 1200 (stroke 400 mm)
Table size (mm x mm)	2400 x 1200
Max cadence (spm)	100
Die cushion capacity (kN)	400
Die cushion stroke (mm)	100
Motor power max/nominal (kW)	450/250

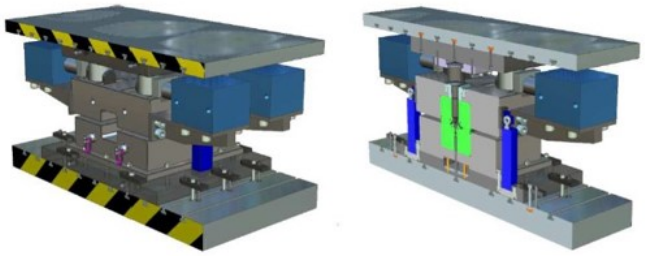

Figure 4.14: Design of tooling for high-melting-point alloys (Lozares et al., 2020)

For the process, the dies are preheated to 270°C with oil flow through the tempering channels. Then, to establish a thermal shock barrier in both dies and punch, a long-lasting ceramic varnish with lubricant was used (CeraSpray®).

One of the main factors is the heating of the billet to a temperature near the solidus. To achieve this aim, a high temperature muffle furnace was used, being 1600°C the maximum achievable temperature. Temperature calibration of the furnace was done in order to control the billet temperature during heating (see Section 4.1.2). Figure 4.15 depicts an example of the cycle used in the press.

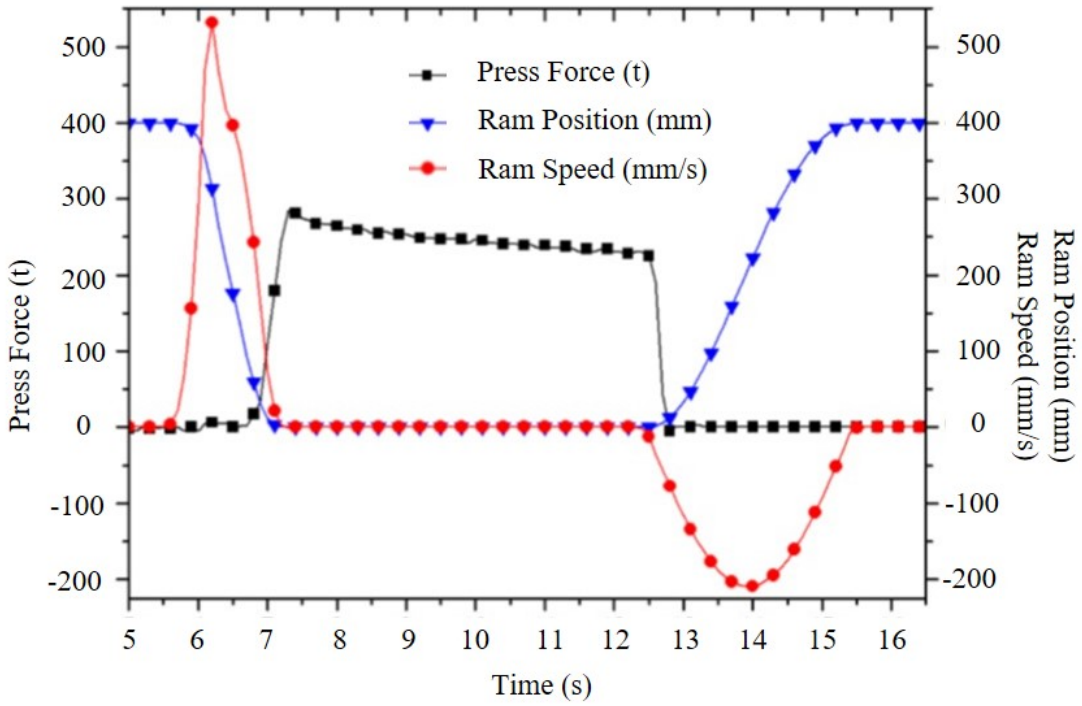

Figure 4.15: Design of tooling for high-melting-point alloys (Lozares et al., 2020)

As was mentioned above, the billet used during the process is heated up in a muffle furnace, following the heating profile explained in Section 4.1.2. The billet could be slightly cool down when it is transported from the furnace to the press.

Finally, in order to eject the component, the clamping system retraction and die opening are manually initiated once the deformation has finished and the ram is at the TDC. After the dies are separated, a pneumatic ejection system is manually activated. Then, an operator is responsible for removing the component from the press and cleaning the dies to start a new cycle (Plata, 2018).

4.4 INITIAL NUMERICAL ANALYSES

Numerical software such as Forge NXT® is a good tool to carry out a preliminary estimation of the expected conditions during the manufacturing process. On this basis, a lifting gear component (hook geometry) was chosen. The main aim of choosing the hook geometry was to have at the same time a real geometry used in the industry which allow grain sizes evolution along the part to be studied as a function of the strain reached.

Forge NXT® uses continuous remeshing and adaptive meshing because of the severe conditions expected during the process. The quality of the mesh is important to obtain accurate results. Consequently, the software applies spatial triangulation, that is, meshes are composed of 3D tetrahedra. The minimum element size in the simulation was set to 1 mm.

Furthermore, these FEM models were developed using AISI 316 from the database. The thermal conductivity, specific heat and emissivity of these materials were taken by default from Forge NXT® database.

The temperature of the dies was 270°C and the billet temperature was set to 1370°C according to Lozares et al., 2020. Lozares et al., 2020 established the working temperature to be between 0.9 and 0.95 the solidus temperature. The thermomechanical model implemented in Forge NXT® is the Hansel-Spittel law which represents the dependency of the material flow stress on strain, strain rate and temperature.

4.4.1 *Results and discussion*

The aim of this preliminary analysis is to test the capacity for the NSF process to manufacture stainless steel parts and to determine the expected conditions to define the process window to characterize material behaviour. In addition, the load mode of the whole process was also numerically analysed taking into account the triaxiality parameter, to prove the assumption that plane strain and uniaxial compression mainly take place during the process. Figure 4.16 shows the strain map in which two different zones were identified: the surface and the bulk.

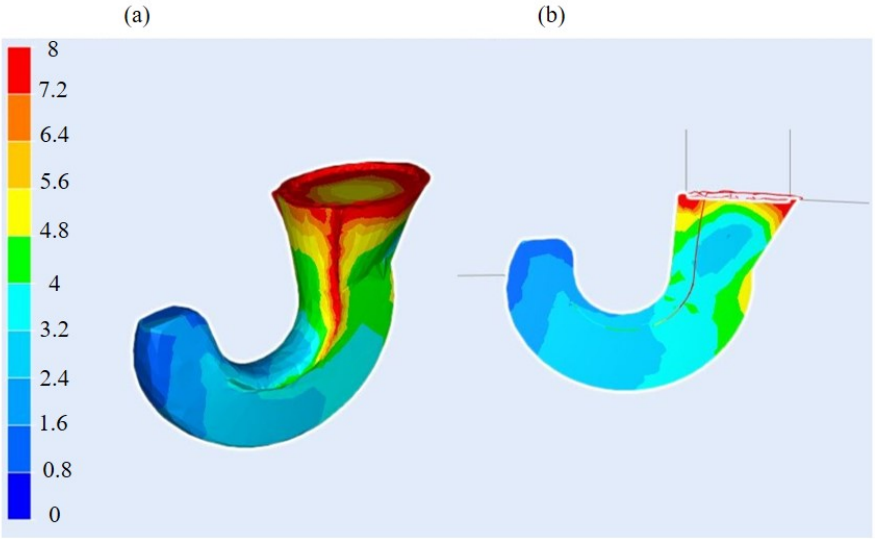

Figure 4.16: Strain fields at (a) surface (b) bulk

As mentioned above, it will be necessary to define the strain rate of the NSF process to characterize the material behaviour under these conditions. It can be seen in Figure 4.17 the strain rate map of the process.

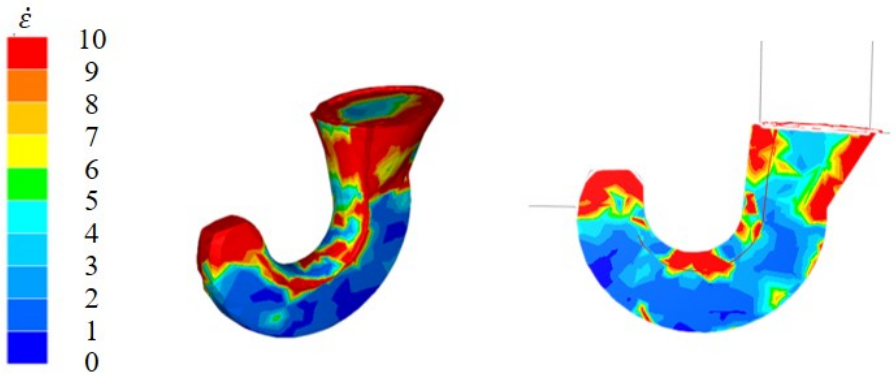

Figure 4.17: Strain rate fields

To define a representative value of strain rate to carry out the thermomechanical characterization properly, an histogram was taken from the simulation demonstrating that the vast majority of the elements were subjected to a strain rate of around ten (see Figure 4.18). That is why, 10 s^{-1} was taken as an average value for the thermomechanical characterization.

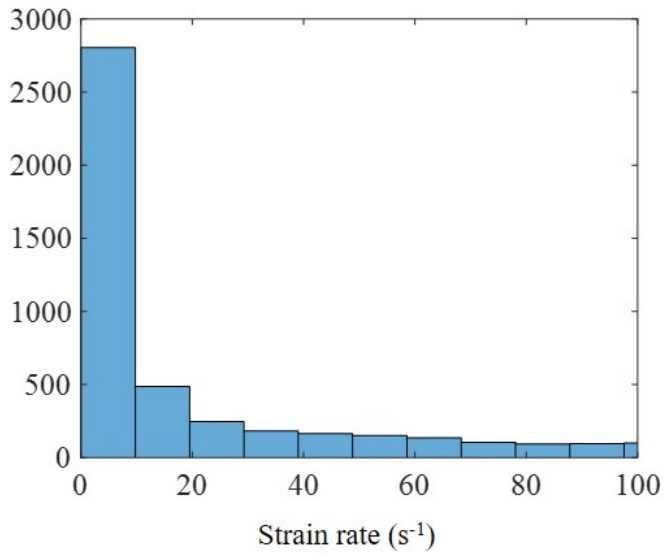

Figure 4.18: Strain rate histogram according to Forge NXT®

Another important aspect to be considered is the load mode during the process. As NSF is a complex process, the billet is subjected to different load modes. In addition, the knowledge of the load mode is relevant in order to choose how to do the characterization tests shown in Section 4.1.3.1. To characterize the load mode, triaxiality is widely used.

Triaxiality represents the ratio between the hydrostatic pressure and the equivalent stress. Thus, the triaxiality parameter (η) was calculated using Equation (17) where p is the hydrostatic pressure and q the equivalent stress. To determine these two parameters, Equation (18) and (19) were used. According to the literature, triaxiality is zero in shear mode, -1/3 in compression mode and -0.6 in plane strain mode (Bai and Wierzbicki, 2008).

To achieve this aim, a MATLAB subroutine was developed in order to determine the load modes during deformation. The stress tensor was obtained from Forge NXT® to develop this calculation.

$$\eta = \frac{-p}{q} \tag{17}$$

$$p = -\frac{1}{3}\,\mathrm{tr}([\sigma]) = -\frac{1}{3}\,(\sigma_1 + \sigma_2 + \sigma_3) \tag{18}$$

$$q = \sqrt{\frac{1}{2}\left[(\sigma_1 - \sigma_2)^2 + (\sigma_2 - \sigma_3)^2 + (\sigma_3 - \sigma_1)^2\right]} \tag{19}$$

As Figure 4.19 shows, at the beginning of deformation (25% of the process), the load mode is basically pure compression and some parts with stress triaxiality associated to plane strain are also observed. Then, in the middle of the process, shear mode also could appear in some parts of the hook but compression remains the principal load mode. Once the deformation has advanced considerably (75%), the triaxiality varies along the part between 0 and -0.6. Finally, at the end of deformation, the principal load mode is compression again.

It is worth mentioning that this premilinary analysis was carried out using the thermomechanical flow behaviour according to Forge NXT® which needs from extrapolation to go to NSF conditions. They reported that high strains would be expected during the NSF process, together with strain rates around 10 s^{-1}. In addition, the triaxiality analysis showed that uniaxial compression and plane strain deformation modes were widely common along the part, making it necessary to characterize the material under both modes.

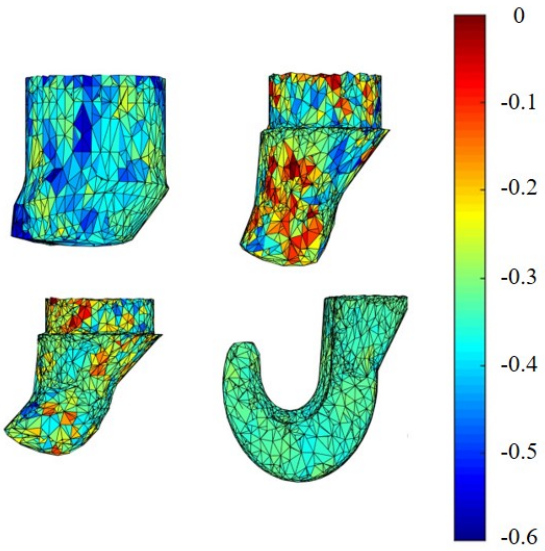

Figure 4.19: Triaxiality results at different steps during deformation

5

THERMOMECHANICAL BEHAVIOUR OF AISI 316

As has been mentioned in the literature, NSF is a novel manufacturing process which works at very high temperatures close to the solidus. However, material behaviour under these conditions is quite complex and its study is not widespread in the literature.

Samantaray et al., 2011a analysed flow curves of 304 (as-cast) and 304 stainless steel under different conditions of strain rates and high temperatures from 800 to 1200°C. As Figure 5.1 shows, both stainless steels showed thermal softening and strain rate hardening.

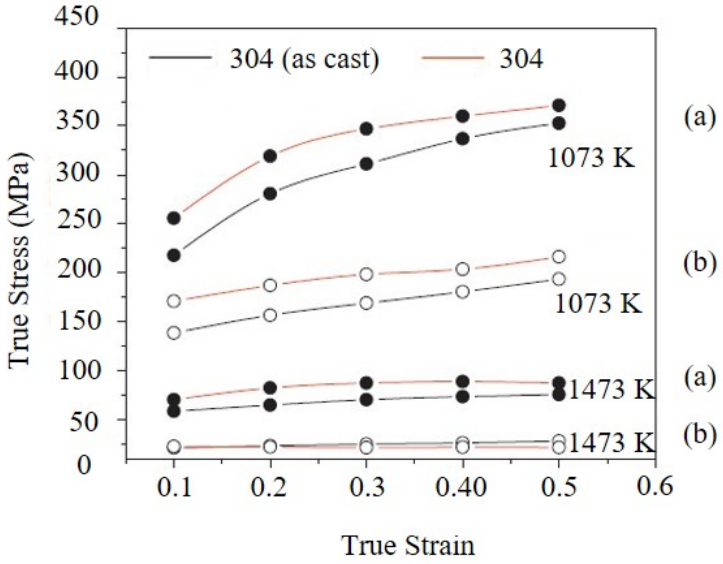

Figure 5.1: True stress- True strain curves of austenitic stainless steel at temperatures between 1073 and 1273 K and strain rates of (a) 1 and (b) 0.001 s^{-1} (Adapted from Samantaray et al., 2011a)

In addition, studying the curves of work hardening rate and temperature (see Figure 5.2) it was observed how strain hardening decreased when temperature increases. This behaviour was noted in other FCC materials (Lennon and Ramesh, 2004).

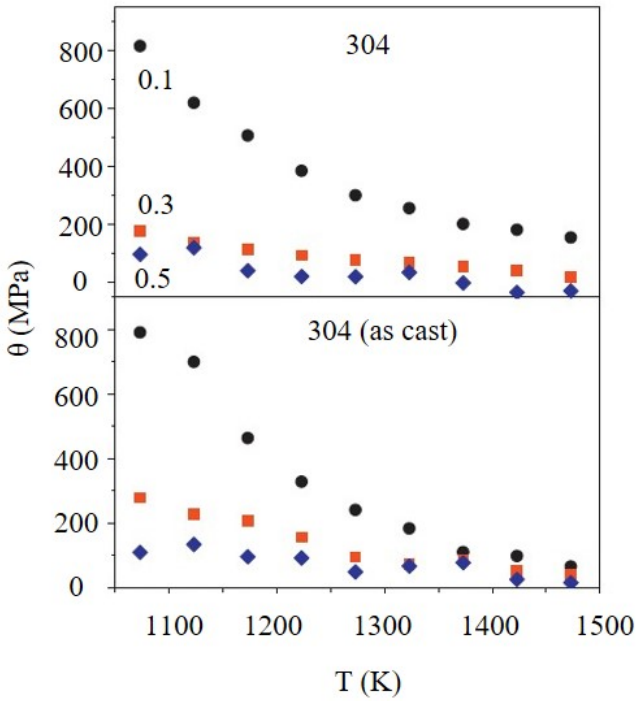

Figure 5.2: Work hardening rate (θ) vs T at 1 s^{-1} (Adapted from Samantaray et al., 2011a)

Dehghan-Manshadi, Barnett, and Hodgson, 2008a carried out research into hot deformation with austenitic stainless steel (AISI 304). The samples were deformed at temperatures from 600 to 1200°C and at low strain rates. At temperatures higher than 850°C and a constant strain rate of 0.01 s^{-1}, curves have a typical dynamic recrystallization shape while at temperatures lower than 850°C this behaviour was not evident. In contrast, at 700°C the curve shows a steady state without a peak value which could imply dynamic recovery. Finally, at 600°C the stress increases with strain until fracture which indicates continuous work hardening, probably without any kind of recovery or recrystallization.

Similar behaviour is shown at a constant temperature of 900°C and at different strain rates. The typical peak stress followed by a steady state is shown at lower strain rates which implies DRX. Strain rate hardening was also observed (see Figure 5.3).

Furthermore, Samantaray et al., 2011b studied flow behaviour using AISI 316 (see Figure 5.4). In this case, the test conditions are at different temperatures and at two strain rates (0.1 and 1 s^{-1}). These curves show thermal softening and strain rate hardening.

As has been shown, hot deformation for an austenitic stainless steel is usually accompanied by recovery and recrystallization, especially at high temperatures. That is why Hansel-Spittel (Gronostajski et al., 2017) proposed a flow stress law considering strain, strain rate and temperature as shown in Equation (1).

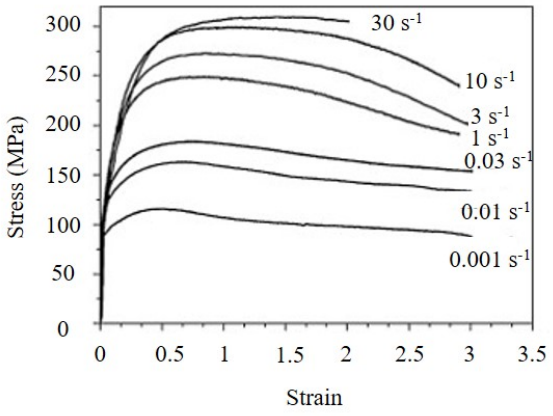

Figure 5.3: Flow curves at different strain rates and a constant temperature of 900°C (Adapted from Dehghan-Manshadi, Barnett, and Hodgson, 2008a)

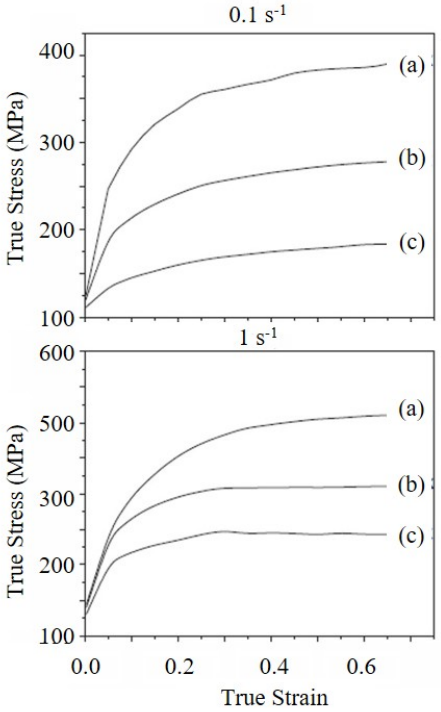

Figure 5.4: Flow curves of AISI 316 at 0.1 s^{-1} and 1 s^{-1}: (a) 1073 K (b) 1173 K (c) 1273 K (Adapted from Samantaray et al., 2011b)

This law has been implemented in Forge NXT® and that is why there is a special focus on the use of this law in stainless steel. For instance, Kang et al., 2017 carried out a comprehensive study on flow behaviour of 304 stainless steel at temperatures between 800 and 1200°C and at different strain rates. They fitted the data to the above-mentioned equation concluding the following:

- The parameter A_0 is temperature dependent and oscillates between 1100 and 2700 MPa
- The parameter m_2 and m_4 decreases with temperature and its value is from 0.55 to 0.80 for the first one and 0.007 to 0.008 for the second one
- The parameter m_3 increases with temperature changing between 0.02 and 0.12
- The parameter m_7 decreases with temperature, its value being between -2.1 and -0.9
- m_1, m_5, m_8 and m_9 are taken as zero

Kajberg and Sundin, 2013 studied flow behaviour of AISI 316 using a high-temperature Split Hopkinson pressure bar at temperatures from 900 to 1200°C and two different strain rates. They used a simple model based on Equation (1) in which m_5,m_7,m_8 and m_9 were neglected. The following values were obtained:

- A_0 has a value of 4320 MPa
- m_1 is taken as -0.00182
- m_2 is equal to 0.27
- m_3 has a value of 0.0485

Regarding Forge NXT® simulation software it is possible to see how the flow behaviour of AISI 304 is not yet included in the software whereas for 316 the following values were employed in the range of 800-1200°C and 0.01-500 s^{-1}.

- A_0 value is equal to 4320 MPa
- m_1 is taken as -0.00305
- m_2 has a value of 0.10835
- m_3 is equal to 0.08647
- m_4 is taken as -0.0127
- m_5,m_7,m_8 and m_9 are equal to zero

However, although these values were obtained for strain rates of up to 500 s^{-1}, the maximum temperature was 1200°C, making it necessary to extrapolate to reproduce NSF conditions. For similar conditions, Paquette et al., 2021 gave the following parameters:

- A has a value of 4660 MPa
- m_1 is taken as -0.00311
- m_2 is equal to -0.09996
- m_3 has a value of 0.09794
- m_4 is -0.06481

There are different techniques and laws used to model the flow behaviour of metals. However, the validity of the material law is limited to the range in which the material has been tested. As has been shown, even for similar materials (austenitic stainless steel) and using the same law, the material parameters are totally different. Thus, in order to study the material behaviour under NSF conditions it is necessary to carry out material characterization to have a proper law to reproduce the material behaviour.

On this basis, first, a thermal characterization of the material was carried out to accurately determine its solidus temperature through the DSC (see Section 4.1.1), also analysing all possible phase transformations.

Then, a thermomechanical characterization was carried out using two different thermomechanical simulators (Gleeble and dilatometer as explained in Section 4.1.3) and two dissimilar configurations (plane strain and uniaxial compression). The effect of the heating rate on material behaviour was also studied as it is a relevant aspect for the process and it is usually neglected in the literature.

Thanks to this thermomechanical analysis, the flow stress behaviour of the material was characterized covering the range of the NSF conditions. These extreme temperatures were not analysed in the literature, and extrapolations were proven to report inaccurate predictions under these conditions.

Finally, the possibility of having recrystallization was analytically studied using the stress-strain curves, and analysing the effect of relevant input parameters such as temperature, strain rate or heating rate.

Modelling of DRX consists of determining different parameters such as activation energy (Q), critical strain, recrystallized grain size or recrystallized fraction, among others. The study of DRX for AISI 316 is extensive in the literature and some examples are summarized here.

As mentioned in Section 2.3.1, Q for dynamic recrystallization could be obtained fitting Equation (7) for the material tested under the experimental conditions, i.e. different researchers defined the value of the activation energy of AISI 316 around 400 kJ mol^{-1} (Kim, Lee, and Jang, 2003; Liu et al., 2013; Dupin, Yana, and Yanag., 2014; Suker et al., 2017).

Kim, Lee, and Jang, 2003 proposed a model based on torsion tests under dissimilar conditions of temperature and strain rates. The temperature range at which the tests were carried out was from 1000 to 1200°C and the strain rate from 0.05 to 5 s^{-1}. These researchers defined Equation (20) and (21) for the critical strain and the dynamic recrystallized grain size.

$$\varepsilon_c = 0.0227 Z^{0.057} \tag{20}$$

$$d_{DRX} = 4644 Z^{-0.123} \tag{21}$$

Jafari, Najafizadeh, and Rasti, 2007 developed a dynamic recrystallization model through compression tests under different temperature conditions (950-1100°C) and strain rates between 0.01 to 1 s^{-1}. According to these results, critical strain and recrystallized grain size equations were obtained (Equation (22) and (23)).

$$\varepsilon_c = 0.0033 Z^{0.127} \tag{22}$$

$$d_{DRX} = 230 Z^{-0.097} \tag{23}$$

Other studies such as the one done by Liu et al., 2013 proposed another model taking into account results from compression Gleeble tests. These tests were carried out in the range of temperatures from 900 to 1200°C and from 0.001 to 10 s^{-1} of strain rate. This research work did not include an equation for the critical strain maybe due to the difficulties of determining it at high strain rates, without the presence of a peak in the flow stress curve. The recrystallized grain size equation is shown in Equation (24).

$$d_{DRX} = 1.01 \cdot 10^5 Z^{-0.24} \tag{24}$$

Dupin, Yana, and Yanag., 2014 carried out single compression tests in the temperature range of 950-1150°C and from 0.01 to 20 s^{-1} of strain rate. Thus, Equation (25) shows the critical strain equation and Equation (26) represents the recrystallized grain size.

$$\varepsilon_c = 0.019 Z^{0.09} \tag{25}$$

$$d_{\mathrm{DRX}} = 27000\dot{\varepsilon}^{-0.2}\exp\left(\frac{-13000}{T}\right) \tag{26}$$

Other researchers such as Zhang et al., 2015 studied AISI 316 using single compression tests under different conditions of temperature (900-1200°C) and strain rate (0.1-10 s^{-1}). This investigation developed the relationship between critical stress and Z and, also, d_{DRX} and Z.

$$\sigma_c = 15.9\ln(Z) - 495 \tag{27}$$

$$d_{\mathrm{DRX}} = 1.3 \cdot 10^4 Z^{-0.22} \tag{28}$$

Wang et al., 2016b developed another model based on compression tests at temperatures from 900 to 1250°C and at strain rates between 0.01 to 1 s^{-1}. The critical strain model was not included, these researchers used by default the relationship between the critical and peak strain (see Equation (11)). Moreover, the recrystallized grain size is modelled obtaining Equation (29).

$$d_{\mathrm{DRX}} = 20975.492 Z^{-0.19324} \tag{29}$$

Summarizing, Table 5.1 embraces the conditions mainly analysed in the literature with regard to recrystallization modelling and the different DRX grain size laws, proving that no agreement was found between researchers.

Table 5.1: Summary of the main conditions employed in literature to characterize DRX kinetics in AISI 316

Ref.	**T(°C)**	$\dot{\varepsilon}(s^{-1})$
Kim, Lee, and Jang, 2003	1000-1200	0.05-5
Liu et al., 2013	900-1200	0.001-10
Dupin, Yana, and Yanag., 2014	950-1150	0.01-20
Jafari, Najafizadeh, and Rasti, 2007	950-1100	0.01-1
Zhang et al., 2015	900-1200	0.1-10
Wang et al., 2016b	900-1250	0.01-1

To conclude, it was demonstrated that austenitic stainless steel is known for dynamic recrystallization to occur, especially when the process is carried out at high temper-

atures and when high strains are achieved. These conditions are typical in the NSF process as was proven in Section 4.4. However, the parameters to model DRX behaviour differ among the researchers as they are highly dependent on the initial microstructure, material properties or testing conditions. That is why, it is necessary to determine the recrystallization behaviour of the material under NSF conditions in order to have reliable models.

5.1 DIFFERENTIAL SCANNING CALORIMETRY

As mentioned above, the main aim of this DSC analysis was to determine the material solidus temperature and to analyse possible phase changes during heating. According to literature review, the solidus temperature is around 1420°C. The experimental sequence consisted of a cycle which was composed of different segments. First, to heat a sample of 50 mg at a rate of 10°C/min up to 1450°C in order to melt it, followed by a slow cooling at the same rate. A more detailed explanation of the methodology can be seen in Section 4.1.1.

The first heating segment showed a linear trend without the presence of phase changes. This first analysis showed that AISI 316 could be a potential choice to study the phenomena which explain NSF process avoiding the intrinsic difficulties of having phase changes. This statement could be extrapolated to any other austenitic stainless steel. Finally, as Figure 5.5 shows, the solidus temperature was 1435°C. In addition, at around 1400°C a slight variation was observed in the graph which could be related to the appearance of delta ferrite as it is a common phase in this alloy. It is worth mentioning that this analysis was carried out under equilibrium conditions.

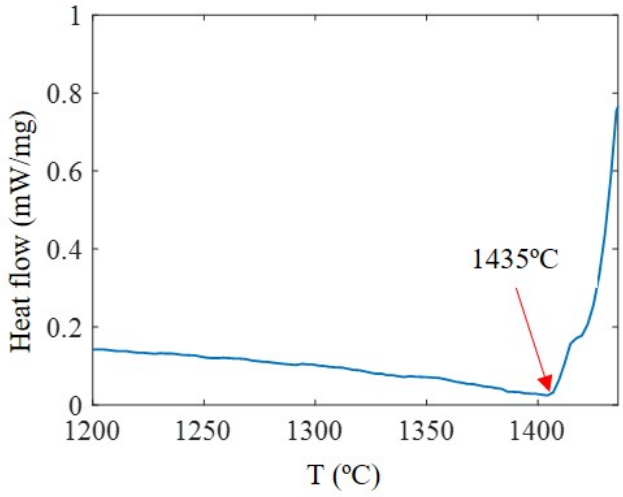

Figure 5.5: Solidus temperature of AISI 316

Moreover, a simulation was launched using FactSage. The results are shown in Figure 5.6. As can be seen, the results are in agreement with the experimental ones, both reporting the same solidus temperature. However, with regard to the delta ferrite, slight discrepancies were observed as, according to simulation, delta ferrite tends to appear around 1320°C. These results are of great relevance in order to define the working temperature range.

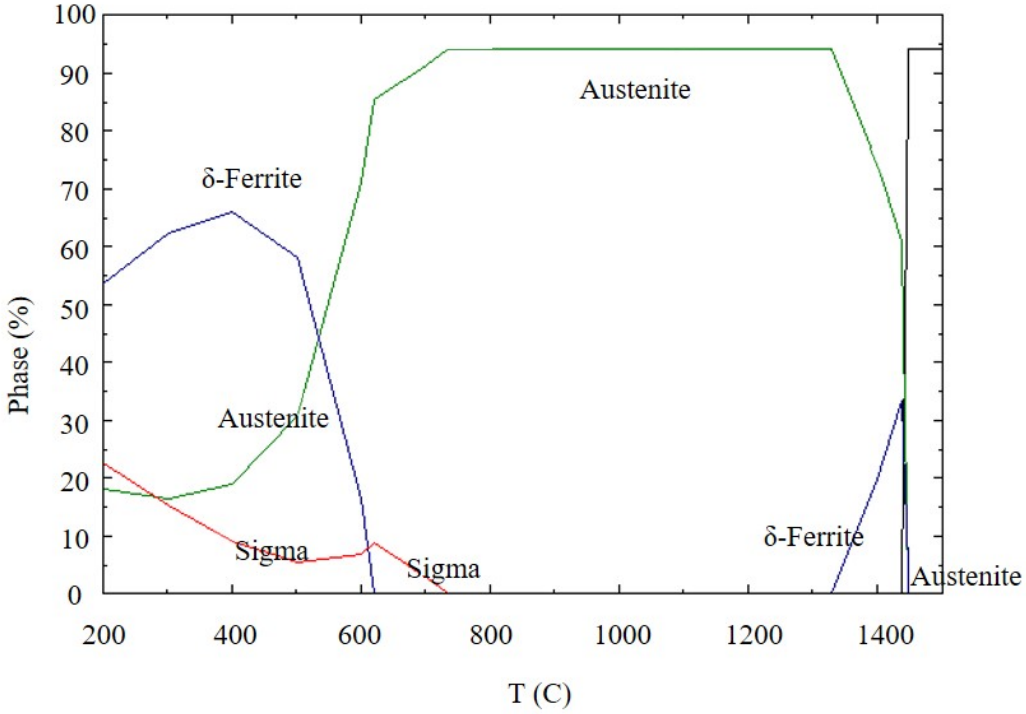

Figure 5.6: Phase diagram of AISI 316 using Factsage

These results are of special interest as they allow the temperature of the NSF process to be determined. According to Lozares et al., 2020, the process temperature ought to be around 0.95 the solidus temperature. Under these conditions, Plata, 2018 demonstrated that NSF worked for different steel grades. On this basis, taking into account the knowledge acquired from previous experiences and the results obtained, the optimum process temperature should be 1370°C.

5.2 THERMOMECHANICAL ANALYSIS

The main aim of this section is to analyse the material behaviour of the AISI 316 from the typical temperature range which appears in the literature to that found in the NSF process. Uniaxial compression tests were chosen to carry it out. Although plane strain

compression tests were also done as was explained in Section 4.1.3, these tests were used to carry out the microstructural analysis due to the fact that the plastic strain was demonstrated by Slater, Tamanna, and Davis, 2021 to be more uniform along the sample.

Uniaxial compression tests are widely used to determine material properties under extreme working conditions. In addition, these tests are also of great interest when studying recrystallization behaviour from an analytical point of view. That is why, these tests were done in parallel with the plane strain ones in order to complement the results. Therefore, these tests were mainly used to determine the hot deformation constitutive parameters. Also, the flow curves obtained were used to characterize recrystallization behaviour in uniaxial compression and the microstructures were taken to validate the analytical results. It is worth mentioning that all these tests were done up to a strain of 1.

For the dilatometer (see Section 4.1.3.2), the tests were done in a vacuum chamber with inert gas. It is worth mentioning that all the samples were quenched with air to freeze the microstructure. As Section 5.1 shows, the NSF temperature was 1370°C, that is why all the samples were heated up to that temperature to have the same initial grain sizes at the beginning of the test. In terms of heating rate and holding time, the tests were organised as follows (see Figure 5.7):

- 3600°C/min up to 1370°C and 2 min of holding time.
- Then, 3600°C/min up to the desired temperature: 1100, 1200, 1250, 1300 and 1370°C.
- After the trial, the sample was quenched in air at 12000°C/min.

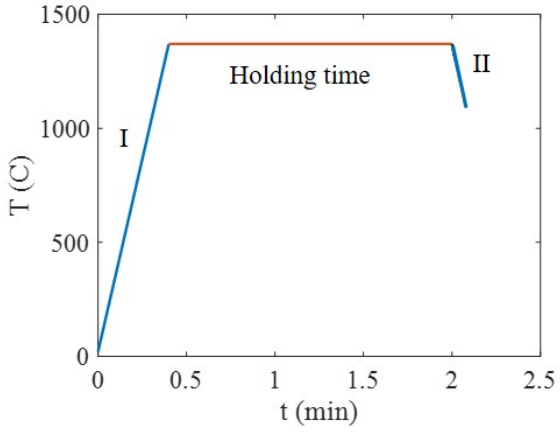

Figure 5.7: Heating profile using the dilatometer: (II) from 1100 to 1370°C

As mentioned above, the main aim of doing these tests was to analyse the flow behaviour under the typical temperature conditions which appear in the literature and the NSF temperatures (see Figure 5.7).

To determine the material parameters (see Equation (4), (5) and (6) in Chapter 2) different temperatures and strain rates were selected. The temperature range chosen was between 1100 and 1370°C, previously heated up to 1370°C to achieve the same initial grain sizes used during the NSF process. Moreover, the strain rates selected were 0.1, 1 and 10 s^{-1} in order to cover up to the strain rate observed during the process and to ensure recrystallization (it is assumed that at lower strain rates the critical strain for recrystallization would be lower) providing enough points to determine material behaviour. It should be highlighted that no research was found in the literature covering these extreme conditions.

Also, with the aim of being as close as possible to the real heating conditions observed during the NSF process, different tests (commercial tests) were carried out with the following heating profile (see Figure 5.8). The commercial tests were carried out using the Gleeble as these conditions were not possible to achieve with the dilatometer as, due to the slow heating rate, the sample spent too much time subjected to high temperatures which caused the thermocouple to fail because of the lack of welding generating high temperature peaks resulting in a partial melting of the sample. For these trials, the strain rate was 10 s^{-1} according to the FEM results showed in Section 4.4.

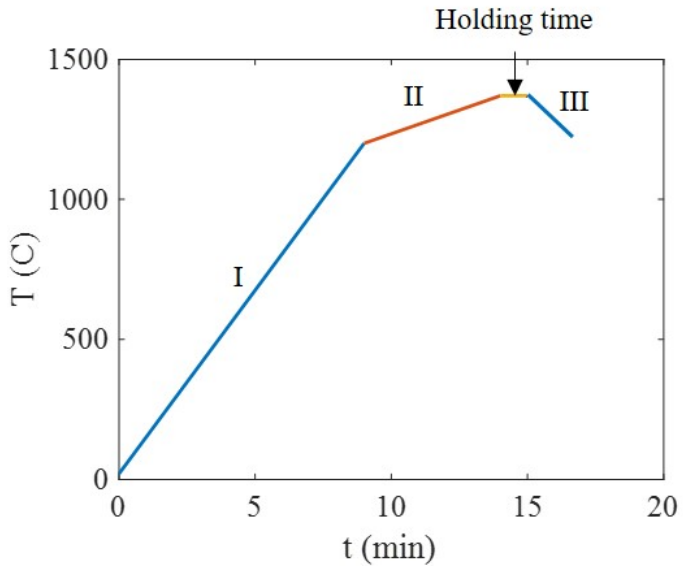

Figure 5.8: Commercial tests heating profile using the Gleeble: (III) from 1200°C to 1370°C

In terms of heating rate and holding time, the commercial tests were organised as follows:

- From 25°C to 1200°C: 130°C/min

- From 1200°C to 1370°C: 12°C/min
- Time maintenance: 1 min. As the heating rate is lower in comparison with the one previously explained, one minute was assumed to be enough to ensure dissolution of precipitates.
- From 1370°C to the desired temperature (1200°C, 1250°C, 1275°C, 1300°C, 1330°C and 1370°C): 96°C/min

5.2.1 *Flow stress behaviour: results*

The objective of this section is to analyse the influence of the temperature, strain and heating rate on the flow behaviour of AISI 316.

Influence of temperature and strain rate

The stress-strain curves from the dilatometer for AISI 316 at the range of temperatures analysed are shown in Figure 5.9 and Figure 5.10 for the whole set of strain rates analysed.

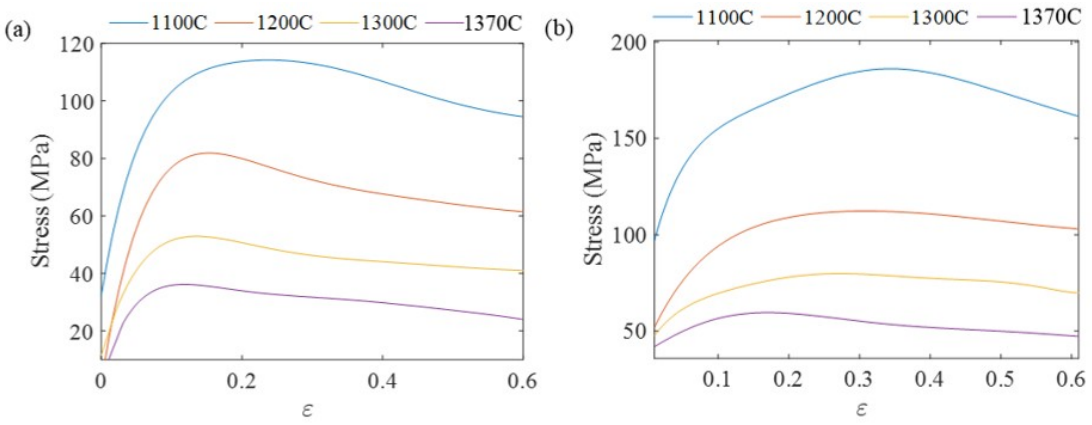

Figure 5.9: Flow stress curves in the dilatometer: (a) 0.1 s^{-1} (b) 1 s^{-1}

Regardless of the strain rate a clear thermal softening effect was observed in the whole range of temperatures. Therefore, if it would be possible to ensure good mechanical properties thanks to recrystallization processes, high temperatures could be a good option to carry out NSF tests making the deformation process easier.

With regard to the strain rate, it can be observed in Figure 5.9 and Figure 5.10, that, regardless of the temperature, there is clear strain rate hardening. This means that the material is more difficult to deform when the strain rate is higher. This issue should be taken into account in the NSF process as strain rates associated with this manufacturing process tend to be high.

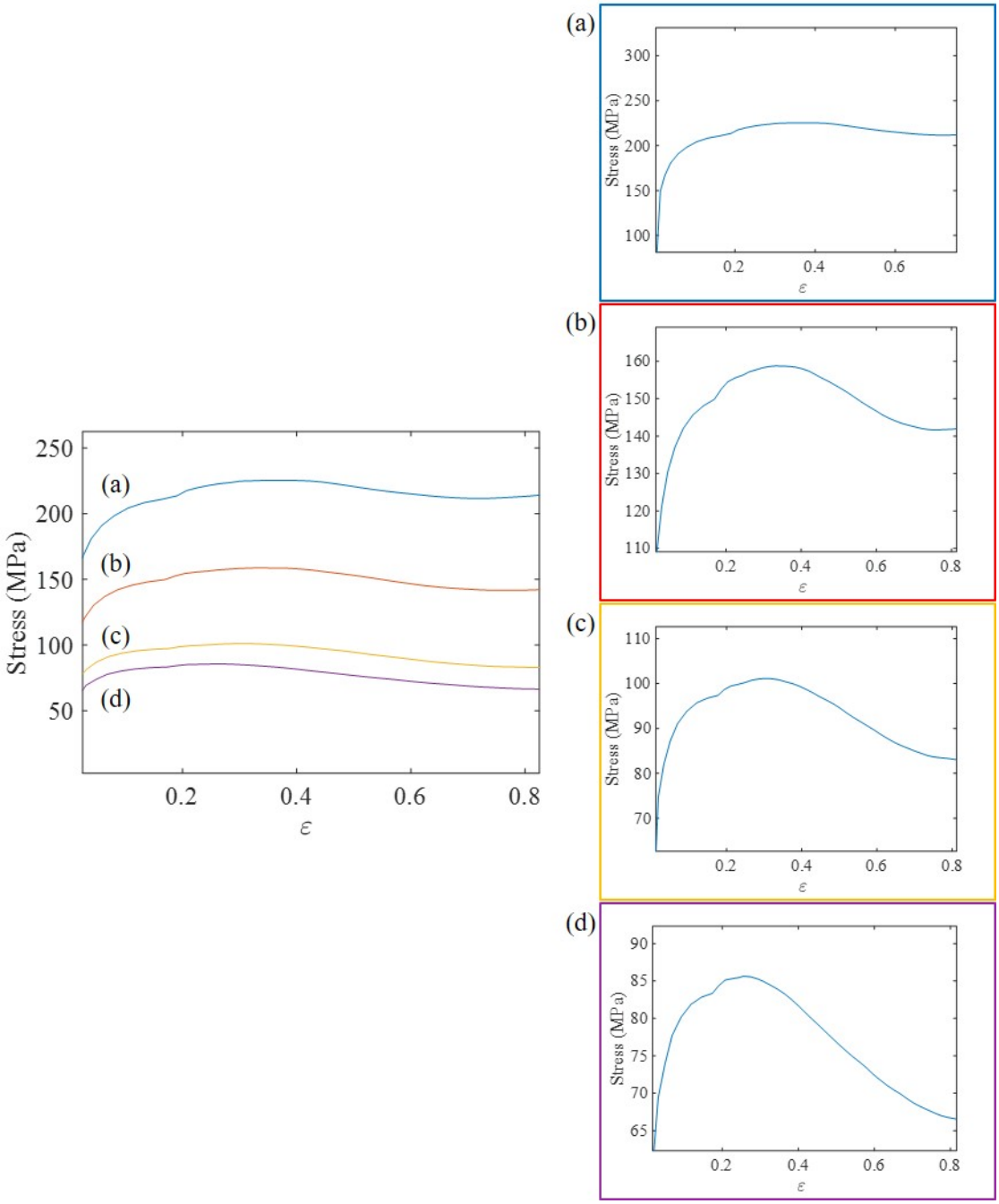

Figure 5.10: Flow stress curves at 10 s^{-1} in the dilatometer: 1100°C (blue), 1200°C (red), 1300°C (yellow) and 1370°C (purple)

Nevertheless, one of the main reasons that the forging industry avoids high temperatures is because of the formation of delta ferrite, which could be detrimental for the

process. At these high temperatures delta ferrite formation was observed (see Figure 5.5).

Influence of heating profile

Heating up the billet is one of the main stages related to the NSF process. Therefore, the aim of this section is to briefly analyse the effect that heating rate could have on material flow behaviour and, thus, on process performance. To achieve this aim, the commercial tests were carried out in the Gleeble machine and these results were compared with those obtained from the dilatometer (see Figure 5.11).

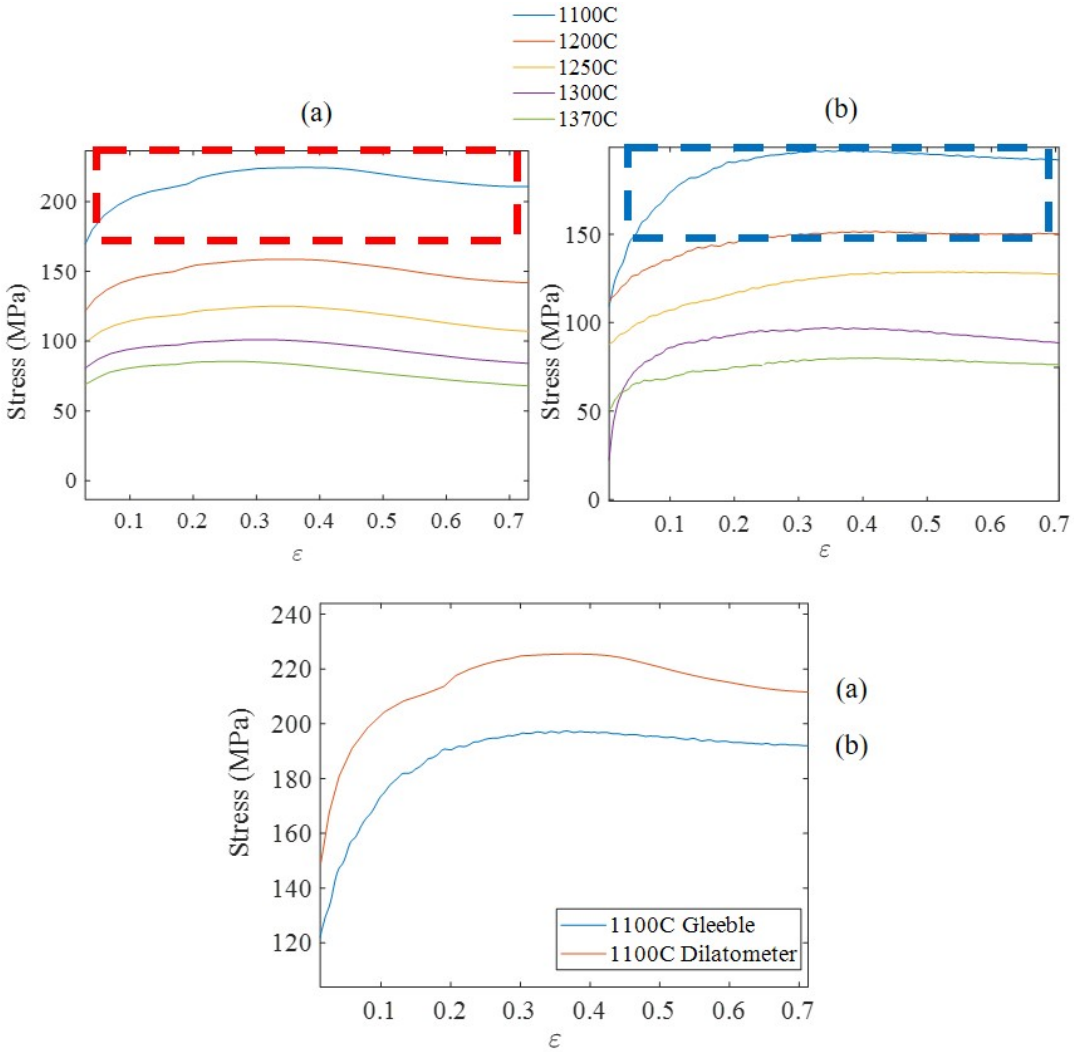

Figure 5.11: Comparison between flow stress curves: (a) Dilatometer (b) Gleeble

As can be seen, the same trend was obtained, as expected, using both machines. In general, the results were in the same order of magnitude but under all the conditions tested, higher stresses were observed when using the dilatometer. This behaviour is assumed to be due to the influence of the heating rate.

5.2.2 *Flow stress behaviour: discussion*

To analyse the thermal softening effect more deeply, peak values of stress were compared at different temperatures for the dissimilar strain rates. As can be seen in Figure 5.12, the thermal softening rate is similar for each strain rate. Therefore, this thermal softening is assumed to be related to microstructural issues instead of mechanical ones.

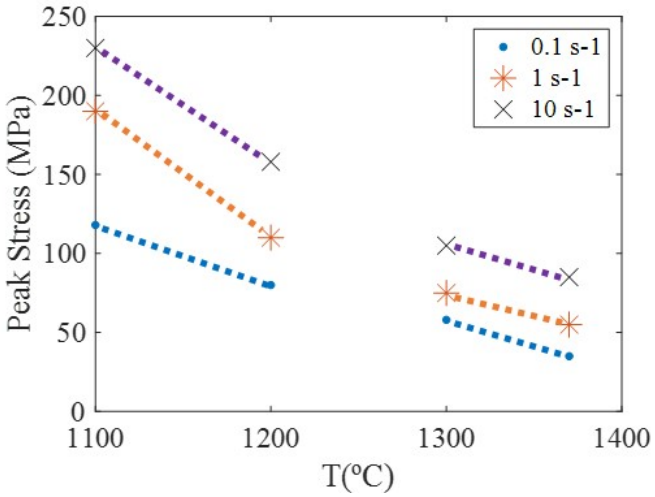

Figure 5.12: Peak stress under dissimilar strain rate conditions: 0.1 s^{-1} (dot), 1 s^{-1} (star) and 10 s^{-1} (cross)

However, although the trends reported for the different strain rates were similar, all of them showed a change in the trend when the temperature was closer to the NSF conditions. This was highlighted in Figure 5.12. This effect is assumed to be due to the formation of delta ferrite during the heating which could not be totally diluted after the cooling, as was observed in the DSC analysis that delta ferrite tended to appear around the NSF working temperature under equilibrium conditions. Therefore, although the heating up to 1370°C aimed to homogenize the initial microstructure, delta ferrite formation could have an impact on the flow behaviour. This will be analysed and discussed more in depth in Chapter 6.

Nevertheless, apart from the possible differences in a delta ferrite fraction at the beginning, this phase could nucleate easier depending on the working conditions. For instance, Venugopal, Mannan, and Prasad, 1996 or Soleymani, Ojo, and Richards, 2015 stated that higher strain rates and temperatures might result in the formation of a higher

amount of delta ferrite. This may explain the aforementioned change in trend. To corroborate this assumption, as no literature data was found at these extreme temperatures, different microstructures were taken from the centre of the deformed sample which were quenched in air as stated in Section 4.1.3.2. The microstructures obtained are shown in Figure 5.13 in which the delta ferrite phase is highlighted with a red arrow and the austenite grains with a blue arrow.

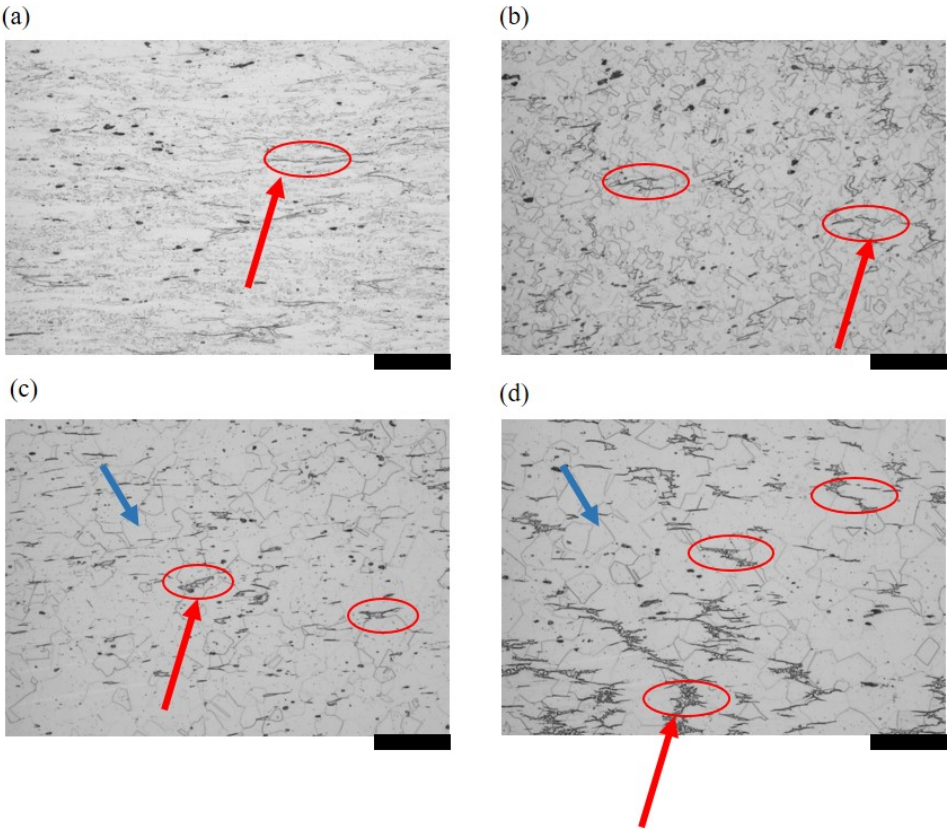

Figure 5.13: (a) 1100°C (b) 1200°C (c) 1300°C (d) 1370°C. Scale bar: 100µm

It is worth mentioning that Figure 5.13 shows the results for a strain rate of 10 s^{-1} which were the conditions which reported a more pronounced change between the two slopes differentiated (see Figure 5.12). As can be seen, especially for the tests at 1370°C, a high amount of delta ferrite was observed (see Figure 5.14), justifying the obtained results.

Again, analysing more in depth the effect of the strain rate, the values of the peak stress were plot against strain rate for the different temperatures (see Figure 5.15). As can be seen, the same behaviour was observed for all the temperatures. However, the strain rate effect, as expected, was not linear, being more pronounced at lower strain rates. This drastic change observed between 0.1 and 10 s^{-1} is assumed to be due to

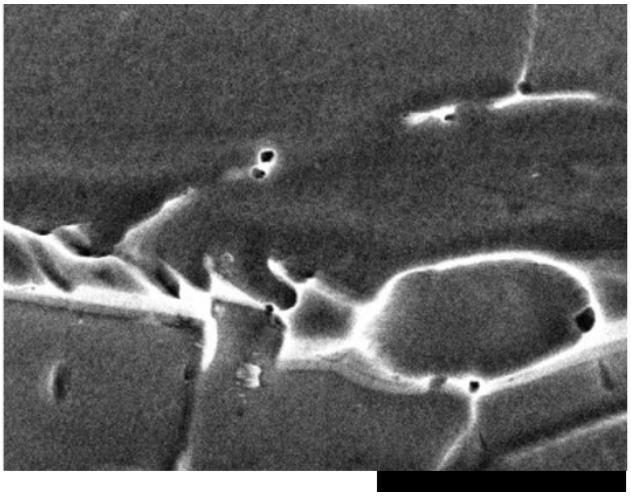

Figure 5.14: Delta ferrite phase. Scale bar: 10μm

the higher amount of delta ferrite formed at high strain rates as stated by Venugopal, Mannan, and Prasad, 1996 and observed in Figure 5.13.

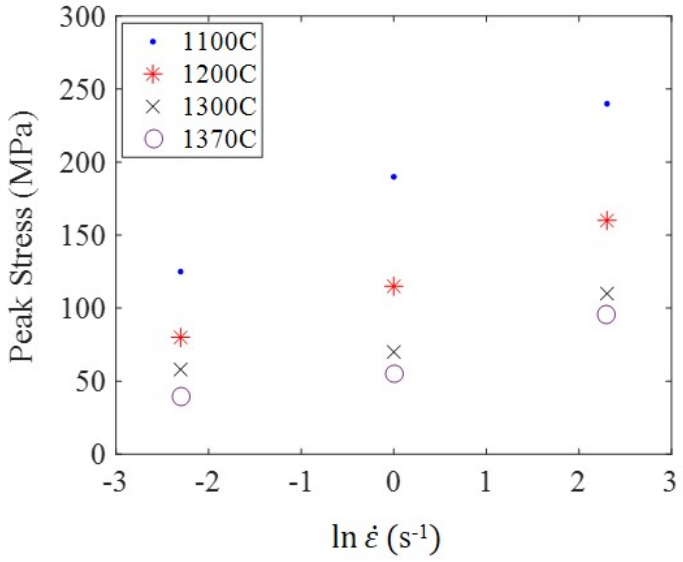

Figure 5.15: Peak stress at: 1100°C (dot), 1200°C (star), 1300°C (cross) and 1370°C (circle)

With regard to the heating profile, the one followed in the dilatometer, as was explained in Section 4.1.3.2, is much faster (around thirty times) than the one used in the Gleeble. Thus, the sample was more time subjected to high temperatures in the Gleeble test and the initial microstructure is assumed to present higher grain sizes with a high amount of delta ferrite thanks to having more time for nucleation and growing.

For instance, Figure 5.16 shows the microstructure at 1370°C for both cases measured with the optical microscope according to the methodology explained in Section 4.1.2. As can be observed, the grain sizes were 45 µm for the dilatometer case and 55 µm for the Gleeble test, being the delta ferrite highlighted with a red arrow in Figure 5.16.

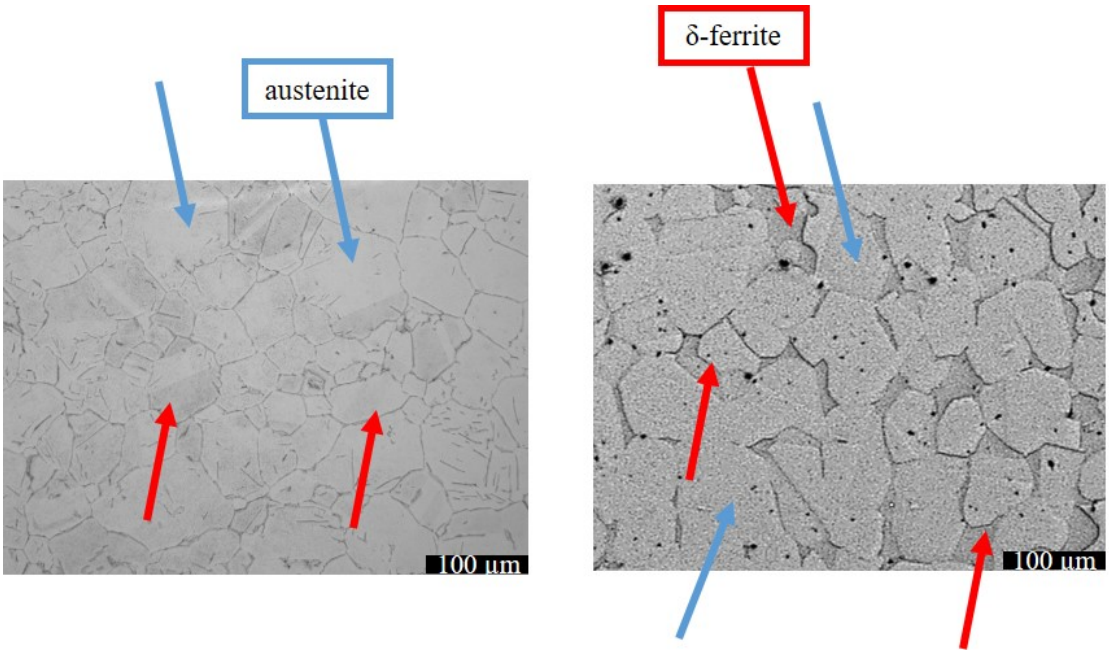

Figure 5.16: Initial microstructure at 1100°C: (a) Dilatometer (b) Gleeble

According to Guo et al., 2012 and Liu, Li, and Dang, 2013, based on the discrepancies observed in the microstructure, no remarkable differences would be expected on the flow stress behaviour. In general, taking peak stresses as reference, the deviations were in the range from 10 to 15%, being lower for the Gleeble test. This reduction is associated with having higher initial grain sizes but just the slight differences on the initial grain sizes could not explain such variations. As these differences were slightly higher than the ones reported by Guo et al., 2012 it could be expected that another effect apart from the differences on the grain size is playing a role.

As can be observed in Figure 5.16, together with the differences on grain size, the sample heated up at the slowest heating rate also presented high amount of delta ferrite on the austenite grain boundaries. This phase could also have an influence on the softening seen, that is why the microstructure of the deformed samples was again analysed, as can be seen in Figure 5.17, in which delta ferrite phase is highlighted with a red arrow being on the left the dilatometer microstructures and on the right the Gleeble ones, proving that Gleeble microstructure presented higher amount of delta ferrite.

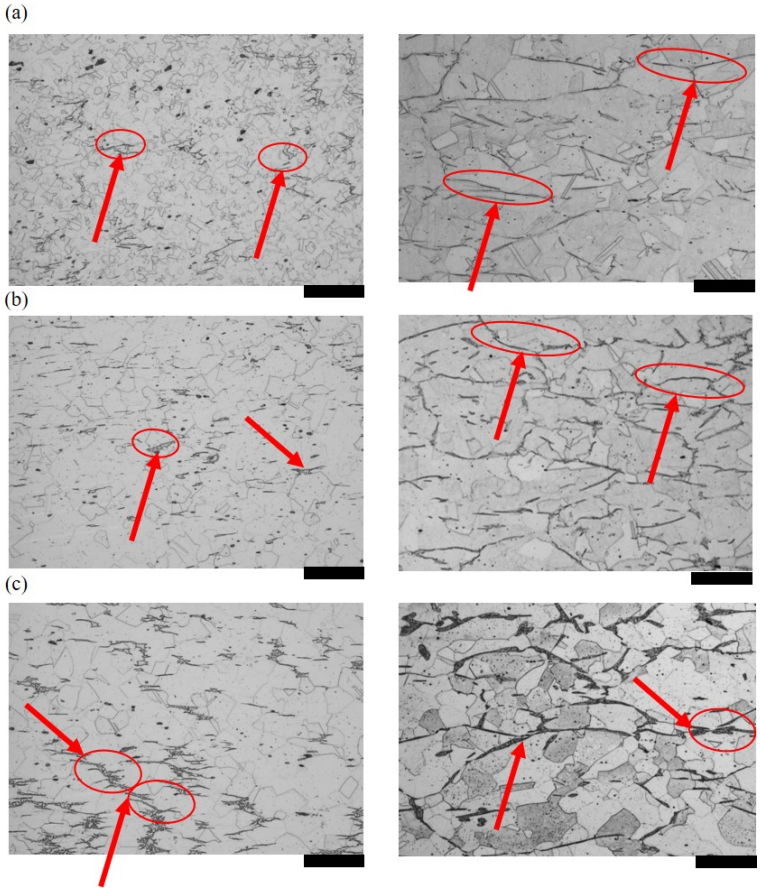

Figure 5.17: (a) 1200°C (b) 1300°C (c) 1370°C. Scale bar: 100µm

As can be observed, for all the conditions carried out in the Gleeble, higher amount of delta ferrite was obtained which could be associated with a reduction in the flow stress. These results are in agreement with those reported by Park et al., 2013.

5.3 MATERIAL BEHAVIOUR MODELLING

It would be of great interest to characterize material flow behaviour under extreme conditions reached during the NSF process as was observed based on the literature review that the commonly tested conditions are still far from those expected in the NSF process as was stated in Section 4.4.

5.3.1 *Hansel-Spittel law under NSF conditions*

As can be seen at the beginning of this chapter, the values of the material constants notably differ among researchers. To characterize the material behaviour it is necessary to have results of flow stress under different conditions of strain rate and temperature. On this basis, the dilatometer results were employed both to compare the predictions with the experimental results and to optimize Hansel-Spittel parameters up to NSF conditions. The predicted results using the parameters aforementioned were compared with the experimental ones as Figure 5.18 shows.

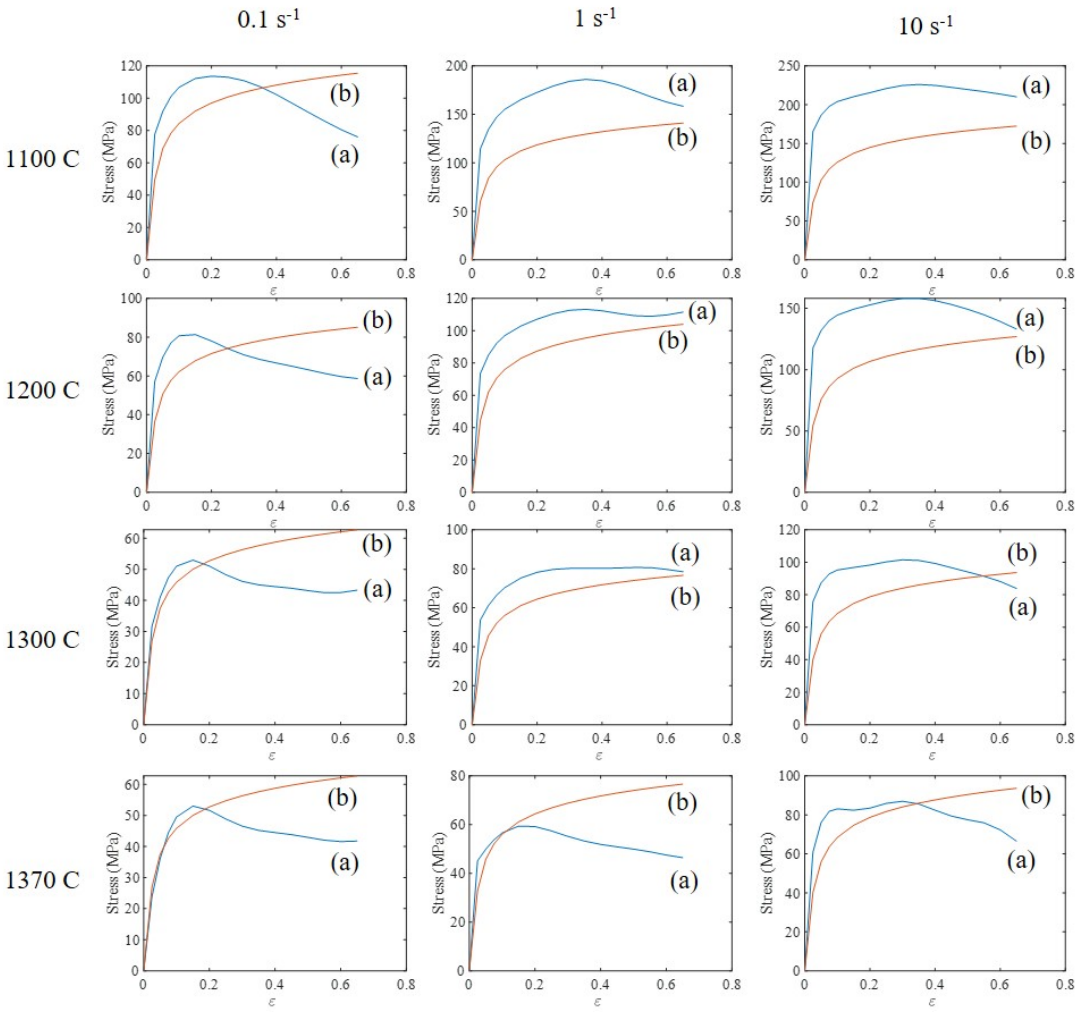

Figure 5.18: Flow stress curves: (a) Dilatometer compression test (b) Hansel-Spittel predictions with Forge NXT® parameters

In general, no agreement was found between experimental and predicted values. Therefore, it seems clear the necessity of characterizing material behaviour at these temperatures, not widely analysed in the literature.

Thus, the dilatometer tests were used to model the dependence of stress with strain, strain rate and temperature under these conditions. The results were fitted using Generalized Reduced Gradient (GRG) method for non-linear problems (Romeo, 2019).

For each condition, the experimental results were compared with those predicted using the parameters proposed in Forge NXT®, and the absolute errors in the predictions were calculated. After doing so, the objective function was defined as the sum of the prediction errors for each condition, aiming to minimise it.

After adding the necessary constraints, the solver was launched varying all possible material constants included in Equation (1). In order to ensure the reliability of the results, the material parameters proposed in Forge NXT® software were used as seed for the algorithm.

Once the algorithm finished, the following material parameters were reported:

- A= 4321 MPa
- m_1= -0.003004
- m_2= 0.1
- m_3= 0.16157
- m_4= -0.01

5.3.1.1 *Hansel-Spittel law under NSF conditions: discussion*

Although the variations could seem low, they resulted in a reduction in the total error by more than half, which would result in a notable increase in the accuracy of the predictions as can be seen in Figure 5.19. It is easy to see that the predictions reported in Figure 5.19 are clearly more accurate than those shown in Figure 5.18 for all the conditions tested, especially at higher strain rates.

Analysing more in depth the results, it can be seen that the variations for low strain rates, and more specifically for 0.1 s^{-1}, the increase on the accuracy is not so much pronounced whereas at 1 and 10 s^{-1} the errors were notably reduced.

The accuracy of the proposed method was validated comparing the experimental results obtained at 1250°C and 10 s^{-1}, as this condition was not included in the optimization algorithm. In Figure 5.20, the results obtained using the calculated material parameter are shown compared with those predicted using Forge NXT® parameters, Faini, Attanasio, and Ceretti, 2018 and Paquette et al., 2021, for the same steel grade. As can be seen, the prediction with the values taken from the literature and also with the values employed by Forge NXT® were notably inaccurate. Thanks to the proposed optimization the prediction error was reduced by more than half.

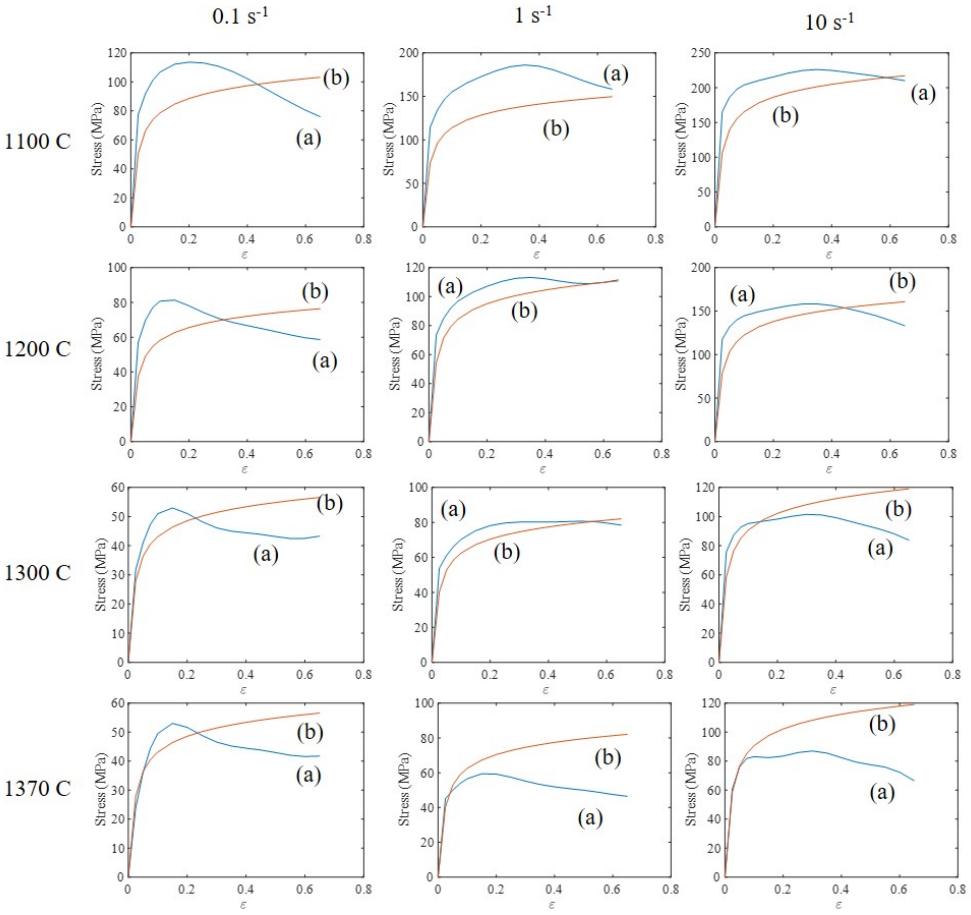

Figure 5.19: Flow stress curves: (a) Compression test (b) Model prediction

Although the results obtained in this section are promising and can improve the accuracy on the predictions using FEM software, it is worth mentioning that the model proposed just considers the effect of strain, strain rate and temperature, being not able to properly reproduce the shape of the stress-strain curve due to the effect of recrystallization during deformation. That is why, in the following section, the recrystallization phenomenon will be deeply analysed.

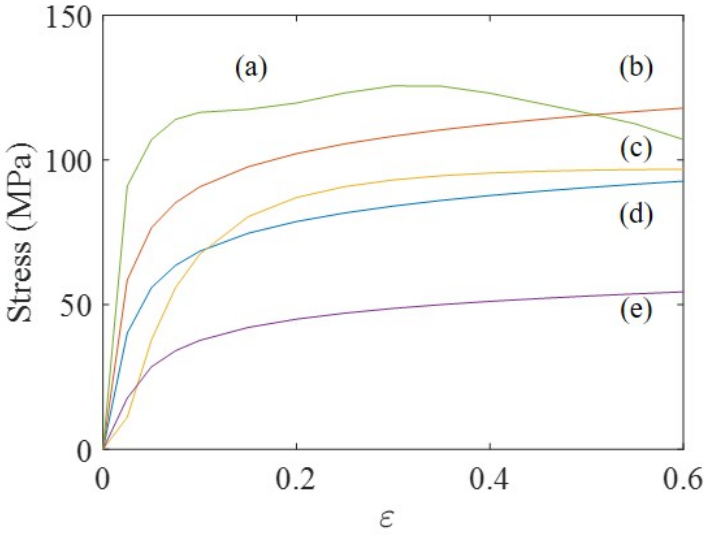

Figure 5.20: Flow stress curves: (a) Compression test (b) Model prediction (c) Paquette et al., 2021 prediction (d) Forge NXT® database (e) Faini, Attanasio, and Ceretti, 2018 prediction

5.3.2 *Constitutive equation for recrystallization analysis of AISI 316*

Constitutive equation, as the one explained in previous section, is typically used to describe the relation of plastic stress with thermodynamic parameters such as strain, temperature and strain rate. However, these equations are usually not able to reproduce material behaviour subjected to recrystallization processes.

Therefore, a recrystallization analysis was carried out for AISI 316 at high temperatures representative of the NSF process and over a wide range of strain rates. These conditions are not widely analysed in the literature although they are of great interest to many mechanical process. The results related to the dilatometer tests were used to carry out the analysis (see Figure 5.9 and Figure 5.10 in Section 5.2.1).

Constitutive equation was modelled according to Sellars and Tegart, 1966 as a hyperbolic sine function. However, to describe this behaviour different equations were used (Equation (4), (5) and (6)) covering all possible regimes of plastic stress, as was explained in Section 2.3.3.

The analysis was made taking logarithms from both sides of Equation (4), (5) and (6). In order to estimate the values of β and b, Equations (7) and (8) were used for plotting $\ln \sigma_p$-$\ln \dot{\varepsilon}$ and σ_p-$\ln \dot{\varepsilon}$. The values of b and β were determined by the average value of the slopes being 6.3272 and 0.0702, respectively (see Figure 5.21). Likewise, $\alpha{=}\beta/b$ was 0.011.

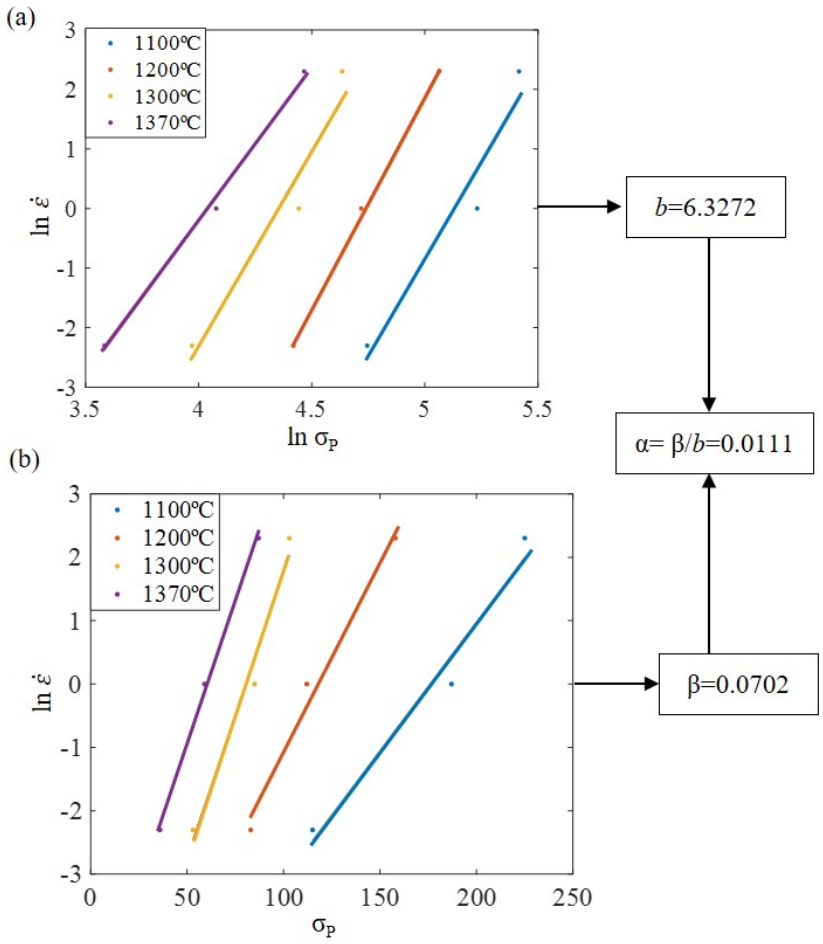

Figure 5.21: (a) $\ln \sigma_p$ vs $\ln \dot{\varepsilon}$ and σ_p vs $\ln \dot{\varepsilon}$ to obtain b and β

To obtain the value of the stress exponent n, Equation (9) was used, plotting $\ln \dot{\varepsilon}$-$\ln[\sinh(\alpha\sigma_p)]$ taking into account the value of α. After linear regression fitting, n was determined to be 4.52 (see Figure 5.22).

Likewise, for each strain rate, the activation energy Q was determined using Equation (9), plotting $\ln[\sinh(\alpha\sigma_p)$-$1/T$. Linear fitting was used to determine the average, obtaining 480 kJ/mol as Q (see Figure 5.23).

Table 5.2 shows a summary of the values calculated.

Table 5.2: A summary of the characteristic constants

b	β	α	n	Q (kJ/mol)
6.3272	0.0702	0.011	4.52	480

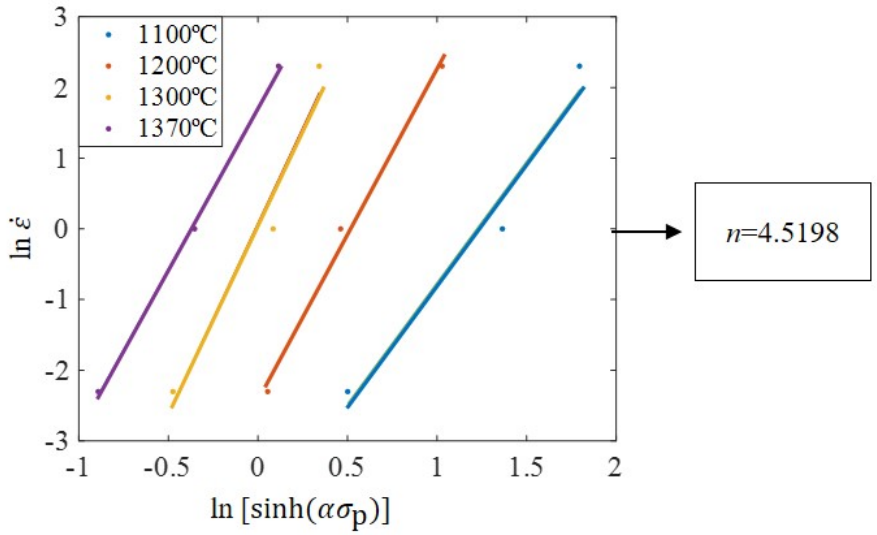

Figure 5.22: $\ln \dot{\varepsilon}$ vs $\ln[\sinh(\alpha\sigma_p)]$ to obtain n

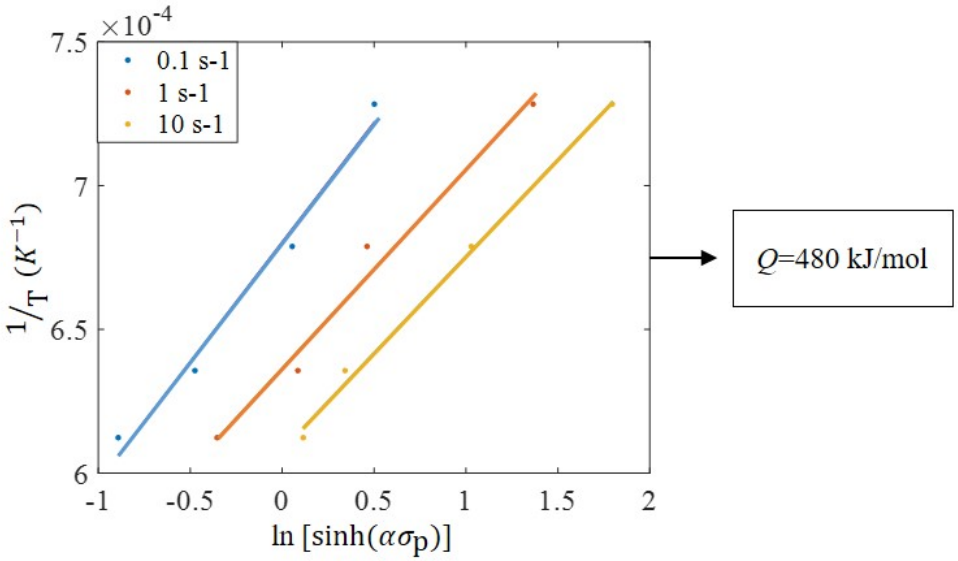

Figure 5.23: $\ln[\sinh(\alpha\sigma_p)$ vs 1/T to obtain Q

5.3.2.1 *Constitutive equation for recrystallization analysis of AISI 316: discussion*

As was mentioned above, the determination of the activation energy for dynamic recrystallization is of wide relevance to be able to model it analytically. This value, although it has been obtained for conditions not reported in literature, is in agreement with different researchers such as Kim, Lee, and Jang, 2003; Liu et al., 2013; Dupin, Yana, and Yanag., 2014 and Suker et al., 2017, being always around 400 kJ/mol.

Nevertheless, it is worth mentioning that the obtained value was slightly higher than those reported in the literature, around 20% higher. According to Nkhoma, Siyasiya, and Stumpf, 2014 the hot working conditions should not have an effect on activation energy. Therefore, the observed differences may be explained by alloying elements and possible formation of new phases during heating and deformation. For instance, Bao et al., 2011 stated that higher amount of alloying elements would result in higher activation energies. In this line, McQueen et al., 1995 demonstrated that stainless steels with high amount of delta ferrite, tended to have higher activation energies, that is, delta ferrite hampers dynamic recrystallization to take place. On this basis, the obtained result is in concordance with all the statements found in the literature as was demonstrated that, due to the preheating at 1370°C, high amount of delta ferrite would be expected specially under the most extreme conditions.

With regard to α, β and n, these values are reported in literature to be apparent material parameters (Mirzadeh et al., 2011; Mirzadeh, Cabrera, and Najafizadeh, 2011). Therefore, no special variation in comparison to the values shown in the literature would be expected. For instance, these values are in agreement with those obtained for similar steel grades but under different conditions (Nkhoma, Siyasiya, and Stumpf, 2014; Wang et al., 2016a).

It should be mentioned that, although the values were obtained as an average to cover the whole range of conditions, a slight change in trend was observed between 1200 and 1300°C in the graph related to b, n and β (see Figure 5.21 and Figure 5.22). This change is in agreement with the alterations in microstructure reported in Section 5.2.1, proving that the presence of delta ferrite influences not only the flow behaviour but also the recrystallization behaviour.

5.4 DETERMINATION OF THE CRITICAL STRAIN AND STRESS

Based on the flow stress curves showed in Section 5.2.1, it is possible to analytically determine whether recrystallization has taken place during the deformation process or not. The flow curves shown in Figure 5.11 had a peak value which is supposed to be a sign of dynamic recrystallization. In order to determine the presence of recrystallization, the method proposed by Poliak and Jonas (Poliak and Jonas, 2003a; Poliak and Jonas, 2003b), which assumed that the initiation of recrystallization takes place when an inflection point is observed in the work hardening, was used.

5.4.1 *Determination of the critical strain and stress: results*

The stress-strain curves were fitted to a seventh order polynomial. It was observed that this order was accurate enough to fit the stress-strain with no remarkable deviations (the coefficient of determination was always higher than 0.998). This approach made

the future differentiation needed easier than employing a ninth order polynomial, as is usually reported in the literature.

Then, this function was differentiated to obtain the work hardening rate ($\theta = \frac{d\sigma}{d\varepsilon}$), which was plotted against flow stress. This function was, then, differentiated twice and equalled to zero to determine the aforementioned inflection point. Figure 5.24 shows two dissimilar curves under the same conditions but different heating profiles.

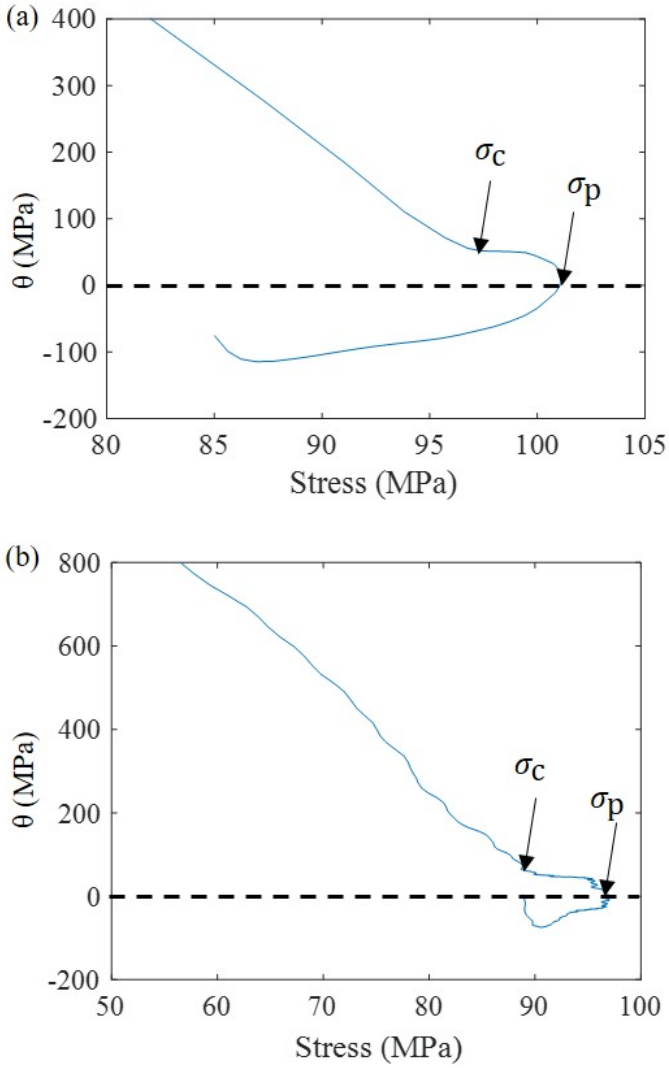

Figure 5.24: Work hardening curve showing the presence of DRX at 1300°C: (a) Dilatometer (b) Gleeble (commercial trials)

Afterwards, the critical strain was determined for each condition. In Figure 5.25 the critical strains versus the Zener-Hollomon parameter are shown. As has been previously mentioned, Z can be calculated following Equation (3), as a function of absolute tem-

perature and strain rate. In this case, as the strain rate was kept constant, a decreasing trend in Z, is the result of increasing the temperature.

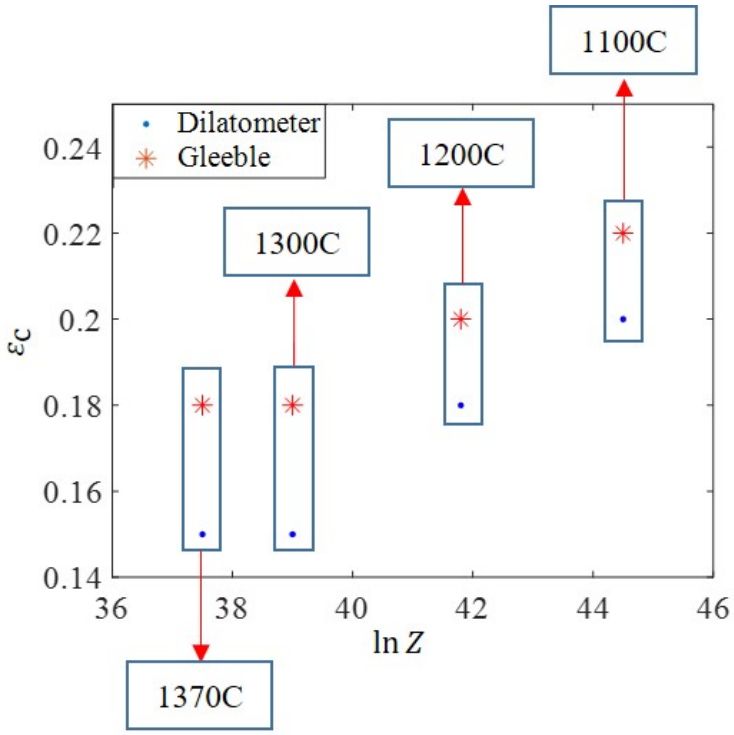

Figure 5.25: Critical strain as a function of Z for the two different configurations and, therefore, heating rates

Carrying out a similar analysis with the critical stresses, the obtained results at a strain rate of 10 s^{-1} with the different heating rates are shown in Figure 5.26.

The tests carried out in the dilatometer also permitted the analysis of the effect of strain rate on the critical onset for DRX at temperatures close to the solidus and notably higher than those reported in the literature. These results are summarized in Figure 5.27.

In this case, a clearly increasing trend was observed with the strain rate, especially at low strain rates. As DRX is not an instantaneous phenomenon, it needs time to occur. That is why, for higher strain rates the obtained critical strains also became higher. Something similar was reported by Ghazani and Eghbali, 2018. Analysing the critical stresses, an increasing trend was observed due to the strain rate hardening effect.

5.4.2 *Determination of the critical strain and stress: discussion*

As can be seen, for the dilatometer case at 10 s^{-1}, the critical strain varied between 0.22 and 0.15 with a notable drop at the highest temperature while for the Gleeble case, it varied between 0.22 and 0.18. In general, for both cases, the critical strain tended

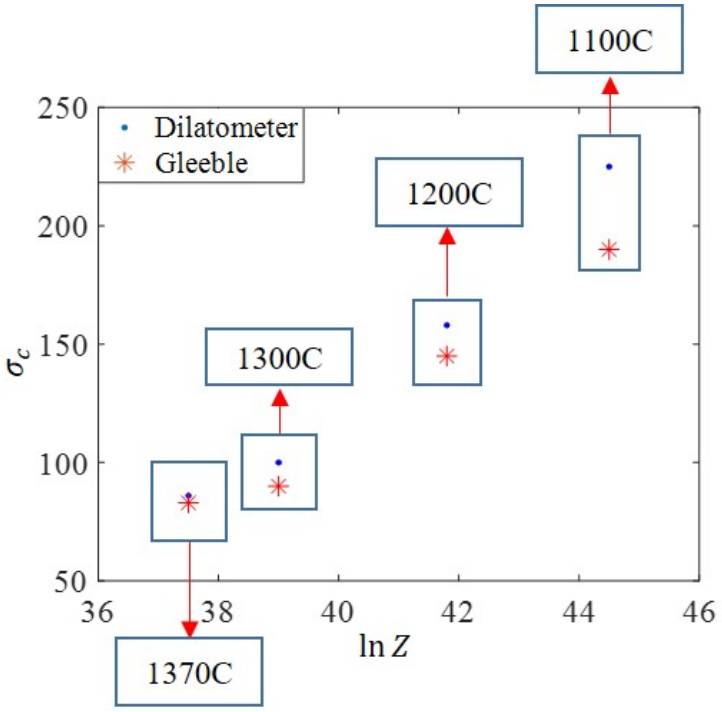

Figure 5.26: Critical stress as a function of Z for the two different configurations and, therefore, heating rates

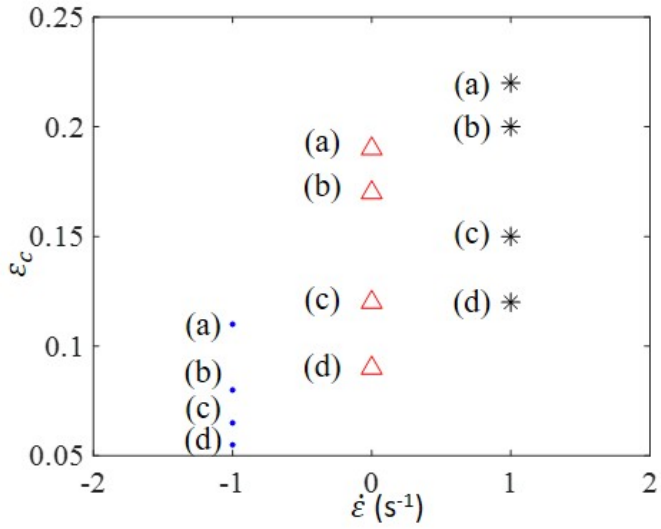

Figure 5.27: Critical strain as a function of strain rate for the dilatometer tests: (a) 1100°C (b) 1200°C (c) 1300°C (d) 1370°C

to decrease with temperature. The slight variations observed, although they could be considered negligible, are assumed to be due to the differences in the heating rate. These results are in agreement with those reported by Taylor and Hodgson, 2011.

Therefore, it can be stated that, according to the analytical calculation, DRX is expected to occur under these conditions. As can be observed, in contrast to what happened with the critical strain, temperature plays a relevant role in the critical stress. In general, a clearly decreasing trend was observed with the increase in temperature, which is attributed to the thermal softening effect. In addition, slight differences were observed due to the heating rate, being lower than the values obtained with the Gleeble. This, as has been discussed in Section 5.2.1, could be assumed to be due to the higher grain sizes (see Figure 5.11).

It is worth mentioning that critical strain and stress are relevant parameters for predicting the initiation of DRX. In general, in the cases in which a clear peak value is observed, a relation could be established between critical and peak values giving a general overview about DRX mechanisms. On this basis, for the conditions shown in Figure 5.11, the ratios between critical and peak values were determined. The results are shown in Figure 5.28.

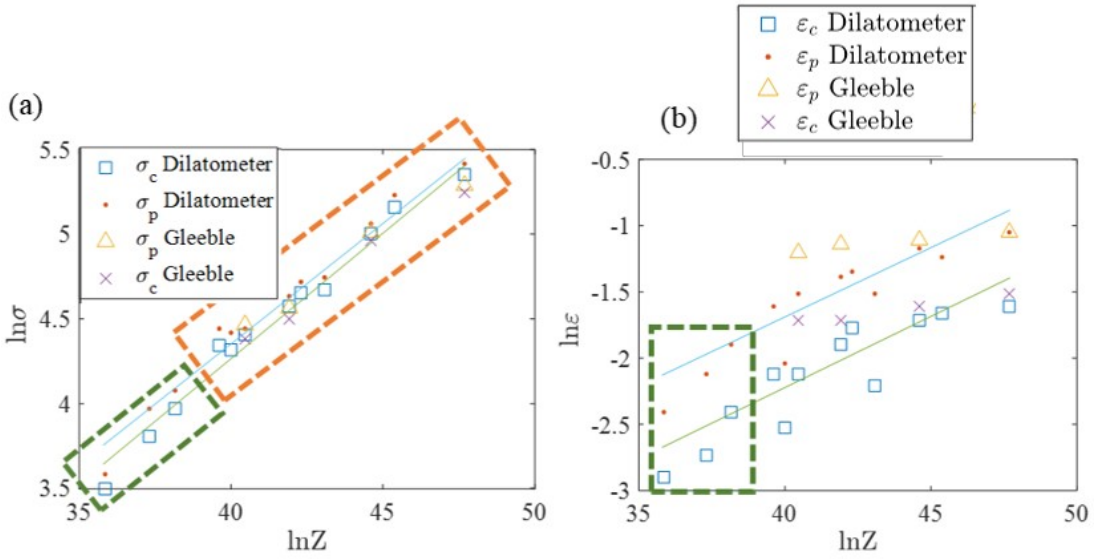

Figure 5.28: Ratio between critical and peak: (a) Stresses (b) Strains for the dilatometer and Gleeble tests

As can be seen, regardless of the conditions (strain rate and temperature) or the heating rate and the test configuration, the values of the ratios remained constant, being 0.6 for the strains and 0.9 for the stresses. These results are in agreement with those reported by Cho and Yoo, 2001a and Nkhoma, Siyasiya, and Stumpf, 2014, among others.

In addition, it is worth mentioning that, although all the experimental conditions were fitted to a linear function, a change in the trend can be observed at lower values

of $\ln(Z)$ which corresponds to higher temperatures. Therefore, it can be stated that under NSF conditions, the recrystallization behaviour may change mainly due to the formation of delta ferrite during the heating which then it is not dissolved at the testing temperature. This change in trend is highlighted in Figure 5.28.

5.5 CONCLUSIONS

Summarizing, the following conclusions can be stated:

- The DSC analysis carried out allows the solidus temperature of the sample to be determined. This temperature was set to 1435°C which is in accordance with the literature. Therefore, this DSC analysis established the process temperature as 1370°C as was stated in previous research that NSF works at temperatures close to the solidus (between 0.9 and 0.95 times the solidus temperature as stated by Lozares et al., 2020).
- DSC results were compared with those obtained through simulations with FactSage®, the simulations being in agreement with the experimental results for the solidus temperature.
- AISI 316 flow behaviour was characterized under extreme conditions representative of the NSF process. In general, a clear thermal softening and strain rate hardening were observed in the range of temperatures analysed, showing the expected trend found in the literature but with changes when moving up to temperatures representative of the NSF process.
- The influence of the heating rate was also studied. Using the slowest heating rate slightly higher grain sizes were observed, which could explain the slight softening. Delta ferrite formation was seen on the austenite grain boundaries with the lowest heating rate, which could also have an effect on the softening.
- It was proven that the flow stress parameters found in the literature or proposed by the Forge NXT® software were not able to accurately reproduce material behaviour under close to NSF conditions. On this basis, an optimization algorithm was carried out in order to determine material constants representative of these conditions. Thanks to this optimization, the prediction was reduced by more than half although characterization of the recrystallization behaviour was still necessary to properly reproduce material behaviour.
- Constitutive equation parameters were determined for AISI 316 under extreme conditions to model the recrystallization behaviour. The obtained values were in the range previously reported in the literature. Nevertheless, it should be highlighted that the conditions tested are far from those studied in the literature and the slight

discrepancies found between the obtained parameters and the typical ones showed in the literature were proven to be due to the formation of delta ferrite under these conditions which hamper recrystallization to occur.

- Among all the constitutive parameters, activation energy defines the difficulty for DRX to take place. The obtained value was 480 kJ/mol, being around 20% higher than the ones reported in the literature under totally different conditions, making it more difficult recrystallization to occur. This higher activation energy is assumed to be due to the amount of delta ferrite formed due to the slow heating rate used and the high temperature reached. These conditions are not tested in the literature.

- The onset for DRX initiation was analytically determined to be around 0.2 under all the conditions tested. In general, critical strain tended to decrease with temperature but to increase with strain rate. For low values of $\ln(Z)$, that covers the conditions representative of the NSF process, a change in trend was observed proving that extrapolation to NSF conditions may fail due to the effect of delta ferrite formation.

- The range of conditions tested included extreme conditions representative of the NSF process and not studied in the literature. The critical to peak strain and stress ratios were calculated to be 0.6 and 0.9, respectively. These results are in the same order of magnitude than those reported in the literature for different conditions.

Therefore, the comprehensive analysis carried out during this chapter about the thermomechanical behaviour of AISI 316 demonstrated that there is, in general, a change in the trends when moving from 1200°C (the maximum temperature commonly tested in the literature) to more than 1300°C (temperatures representative of the NSF process) which makes it necessary to characterize the material under these conditions as extrapolation based on the experimental data available may tend to fail. This change on the behaviour was attributed to the formation of relatively a high amount of delta ferrite which is not diluted after the cooling. It was proven the presence of delta ferrite corroborating this assumption.

6 RECRYSTALLIZATION ANALYSIS

Different restoration mechanisms take place during the forming process. To identify these mechanisms the flow stress curves were used and they were validated using microstructural analysis. The objective of this study is to evaluate the hot working characteristics of AISI 316 and to show whether recrystallization could occur within the NSF working range.

Among all the possible mechanisms, recrystallization implies small grain sizes which could be beneficial for the final part. Dynamic recrystallization is the most common under the conditions reached in the process as it occurs at high strains and temperatures. Nevertheless, postdynamic recrystallization could occur if the restoration process does not finish and the final strain is higher than the critical one. Finally, if the strains were not high enough, static recrystallization could occur. However, as the strains reached during the process are high (in many cases higher than 1), static recrystallization was not considered in the analysis.

The knowledge of the initial microstructure is essential to understand the behaviour of an alloy subjected to a deformation process. In general, NSF is usually carried out at temperatures near the solidus. This is based on the assumption that higher grain sizes could be beneficial as softer alloys would be expected.

Dupin, Yana, and Yanag., 2014 noticed an increment in the recrystallization rate with temperature, and a decrease when the strain rate increases. This was also observed by Radionova et al., 2022. From medium to high strain rates, the DRX rate has a constant value, while for lower strain rates it increases with temperature. They also observed that the critical strain tended to decrease with an increase in temperature having the opposite trend with the strain rate (see Figure 6.1).

Furthermore, Dehghan-Manshadi, Barnett, and Hodgson, 2008b studied dynamic recrystallization using AISI 304. As mentioned above, the typical DRX flow curves has a single peak stress followed by a steady state stress. Figure 6.2 shows that samples deformed under high values of Zener-Hollomon parameter (Z) have microstructures finer than with low values of Z. Moreover, they observed the beginning of DRX due to the typical necklace structure as Figure 6.3 shows.

Metallurgy is a tough way to determine DRX initiation. Based on EBSD data KAM parameter which is the Kernel Average Misorientation would be a good choice (Xu et al., 2022). This parameter is established in the literature as a possible method to determine whether the grain is recrystallized or deformed. It is known that recrystallized grains have lower KAM values whereas higher KAM values are related to high density levels of dislocation in the microstructure (Zohrevand et al., 2021).

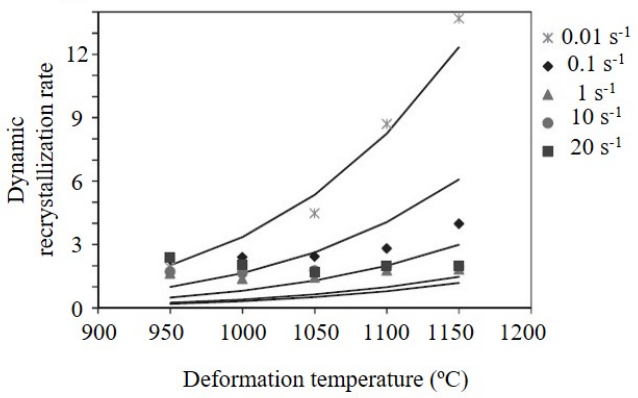

Figure 6.1: Dynamic recrystallization rate at different strain rates (Adapted from Dupin, Yana, and Yanag., 2014)

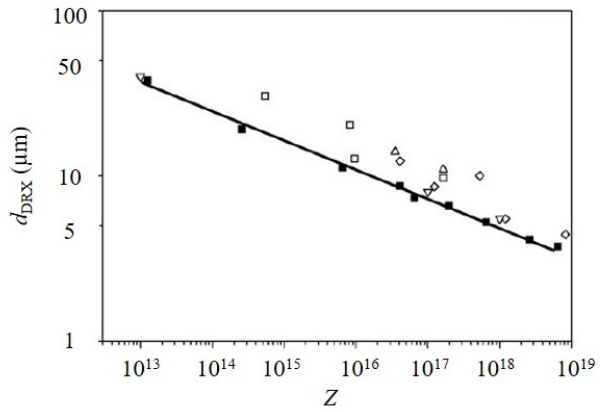

Figure 6.2: DRX grain size vs Z (Adapted from Dehghan-Manshadi, Barnett, and Hodgson, 2008b)

Kumar et al., 2016 analysed DRX in an austenitic stainless steel 316L under dissimilar hot working conditions. These researchers established that the grains were recrystallized when the KAM parameter was lower whereas higher values were related to pancaked grains (see Figure 6.4).

However, the use of EBSD analysis to determine DRX usually requires the quenching of the sample. This could induce some phase transformations or changes in the physical properties (Liss et al., 2009). In addition, this method is expensive and very time con-

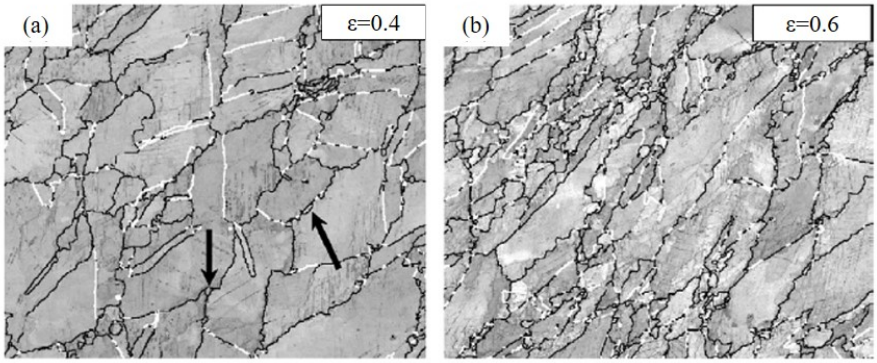

Figure 6.3: AISI 304 deformed at 900°C and 0.01 s^{-1} (Adapted from Dehghan-Manshadi, Barnett, and Hodgson, 2008b)

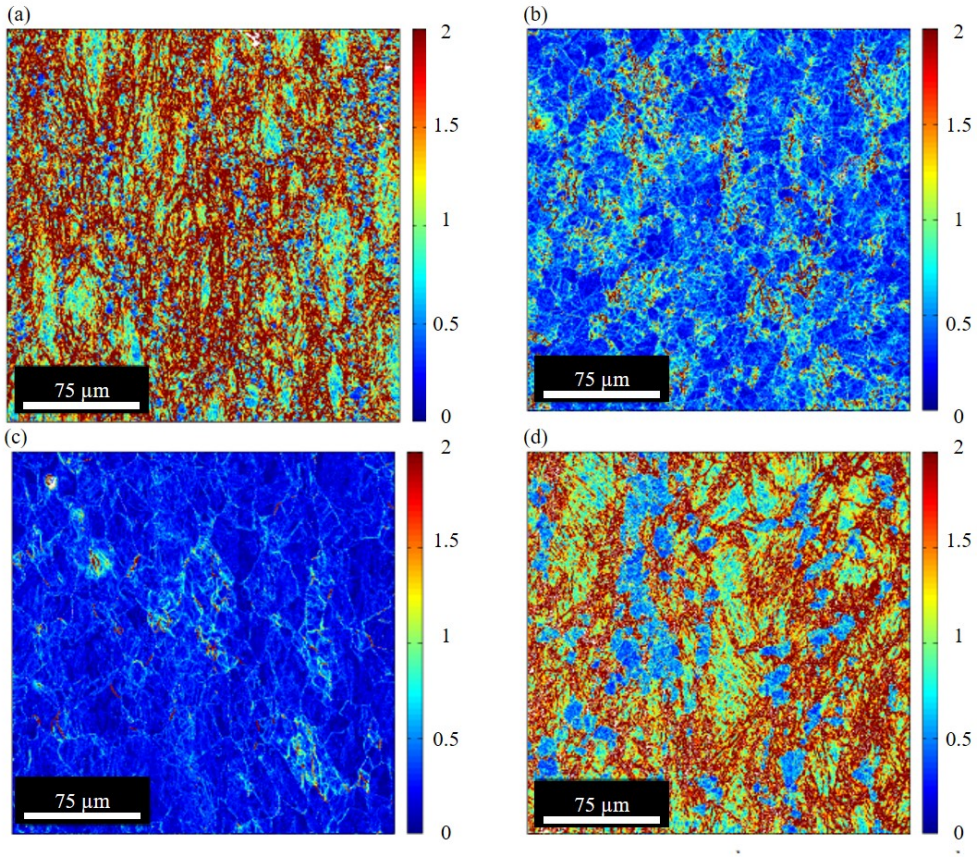

Figure 6.4: KAM images of AISI 316 at (a) 950°C and 0.1 s^{-1} (b) 1050°C and 0.1 s^{-1} (c) 1150°C and 0.1 s^{-1} (d) 950°C and 10 s^{-1} (Adapted from Kumar et al., 2016)

suming. That is why, it would be of great interest to have another experimental method overcoming these limitations.

Also, metadynamic recrystallization is a process whose main characteristic is the continued growth of nuclei formed due to DRX during prestraining Cho and Yoo, 2001b. These researchers investigated MDRX using AISI 304 and they found that after 50% softening there is no difference in the time. To predict the recrystallized volume fraction, they used the Avrami equation with the value of 1.06 for the Avrami constant. Equation 30 determines the time for 50% softening.

$$t_{50} = 1.33 \times 10^{-11} \dot{\varepsilon}^{-0.41} D \exp((230300\text{J/mol})/RT) \tag{30}$$

In Chapter 5 it was established the relevance of having a proper knowledge of the conditions needed to determine the onset for DRX initiation. Together with this, a summary of different equations to model DRX grain sizes were also given. Table 6.1 summarizes different equations found in the literature for DRX grain sizes determination showing no agreement between researchers with regard to grain sizes prediction. This can be more clearly seem in Figure 6.5, especially at lower values of Z which are related to high temperatures. As the majority of the laws were obtained at temperatures up to 1200°C, they need to extrapolate to go to NSF conditions and it is in this range were more discrepancies were found between researchers proving the necessity of characterizing, not only analytically but also through microstructural analysis, the possible occurrence of DRX under these extreme conditions.

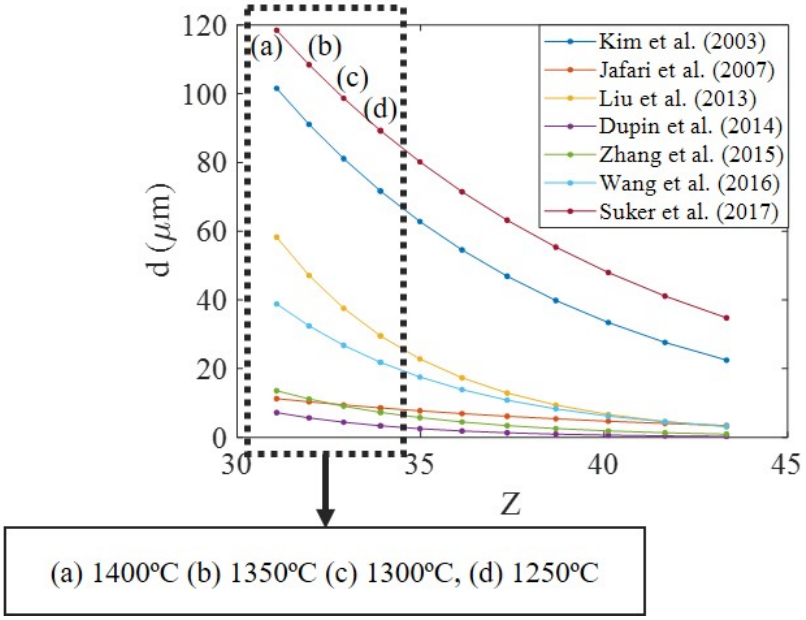

Figure 6.5: Grain sizes extrapolation using different laws from literature

Table 6.1: Summary of the main conditions employed with DRX grain sizes equations for AISI 316

Ref.	T (°C)	$\dot{\varepsilon}$ (s^{-1})	Grain sizes (μm)
Kim, Lee, and Jang, 2003	$1000-1200$	$0.05-5$	$4644Z^{-0.123}$
Liu, Li, and Dang, 2013	$900-1200$	$0.001-10$	$1.01e5Z^{-0.24}$
Dupin, Yana, and Yanag., 2014	$950-1150$	$0.01-20$	$2.7e4\varepsilon^{-0.2}\exp\left(\frac{-1.3e4}{T}\right)$
Jafari, Najafizadeh, and Rasti, 2007	$950-1100$	$0.01-1$	$230Z^{-0.097}$
Zhang et al., 2015	$900-1200$	$0.1-10$	$1.3e4Z^{-0.22}$
Wang et al., 2016b	$900-1250$	$0.01-1$	$20975.5Z^{-0.19}$

Therefore, recrystallization is the only way to achieve free strain microstructures and to obtain stainless steel parts with good mechanical properties and small grain sizes. However, the majority of the studies found in the literature only reached up to 1200°C and no agreement was found between researchers as can be seen in Table 6.1. Thus, this chapter covers a comprehensive microstructural analysis of AISI 316 to study the possible occurrence of different restoration mechanisms under close to NSF conditions.

6.1 GRAIN GROWTH

Together with the DSC analysis carried out and explained in Section 5.1, grain growth kinetics were studied to define the initial grain sizes at each temperature from the typical range found in the literature to the NSF temperatures.

The initial microstructure of the sample is another relevant aspect to be considered as it could play a role in material properties, thus affecting process performance. Also, it could have an effect on recrystallization behaviour as grain boundaries may act as nucleation locations. Therefore, it would be expected that higher grain sizes would result in a small amount of grain boundaries delaying the onset of recrystallization. However, in spite of this relevance few research works were found aiming to address this issue.

6.1.1 *Grain growth: results*

On this basis, grain sizes were measured according to the procedure mentioned above (see Section 4.1.2). The results can be observed in Figure 6.6.

The variation of the grain sizes with temperature and time was analysed covering a wide range of temperatures from the typical ones of forging to those representative of the NSF process. It was observed that, for both time periods, after exceeding a temperature of 1300°C, the grain started to decrease which could be beneficial for the NSF process. This trend is assumed to be due to delta ferrite formation.

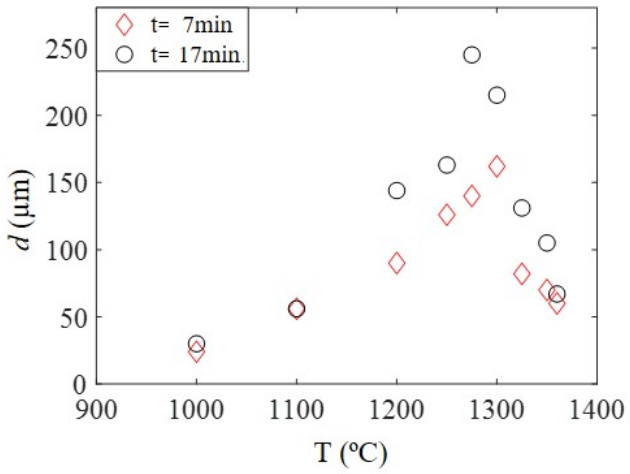

Figure 6.6: Grain growth kinetics for AISI 316

6.1.2 *Grain growth: discussion*

In Chapter 5 it was found that, under equilibrium conditions (that is based on DSC analysis), delta ferrite tended to appear at very high temperatures. However, as stated by Venugopal, Mannan, and Prasad, 1996 or Soleymani, Ojo, and Richards, 2015, this phase could nucleate easier under non-equilibrium conditions. The microstructure of the deformed samples was analysed in Section 5.2.1 but it would be of great interest to know the possible presence of delta ferrite in the microstructure prior to deformation as can be observed in Figure 6.6 a drastic change in the trend which can not be explained as simply a consequence of the heating. Therefore, the microstructures of the quenched specimens can be seen in Figure 6.7.

Based on Figure 6.7, it can be seen that, after seven minutes of holding time, the amount of delta ferrite became more prominent at 1300°C although some delta ferrite appeared at 1275°C. For 17 minutes, as there was much more time to nucleate, the amount of delta ferrite became relevant around 1275°C. At NSF temperatures, the difference in delta ferrite can be seen in Figure 6.8. It is worth mentioning that the length of the scale bar is different.

Microhardness could help to prove the formation of a higher amount of delta ferrite as harder structures would be expected (Ghasemi, Beidokhti, and Fazel-Najafabadi, 2018). In addition, the microhardness is assumed to increase with the holding time as a greater amount of delta ferrite would be created (Ayers, 2012; Setyowati, Widodo, Hermanto, et al., 2019). Microhardness measurements of the samples under all the conditions tested can be seen in Figure 6.9-b.

As can be seen, a decreasing trend was obtained for both holding times up to a temperature of around 1250°C. This trend is in agreement with what could be expected

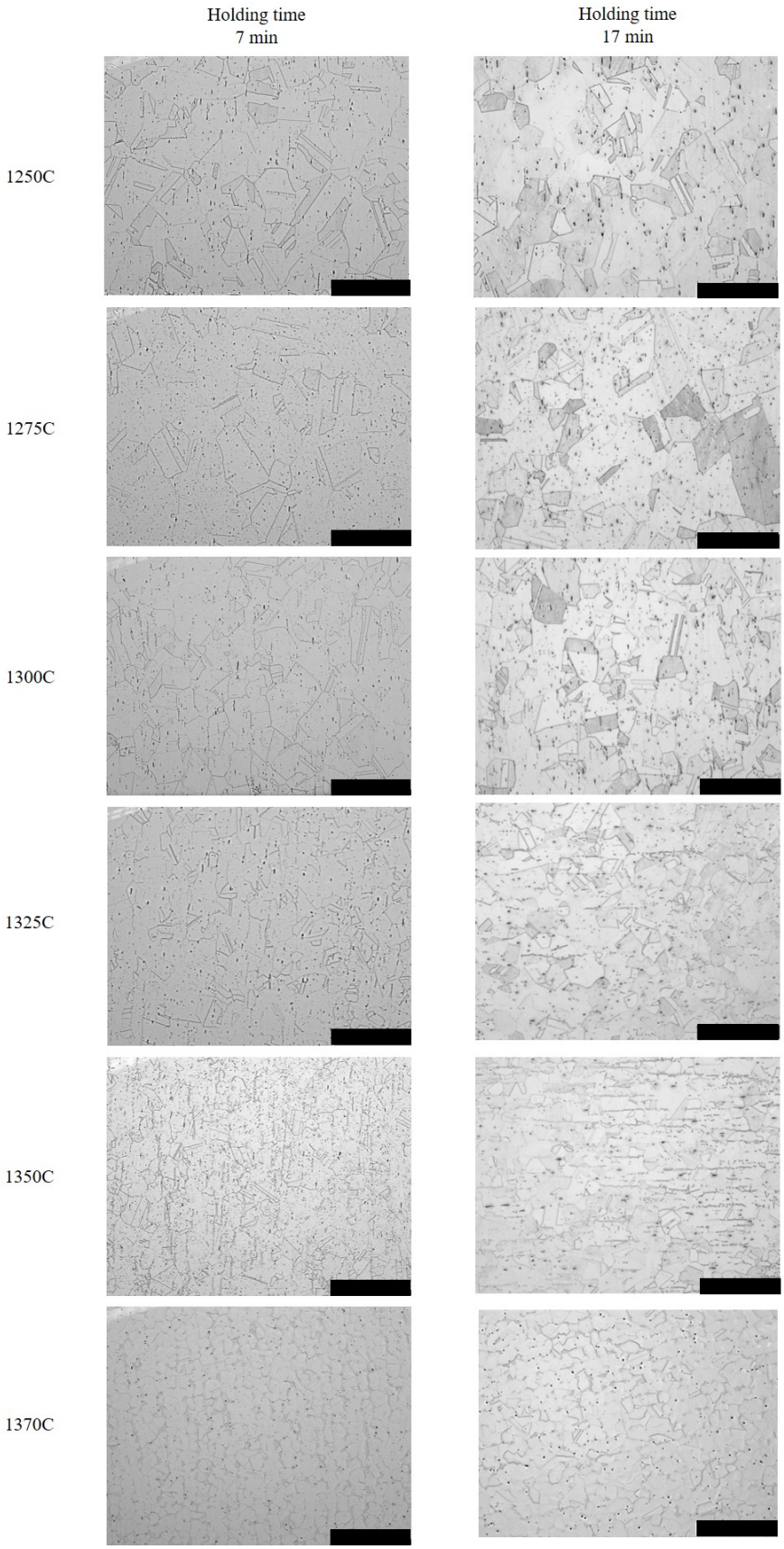

Figure 6.7: Optical microstructures from 1250°C to 1370°C at two dissimilar holding times. Scale bar: 500 µm

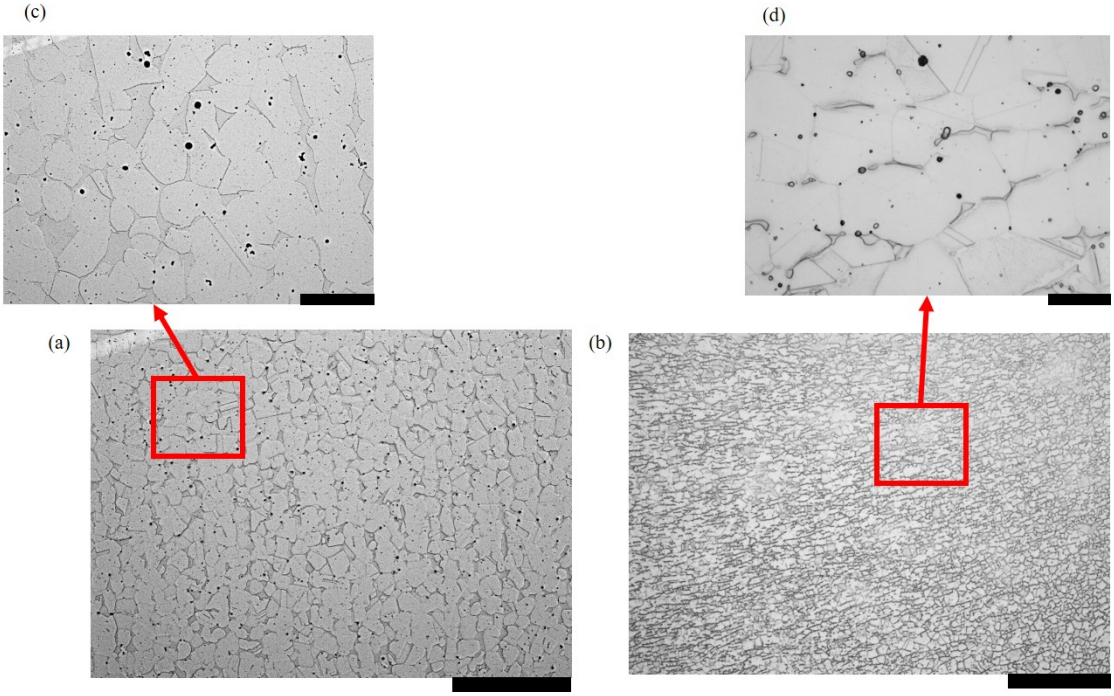

Figure 6.8: (a) 7 min (b) 17 min of holding time. Scale bar: (a) 500µm (b) 500µm (c) 100µm (d) 20µm

based on grain size measurements. Over this temperature, a notable increase was observed in the microhardness which can be correlated with the higher amount of delta ferrite observed in the microstructure.

Delta ferrite not only influences the material properties (as was observed based on microhardness measurements), but it also affects the grain growth kinetics. Grain size is expected to increase with temperature and time following an Arrhenius type equation as stated by different researchers (Huang et al., 2019; Stornelli et al., 2022). Nevertheless, as can be seen in Figure 6.9-a, grain growth velocity tended to increase with temperature again up to around 1250°C. Moreover, it decreased with the holding time, in agreement with what would be expected based on Arrhenius equation. In contrast, over this temperature, grain growth velocity drastically decreased. This is assumed to be due to delta ferrite formation. At higher temperatures and higher holding times, delta ferrite nucleates easier and tends to precipitate to grain boundaries eliminating or, at least, reducing the facility for the grains to grow. This effect is known as Zener pinning and it was stated by different researchers that the higher the amount of delta ferrite, the lower the grain sizes would be (Zhang, Terasaki, and Komizo, 2011; Fu et al., 2020). This statement is in agreement with the experimental measurements shown in Figure 6.9.

Therefore, it can be concluded that the heating of the sample before the NSF process could play a relevant role. Although higher grain sizes would be expected at these extreme

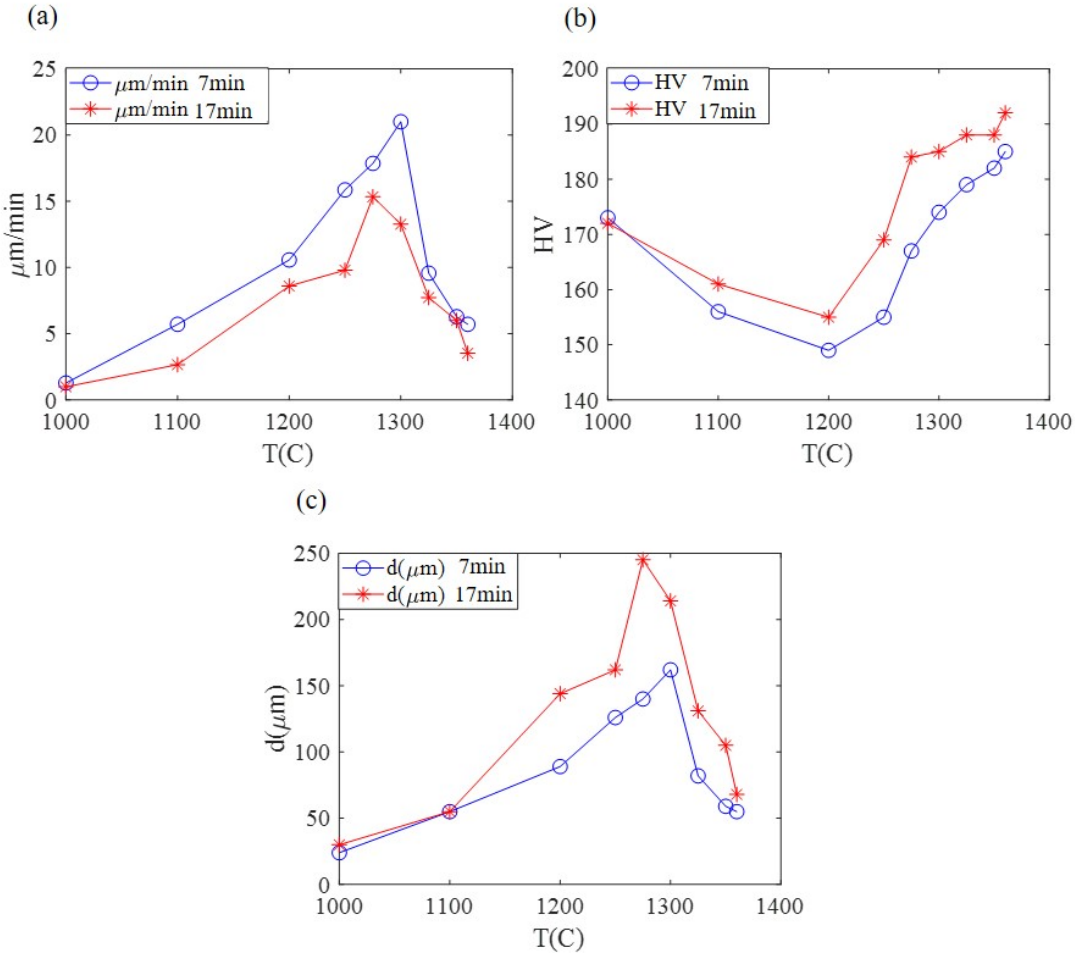

Figure 6.9: (a) Grain growth velocity (b) Microhardness (c) Grain sizes

temperatures, it was observed that over a temperature close to 1250°C, the grain sizes decreased and the microhardness increased up to values quite close to those of the as-received material. In addition, the formation of delta ferrite may be detrimental for the material properties expected in the final part.

6.2 MICROSTRUCTURAL VALIDATION OF THE CRITICAL STRAIN

Once the existence of recrystallization has been analytically proven in Chapter 5, a microstructural analysis was carried out to verify the occurrence of recrystallization and to determine the grain size after deformation.

6.2.1 *Microstructural validation of the critical strain: results*

With this aim, plane strain compression tests were carried out as they are supposed to generate more uniform strain profiles throughout the sample as was stated in Chapter 2. The tests were stopped at two different strains one below the critical one (0.12) and the other one higher than it (0.4). The temperatures tested were 1200°C, 1250°C, 1275°C, 1300°C, 1330°C and 1370°C at a strain rate of 10 s^{-1}, following the commercial heating profile (see Figure 5.8).

The microstructures obtained are shown in Figure 6.10. Based on previous results, a non-recrystallized microstructure would be expected for the samples subjected to 0.12 of strain, while for the samples at 0.4, initial coarse grains were supposed to be replaced by equiaxed grains, meaning that DRX occurred. This does not necessarily mean that recrystallization had finished as new grains could still nucleate due to a phenomenon called metadynamic recrystallization.

It is worth mentioning that these validation tests were carried out following the commercial heating profile. Nevertheless, based on the results presented in the previous section, recrystallized microstructures would be expected regardless of the heating profile. With this aim, dissimilar tests were done at 1 of strain (to ensure that the critical strain is exceeded) using the Gleeble and the dilatometer as mentioned in Section 5.2.1. For the Gleeble case, the heating profile was the non-commercial one, as is explained in Section 4.1.3.1. Figure 6.11 shows the EBSD microstructures obtained after deforming the sample up to a strain of 1 and at a strain rate of 10 s^{-1}.

The aim of Figure 6.11 is to show the possible influence of the heating profile on DRX. As can be seen, as the strain was high enough to exceed the critical strain, the majority of the samples showed a fully recrystallized microstructure. At 1100°C, under both conditions, Figure 6.11 shows a partially recrystallized microstructure. This result is in agreement with the analytical calculation of the critical strain which reported that recrystallization was more difficult when the temperature decreases.

6.2.2 *Microstructural validation of the critical strain: discussion*

As can be seen in Figure 6.10, all the hypotheses mentioned above were corroborated. In general, deformed and coarse grain sizes were observed under all the conditions developed at 0.12, being the grain sizes higher than those obtained at 0.4. In addition, together with having smaller grain sizes at 0.4, an equiaxed microstructure was observed.

Therefore, the presence of dynamic recrystallization has been proven. However, once the deformation had stopped, due to the high strain and temperatures, metallurgical issues could still play a relevant role. Among all the possibilities, the most likely one would be metadynamic (post-dynamic) recrystallization. The aim of this section is to analyse the possible existence of this phenomenon.

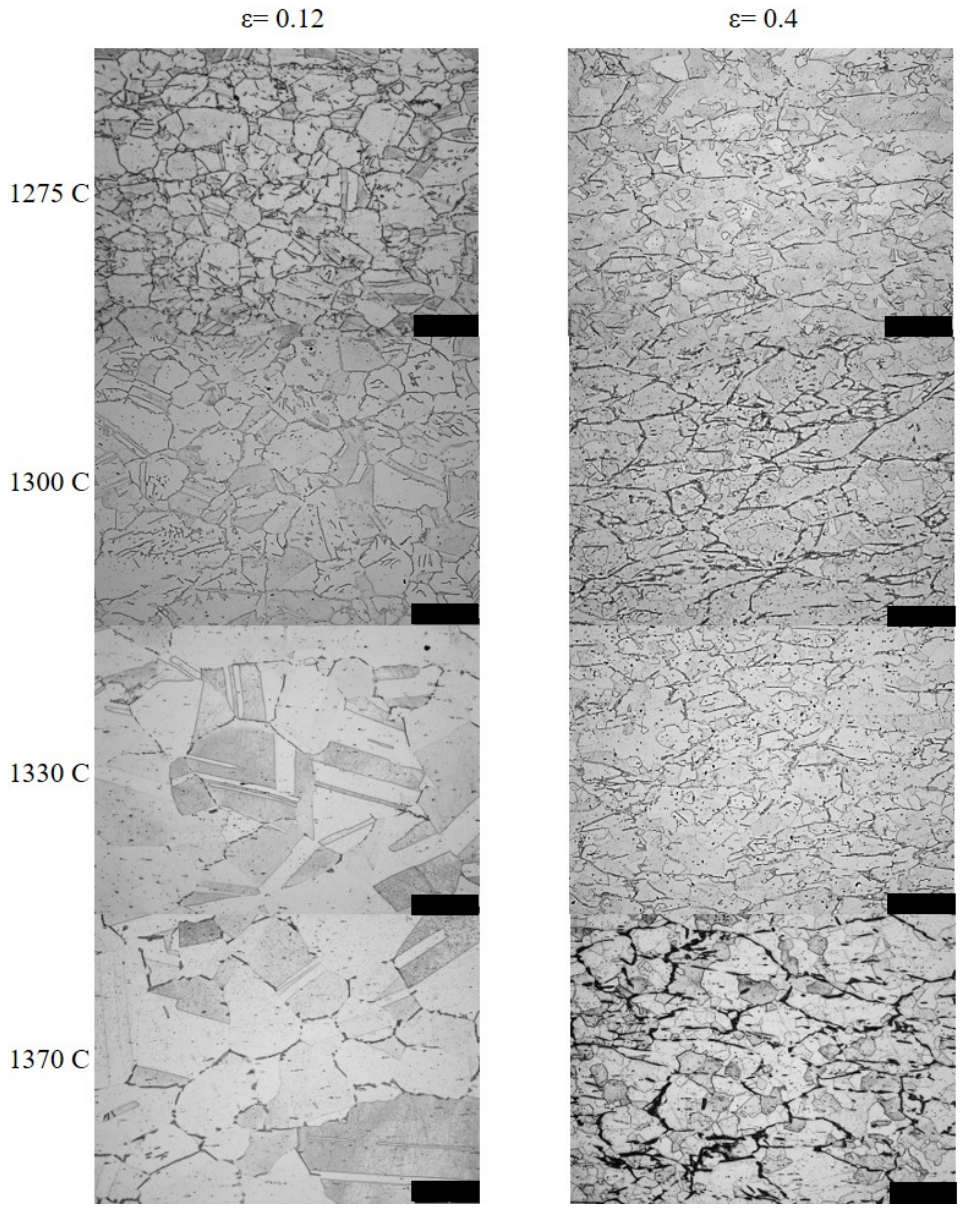

Figure 6.10: Microstructures at 0.12 and 0.4 of strain from 1275°C to 1370°C. Scale bar: 200 µm

To achieve this aim, different experimental tests were carried out under dissimilar conditions to be compared with previous results. After the deformation, the sample was kept at the testing temperature during a certain holding time to study the microstructural evolution.

The holding time was calculated to obtain a 50% volume fraction of recrystallized grains, this is called t_{50}. At low strains, authors such as Dehghan-Manshadi, Barnett,

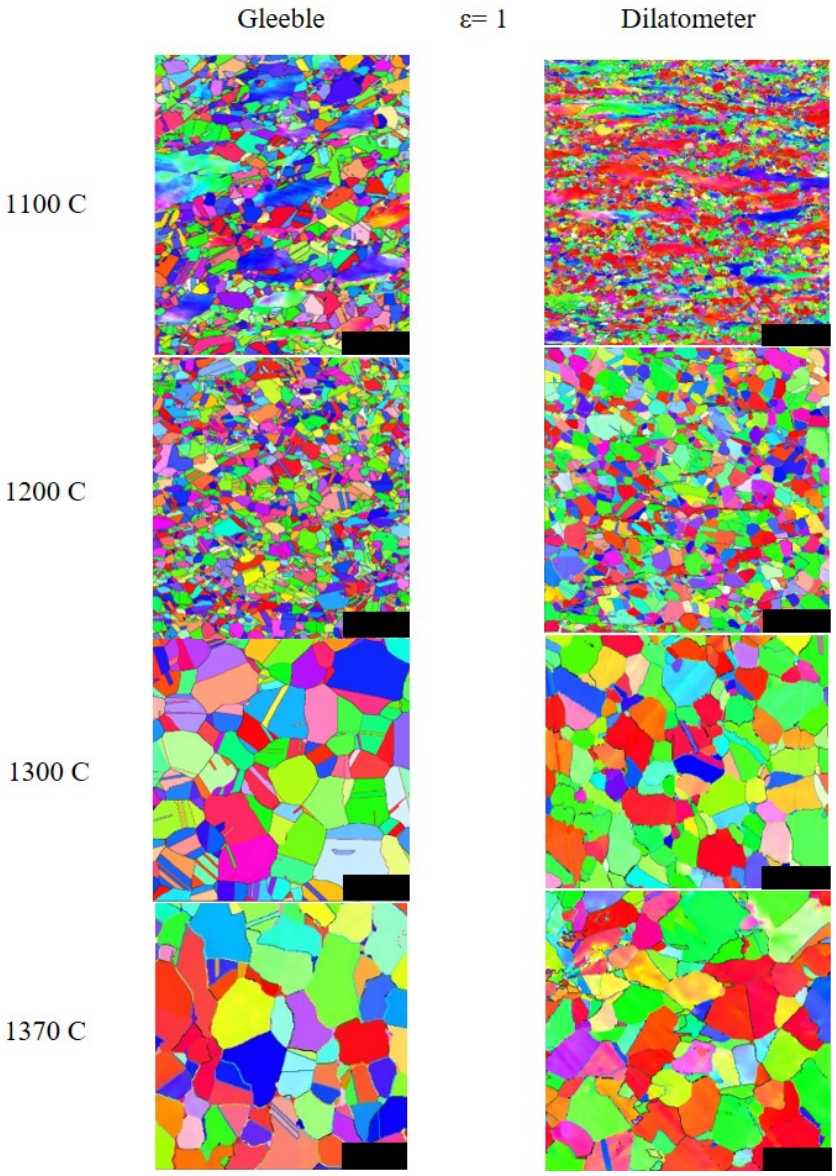

Figure 6.11: EBSD microstructures at 1 of strain from 1100°C to 1370°C. Scale bar: 50 µm

and Hodgson, 2008b proved that these parameters could be modelled as a function of strain, temperature and strain rate according to Equation (31).

$$t_{50} = 8 \cdot 10^{-9} \varepsilon^{-1.48} Z^{-0.42} \exp\left(\frac{375000}{RT}\right) \tag{31}$$

Using Equation (31), for the different condition tested, the following holding times were obtained (see Table 6.2).

Table 6.2: Holding times calculated for each temperature from 1200°C to 1370°C

T (°C)	1200	1250	1275	1300	1330	1370
t (s)	110	70	57	46	33	26

As can be seen in Table 6.2, the holding time decreases when temperature increases. At high temperatures, MDRX is more prone to occur as these events are governed by the energy stored in the dislocations. Nevertheless, it is worth mentioning that, according to the literature review (Dehghan-Manshadi, Barnett, and Hodgson, 2008b; Lin et al., 2016), this phenomenon is assumed to be more affected by strain rate. That is why, among all the strain rates tested, the highest one was chosen as it is representative of the industrial process.

The conditions tested were 1200°C, 1250°C, 1275°C, 1300°C, 1330°C and 1370°C at 10 s^{-1}. The heating profile chosen was the commercial one to be as close as possible to the conditions reached during the NSF process. The tests were stopped at a strain of 0.4.

Therefore, following this experimental procedure, the tests were carried out and the microstructures after deformation were analysed and compared with the previous ones without the holding time. The results can be seen in Figure 6.12.

In general, no clear differences were observed between the microstructures with and without the holding time. At temperatures higher than 1300°C, it seems that the grains could be smaller in the metadynamic cases. This is due to the fact that at these temperatures delta ferrite enters a stable phase and, because of the holding time and its formation during the heating and due to the deformation, it has enough time to precipitate to the austenite grain boundaries, inhibiting the grain growth.

As these are the most interesting conditions with regard to the industrial process, EBSD analyses were carried out to have higher accuracy and resolution to do the comparison. The results are shown in Figure 6.13.

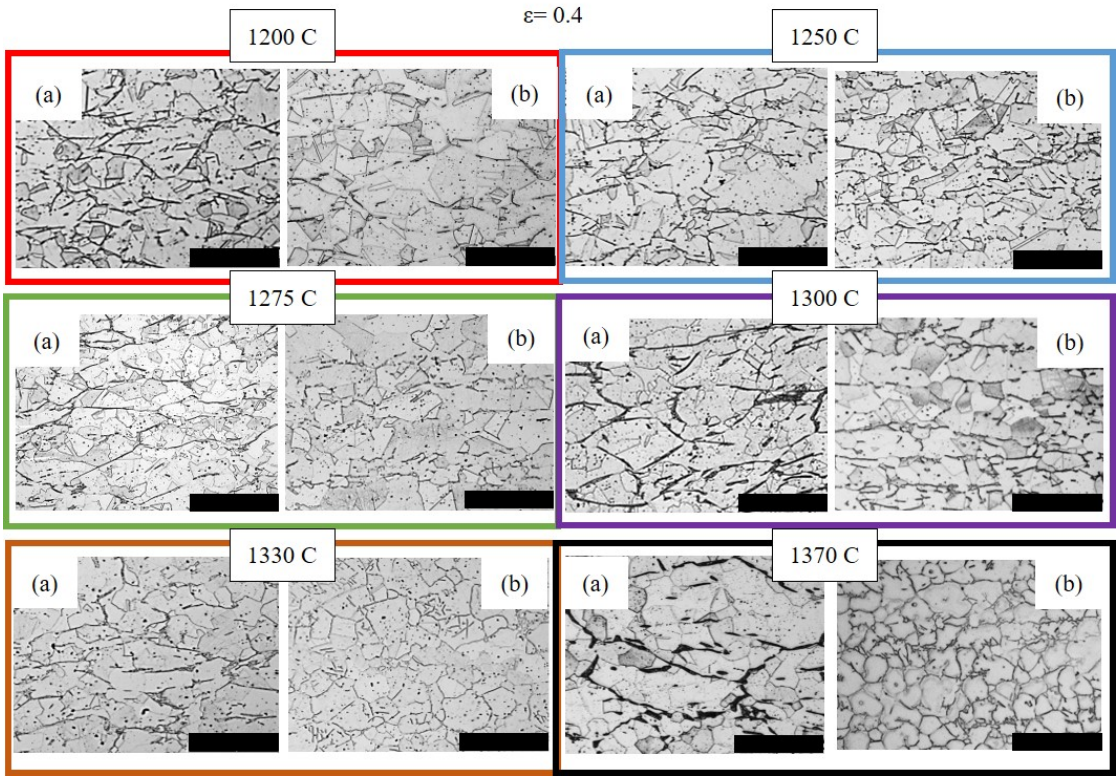

Figure 6.12: Optical microstructures at 0.4 of strain from 1200°C to 1370°C: (a) Quenched after deformation (b) Sample kept at different holding times (see Table 6.2). Scale bar: 200 µm

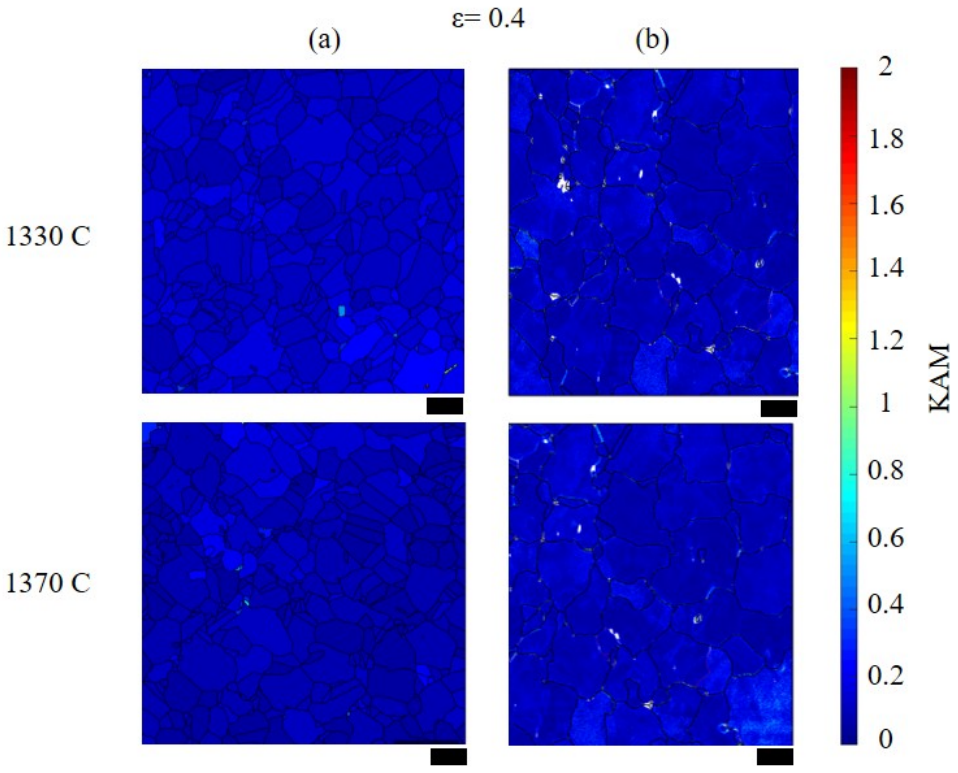

Figure 6.13: EBSD analysis at 1330°C and 1370°C: (a) No holding time (b) Holding time (see Table 6.2). Scale bar: 50 µm

As can be observed, no clear differences were reported in the microstructures for the samples with and without the holding time. Just slight variations seemed to appear with regard to the grain sizes. KAM criterion showed the presence of recrystallized grains in both cases and with similar recrystallized fractions. Low values of KAM are related to low dislocation density, fact which could be assumed to be an indicator of recrystallization.

Using the intersection method, the grain sizes were measured aiming to corroborate the previous assumptions. In Figure 6.14, the evolution of grain sizes against temperature for both cases is shown.

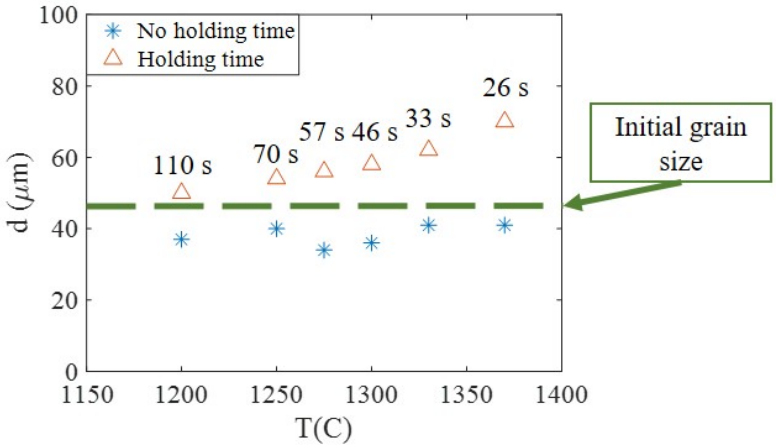

Figure 6.14: Commercial tests: grain size evolution over temperature

Under all the conditions tested, the grain sizes tended to increase with the temperature regardless of the holding time. Nevertheless, it should be highlighted that higher grain sizes were observed for the conditions with holding time. This fact is assumed to be due to this holding time. The sample is kept at high temperature during a certain time and this time facilitates grain growth. Therefore, these findings contradict the assumption that MDRX could play a role in the process, as higher grain sizes were obtained in the samples with holding time while if MDRX would have occurred, the grains should be lower.

6.3 RECRYSTALLIZATION GRAIN SIZES

After proving the occurrence of recrystallization, the knowledge of the grain sizes is of great interest to understand material properties and to develop robust models. Therefore, grain sizes were measured following the procedure explained in Chapter 4 and compared with those predicted by analytical equations reported in the literature, analysing both the microstructures obtained for the samples which had followed the non-commercial heating profile (called fast heating profile using the Gleeble, see Section 4.1.3.1) and those which followed the commercial one analysed in the previous section.

6.3.1 *Recrystallization grain sizes: results*

Examples of the microstructure of the fast heating profile are shown in Figure 6.15, taken by optical and EBSD method and showing the presence of delta ferrite under both conditions.

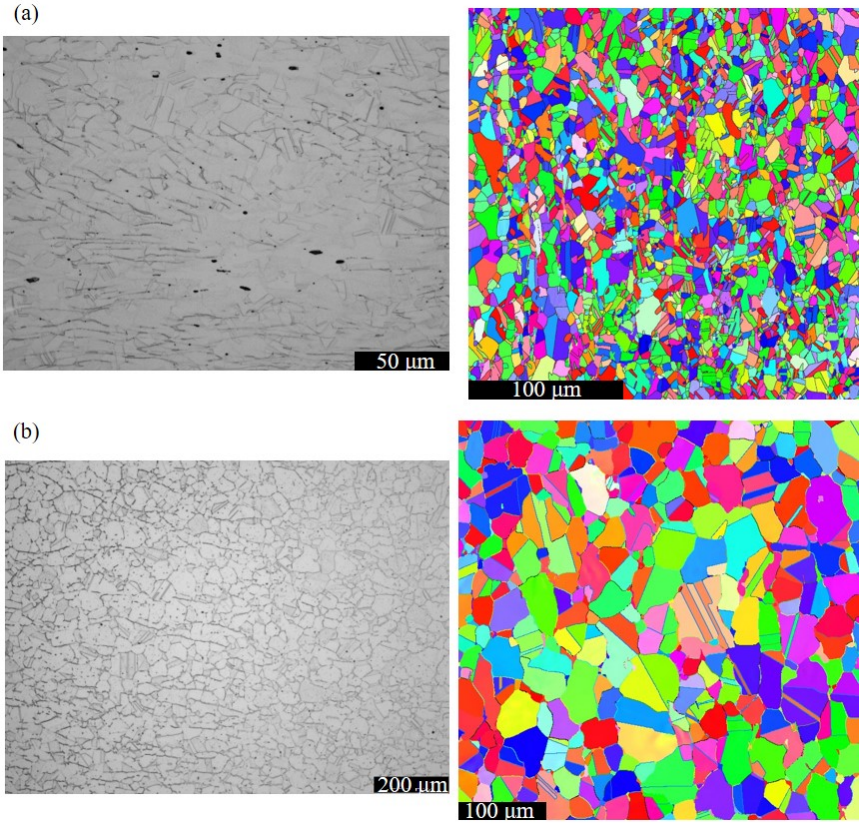

Figure 6.15: Microstructures with non-commercial heating profile at: (a) 1200°C (b) 1350°C

It is worth mentioning that the initial grain size at 1370°C was 50 µm, measured following the same procedure. Thus, the DRX grain sizes evolution can be seen in Figure 6.16. It should be highlighted that the grain sizes were measured only considering the recrystallized ones, regardless of the DRX fraction. An increasing trend was observed with temperature. In addition, it should be noted that the obtained values were notably lower than the initial grain size which could be considered to be beneficial for the process. It should be highlighted that the tests were stopped at a strain of 1.

In addition, an aspect which is usually not analysed in the literature is the influence of the heating profile on RX performance. The grain sizes were measured using the same procedure for the commercial heating profile and examples of the microstructures are shown in Figure 6.17.

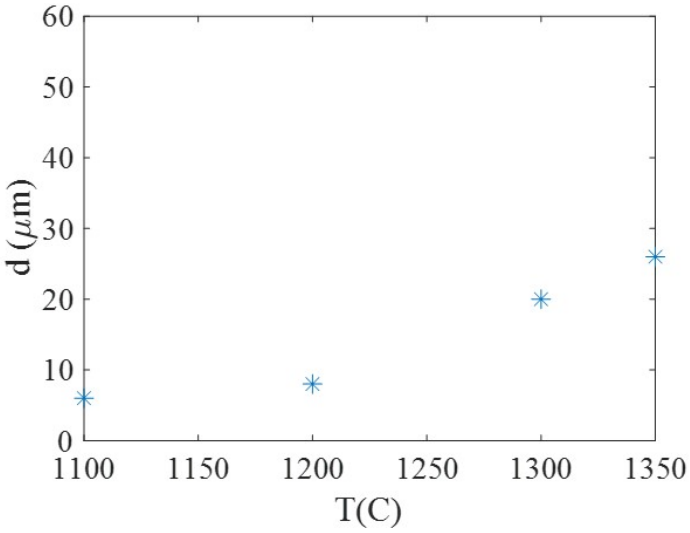

Figure 6.16: Non-commercial tests: recrystallized grain size evolution over temperature

The DRX grain sizes evolution for the commercial tests can be seen in Figure 6.14. In this case, the grain sizes remained almost constant regardless of the temperature. It is worth mentioning that the temperatures analysed were those which could be representative of the process, that is, higher than 1200°C. Although in this range of temperatures no clear variation was observed, it can be stated that the final grain sizes would be notably lower thanks to the recrystallization process as they were around 35 μm.

6.3.2 *Recrystallization grain sizes: discussion*

Apart from the experimental analysis done, it would be of great interest to be able to model the DRX grain sizes. Therefore, the obtained experimental results were compared with those predicted by the equations found in the literature (see Figure 6.5). The conditions are summarized in Table 6.1. The comparison of the measured values with the predictions can be seen in Figure 6.18.

As can be observed, no clear agreement was found between experimental and predicted results with none of the equations, especially at high temperatures, representative of the NSF process. These discrepancies are assumed to be due to the fact that the conditions employed in the literature are far from those, making extrapolation necessary.

As in the previous case, following the same analysis carried out with the non-commercial tests, the obtained experimental results for the commercial tests were compared with those predicted according to the literature (see Figure 6.19).

Again, no clear agreement was found. It should be highlighted that in this case, even the trend was not properly predicted. As mentioned above, these discrepancies are

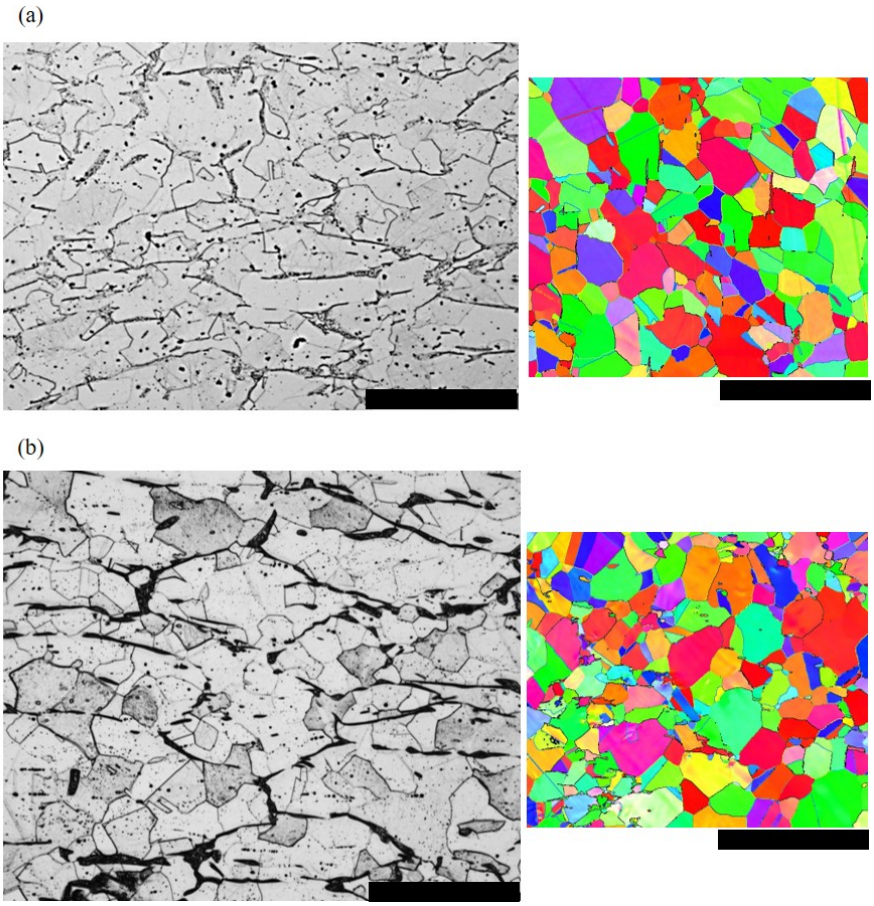

Figure 6.17: Microstructures with commercial heating profile at: (a) 1330°C (b) 1370°C. Scale bar: 200 µm

assumed to be not only due to the necessity of extrapolation but also due to the effect of delta ferrite distribution associated with this heating profile.

As was explained above, the commercial heating profile is notably slower than the traditional ones used for material characterization using Gleeble which was called fast heating rate. In spite of the differences on the heating profile, the initial grain sizes were almost equal, being 55 µm for the commercial tests. Therefore, the influence of the initial grain size is assumed to be negligible. The main discrepancies due to the differences on the heating rate were observed in the distribution of the delta ferrite throughout the sample. With the commercial heating profile, thanks to the higher heating time, the delta ferrite had enough time to distribute along the austenite grain boundaries. The differences on the amount of delta ferrite phase depending on the heating rate can be clearly seen in Figure 6.20.

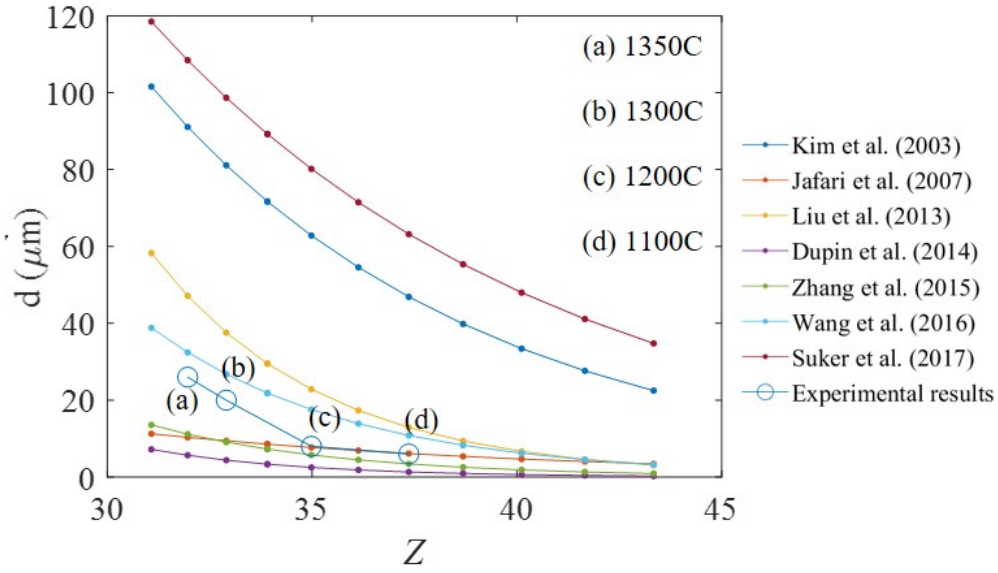

Figure 6.18: DRX grain sizes predictions and comparison with the non-commercial results (fast heating rate) at 10 s^{-1} and 1 of strain and at different temperatures

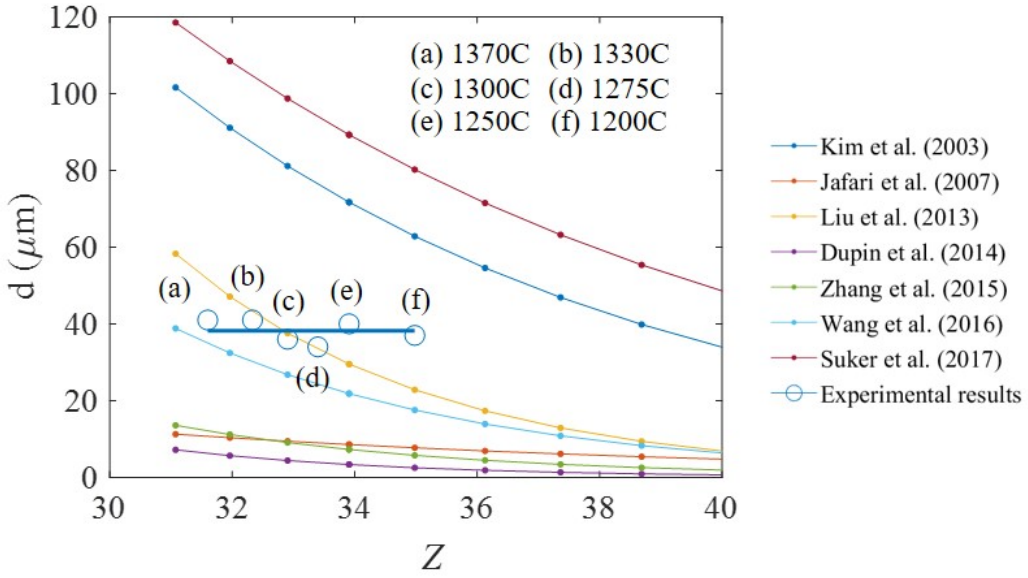

Figure 6.19: Commercial tests: DRX grain sizes predictions and comparison with the experimental results at 10 s^{-1} and at different temperatures

Although with both heating rates no agreement was found because of the necessity of extrapolation, there is a clear difference on the trend reported by the experimental results when comparing Figure 6.18 and Figure 6.19. With the fast heating rate (non-

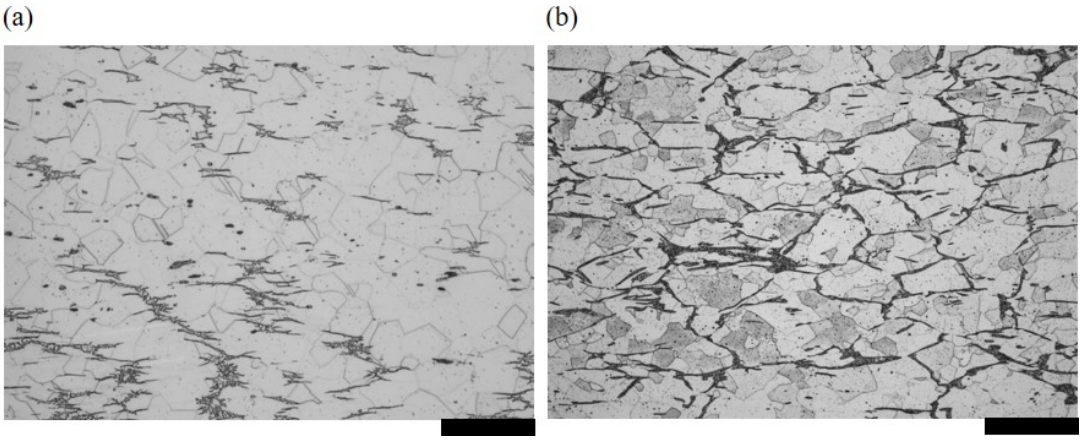

Figure 6.20: AISI 316 at 1370°C and 10 s^{-1} (a) Dilatometer heating rate (b) Commercial heating rate. Scale bar: 200µm

commercial tests) the trend was in accordance with what it would be expected, that is, an increase in the grain sizes (even though they are lower than the initial ones) with a decrease in Z, in other words, with an increase in temperature. Nevertheless, this trend was not observed in the samples subjected to the commercial heating rate.

As this commercial heating rate is notably slower than the other one, there is enough time for delta ferrite to nucleate and precipitate in the austenite grain boundaries. This issue is known to have a negative effect on dynamic recrystallization of austenite grains (Mataya et al., 2003 and Dehghan-Manshadi and Hodgson, 2008). Therefore, after proving the occurrence of dynamic recrystallization in AISI 316 under extreme conditions representative of the NSF process, the relevance of the heating profile was analysed and it was found that it clearly affects on delta ferrite formation, leading to a change in the trend in dynamic recrystallization grain sizes. It was also demonstrated that commonly used laws found in the literature to predict DRX grain sizes are not capable of reproducing the expected grain sizes under these extreme conditions because of the necessity of extrapolation as these temperatures have not been previously reported in the literature.

6.4 CONCLUSIONS

To sum up, the following conclusions can be drawn:

- The variation of the grain sizes with temperature and time was analysed covering a wide range of temperatures from the typical ones of forging to those representative of the NSF process. It was observed that, for both times, after overpassing a temperature of around 1275°C, the grain started to decrease. This trend is assumed to be due to delta ferrite formation. Delta ferrite was proven to influence microhardness,

as it increased with the amount of delta ferrite, and grain growth velocity with the opposite trend.

- The analytical results were experimentally validated through microstructural observations by carrying out tests stopping at 0.12 and 0.4 of strain. It was observed that at 0.12 no recrystallization took place, obtaining coarse grains. In contrast, at 0.4 recrystallization occurred and smaller grain sizes were observed.
- The possible existence of metadynamic recrystallization was also studied, by comparing the tests stopped at 0.4 with those stopped also at 0.4 but keeping a certain holding time to analyse grain size evolution. Higher grain sizes were observed due to this holding time.
- With the non-commercial tests (fast heating rate), in general, recrystallization was observed under all the conditions. However, at 1100°C (temperature assumed to be low for the NSF process), this recrystallization was not fully completed.
- Analysing the recrystallized grain sizes for the non-commercial case, although the obtained grains were notably lower than the initial ones under all the conditions, the value of the grain size tended to increase with temperature, following the expected trend reported in the literature.
- The commercial case was analysed covering the range of conditions representative of the NSF process, that is at temperatures higher than 1200°C. Under all these conditions recrystallization was observed as lower grain sizes were obtained.
- In the commercial case the grain sizes remained almost constant with the temperature, which is a trend in not agreement with what it could be expected. This issue was proven to be due to the high amount of delta ferrite formed because of the slowness of the heating. Delta ferrite influences recrystallization behaviour as has been previously stated in the literature.

7 LIFTING GEAR COMPONENT ANALYSIS

In previous chapters, the potential of using stainless steel under NSF conditions has been shown as recrystallization may take place, which would lead to small grain sizes even when the material is deformed at very high temperatures close to the solidus.

However, all the previous results, although they were obtained under close to these extreme conditions, are based on thermomechanical characterization set-ups whose conditions could still be far from those observed in reality. Therefore, NSF trials are needed to study the capacity for applying this process to austenitic stainless steel. This issue is going to be studied throughout this chapter. In addition, the experimental study of the hook geometry will be accompanied with numerical simulations to carry out a more in depth analysis of the process.

The main aim of choosing the hook geometry was to have at the same time a real geometry used in the industry which allows grain-size evolution throughout the part to be studied as a function of the strain reached.

Therefore, apart from proving the capacity for NSF of manufacturing stainless steel parts, the main aim of this chapter is to define an optimum process window for the NSF process taking into account not only mechanical issues but also microstructural aspects. Thus, based on the results from previous chapters it would be necessary to find a compromise between the process temperature defined in previous works by Lozares et al., 2020 and a proper microstructure with small grain sizes and reducing the amount of delta ferrite.

7.1 LIFTING GEAR COMPONENT: RESULTS

First, in terms of temperature, based on previous experiences recorded by Lozares et al., 2020, the temperature chosen was 1370°C as 0.95 times the solidus according to the results shown in Section 5.1. Although it was observed in previous chapters that slow heating rates lead to a higher amount of delta ferrite, the billet introduced in the muffle furnace followed the commercial heating profile as can be seen in Figure 7.1. This was the reason for testing the commercial heating profile during the characterization step shown in Chapter 5 and 6. With the aim of optimising the process window, in Chapter 6 it was proven that, due to the slowness of the heating rate, delta ferrite had enough time to nucleate and no remarkable difference was observed in terms of grain size with temperature (see Figure 6.19). Therefore, 1330°C was also tested aiming to reduce the amount of delta ferrite.

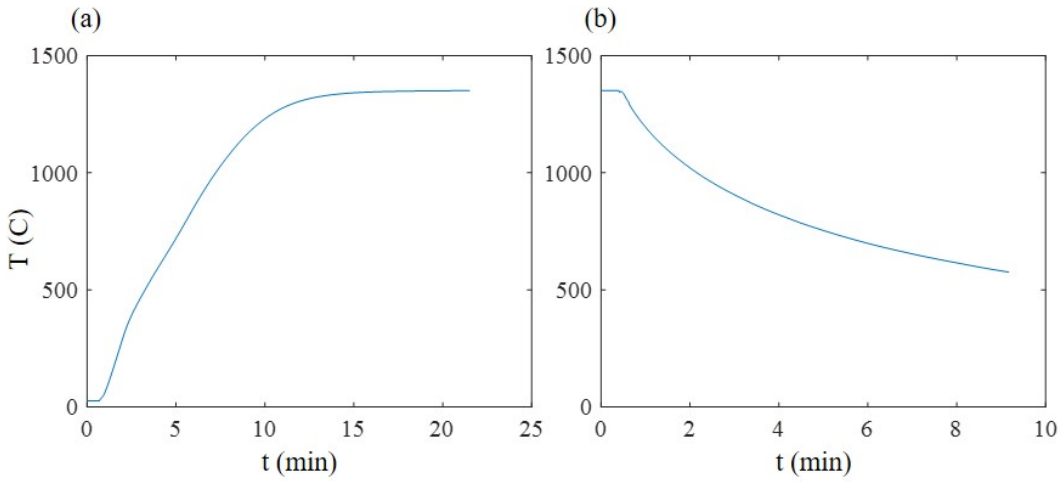

Figure 7.1: (a) Real heating profile of the billet (b) Real cooling profile of the billet

A numerical study of the capacity for the NSF process to be carried out was done according to the numerical model explained in Section 4.4. It is worth mentioning that the optimized flow stress law obtained in Section 5.3 was implemented aiming to obtain the most accurate results possible. The main input parameters were the stroke and the stroke rate in order to determine the expected load and the filling capability. That is why, two different stroke rates (50% and 5% of maximum stroke rate) and three strokes were analysed, being the maximum stroke rate 40 spm. The press velocity control is explained in Garcia, Ortubay, and Azpilgain, 2006.

For the case of 5% of maximum stroke rate, Figure 7.2 illustrates the force required to deform the billet, which was 1180 tonnes, for a stroke of 90 mm (the theoretical stroke necessary to fill the cavity), 610 tonnes for 85 mm and 490 tonnes for 80 mm. As the press used for experimental tests has a limit of 400 tonnes, even with the shortest stroke (which does not completely fill the cavity) the tests could not be conducted.

Thus, the stroke rate was increased ten times. As Figure 7.3 shows, in terms of force, with a stroke of 90 mm, 365 tonnes were needed while a stroke of 85 mm needed 170.6 tonnes and a stroke of 80 mm, 159 tonnes. Therefore, the experimental tests should be carried out at least at 50% of stroke rate, as at lower stroke rates there could be enough time for the sample to cool, leading to higher forces as was observed.

It is known that temperature plays an important role in recrystallization (see Chapter 6). Numerical simulations allow the effect of temperature on plastic strain to be studied. Thus, different simulations were carried out by varying the temperature from 1370 to 800°C. In these simulations, the force limit of the press was set to 400 tonnes in order to be as close as possible to the real press explained in Section 4.3. Figure 7.4 depicts the strain field obtained at each temperature analysed.

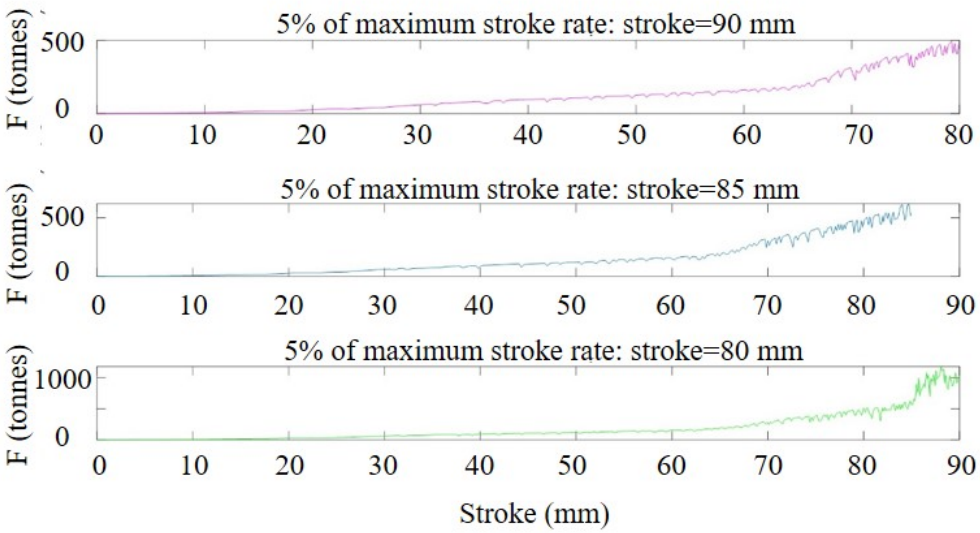

Figure 7.2: (a) 5% of maximum stroke rate and 90 mm of stroke (b) 5% of maximum stroke rate and 85 mm of stroke (c) 5% of maximum stroke rate and 80 mm of stroke

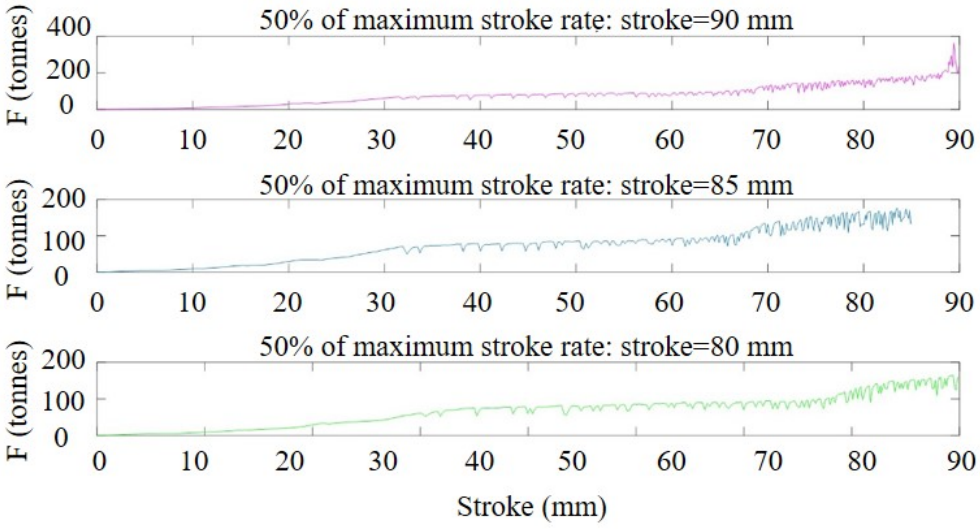

Figure 7.3: (a) 50% of maximum stroke rate and 90 mm of stroke (b) 50% of maximum stroke rate and 85 mm of stroke (c) 50% of maximum stroke rate and 80 mm of stroke

As can be seen in Figure 7.4, no remarkable difference was observed between 1370 and 1260°C and the only difference noticed was in the press force needed to fill the cavity. At 1000°C the press force was not enough to deform the billet whereas at 800°C the force expected was observed to be more than double the limit. Therefore, when the cavity

is completely filled, the strain field obtained is governed by the geometry. Regarding recrystallization, in the zones where the plastic strain is higher than the critical one, dynamic recrystallization would be expected.

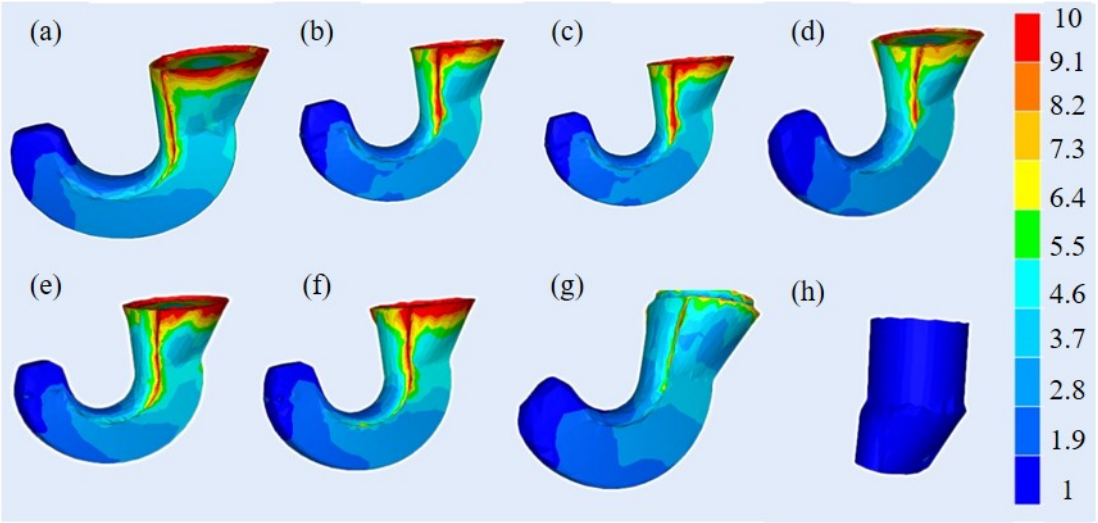

Figure 7.4: Strain fields at (a) T=1370°C (b) T=1340°C (c) T=1320°C (d) T=1300°C (e) T=1280°C (f) T=1260°C (g) T=1000°C (h) T=800°C

Based on these numerical results, different trials were carried out with 50% of the stroke rate at 1330°C and 1370°C. For instance, the force recorded at 1370°C is shown in Figure 7.5.

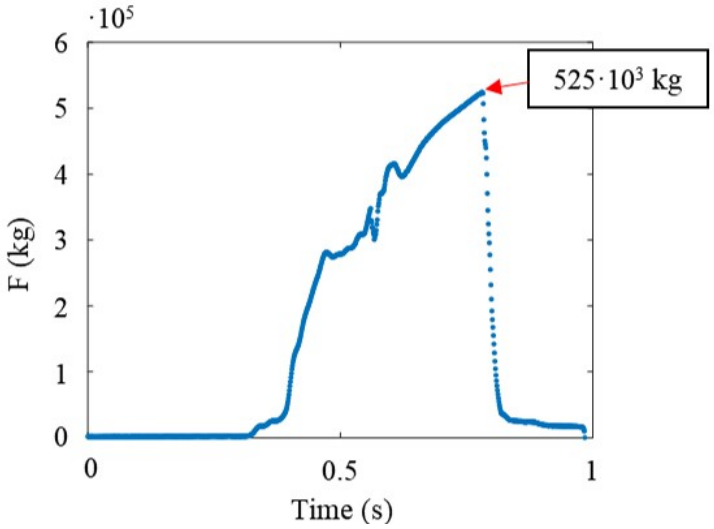

Figure 7.5: Force recorded during hook test at 1370°C

The maximum value was around 100 tonnes higher than the theoretical maximum achievable by the press (see Section 4.3). In comparison with the numerical result (see Figure 7.3a), the experimental value was around 100 tonnes higher. In addition, although the measured force was slightly higher than the maximum achievable by the press, it was able to fill the cavity. No clear differences were observed at the two temperatures tested, that is why just Figure 7.5 was included as an example.

Lastly, Figure 7.6 shows the experimental parts obtained under both conditions. Therefore, the NSF process has been clearly demonstrated the capacity for manufacturing stainless steel parts. The aim of using this geometry is to analyse how the microstructure varies throughout the part under different conditions of strain and strain rate to generate a more in depth knowledge about the reasons which lead this process to work. A comprehensive microstructural analysis (grain-size determination) will be carried out in the following section.

Figure 7.6: (a) 1330°C (b) 1370°C

7.2 LIFTING GEAR COMPONENT: DISCUSSION

The aim of this section is to carry out a comprehensive study of microstructural evolution due to the NSF process. The lifting gear component permits analysis of the influence of plastic strain on the final microstructure by taking different samples throughout the part. The strain distribution can be seen in Figure 7.4. The obtained grain sizes will be compared with those measured in Chapter 6.

The experimental results were accompanied with numerical simulations. The main aim of these simulations was, first, to estimate whether recrystallization could have taken place or not (that is, if the plastic strain was higher than critical) and, second, to estimate the temperature and strain rate throughout the part in order to analyse the results. The values of strain rate and temperature were taken as an average value based on the numerical fields at different zones of the part. These predictions were compared with those measured in the experimental part.

7.2.1 *Experimental case I: 1370°C*

As has been previously mentioned, numerical simulations of the lifting gear component were carried out in order to, at least, estimate whether recrystallization could occur during the process or not. Therefore, Forge NXT® was used to estimate the differences in temperature and strain rate throughout the part (see Figure 7.7) as grain sizes could be notably influenced by process conditions.

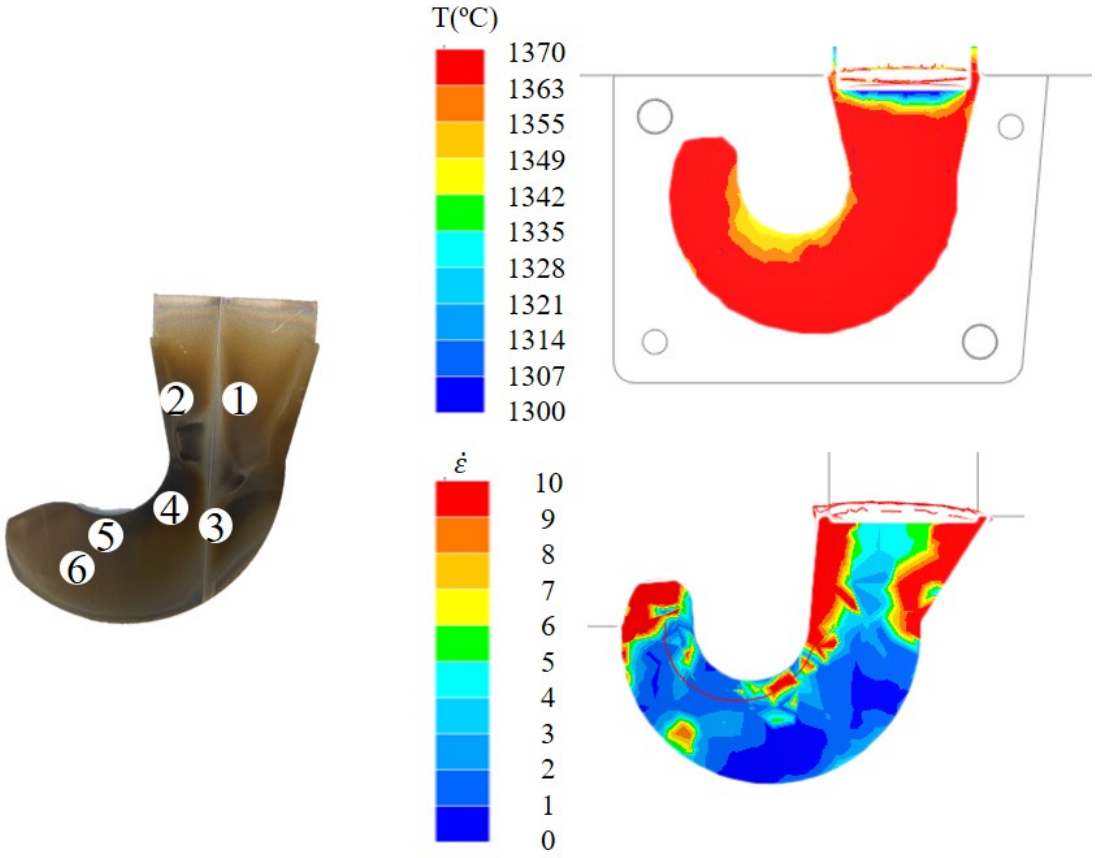

Figure 7.7: Temperature and strain rate profiles for the test at 1370°C

The conditions observed in the real part (according to numerical simulations) were notably variable, which could lead to a variation in grain sizes. Table 7.1 summarizes the conditions reached of strain rate and temperature in the different zones highlighted in Figure 7.7. It is worth mentioning that, as this high variation was expected, for the experimental characterization a strain rate of ten was chosen as an average value (see Figure 4.18).

Table 7.1: Strain rate and temperature in different zones throughout the part for the trial at 1370°C according to Forge NXT® simulation

Zones	1	2	3	4	5	6
T (°C)	1380	1370	1370	1350	1350	1370
$\dot{\varepsilon}$ **(s^{-1})**	5	20	1	5	10	5

Therefore, different samples were taken from the bulk and analysed in the optical microscope and by EBSD method (see Figure 7.8). The zones were chosen to be representative of the whole part, covering a wide range of temperatures and strain rates throughout the part as is shown in Table 7.1. For the sake of comparison, in Figure 7.8, just one Gleeble condition was included (following the commercial heating profile, see Section 4.1.3.1), as based on the results shown in Table 7.1 it was expected to be the most representative one.

Applying the same method as the one explained in Section 4.1.1, the recrystallized grain sizes were measured for each sample. In order to analyse the results globally, the Zener-Hollomon parameter (Z), calculated based on numerical results, was determined for each zone. It can be seen that the grain sizes tended to decrease for high values of Z, the grain sizes being greater in the core. To analyse the effect of process conditions on the mechanical properties of the final part, microhardness measurements were also carried out.

Concerning microhardness analysis, a Vickers indenter was employed in the etched sample with a load of 2 kg to ensure enough resolution and an average value. In Figure 7.9 the correlation between microhardness measurements and grain sizes can be seen. The values of the microhardness tended to increase with the decrease of the grain size. Therefore, thanks to the NSF process the part had a harder shield covering the internal part, which was expected to be more ductile due to the greater grain sizes and the lower microhardness.

Based on the conditions shown in Table 7.1 and also depicted in Figure 7.8, similar microstructures to those obtained during thermomechanical characterization at 10 s^{-1} would be expected (see Figure 4.18). First, it is worth highlighting that, the trend followed by the experimental results considering the Zener-Hollomon parameter was consistent. As can be seen, the main similarities were found between the external microstructures and those from the Gleeble whereas, in the core, notably greater grain sizes were observed although the estimated conditions were supposed to be close to those of the characterization. It should be highlighted that the material tends to be self-heated due to the deformation process which could lead to higher temperatures than expected. This issue, together with the fact that it is more difficult to exhaust the heat from the core would result in greater grain sizes due to these higher temperatures, although grain growth could be limited due to the formation of delta ferrite. This was observed to some

extent in Figure 7.8 but the differences in the conditions were too low to support this assumption.

In the external zones, although the sample is also self-heated, the temperature should be lower as it is in direct contact with the cool dies, thus, lower grain sizes were measured. In addition, the external surface of the billet was heated faster, reaching the set temperature before than in the core and thus not following the commercial heating profile. On this basis, the simulation was carried out again modifying the thermal exchange between the billet and the dies.

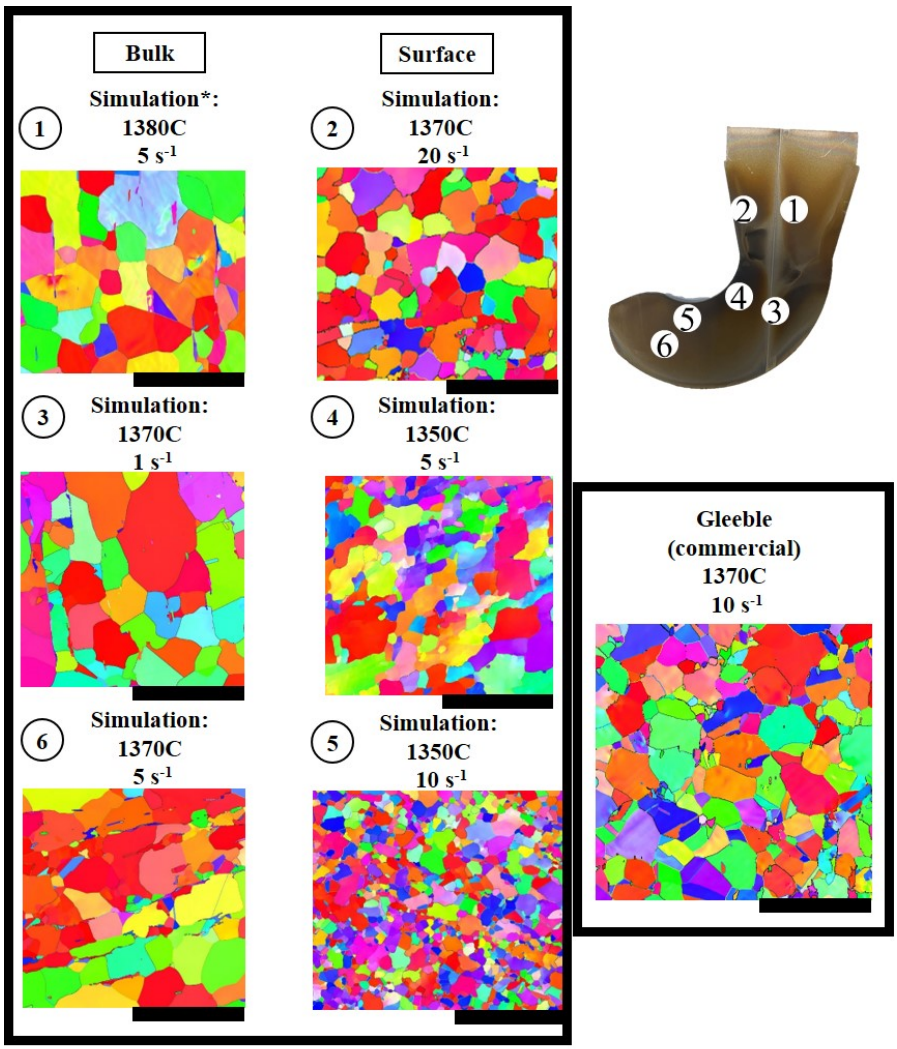

Figure 7.8: Comparison between microstructures of the final part and those obtained with the thermomechanical characterization. Scale bar: 100µm. Temperature and strain rate indicated in Zones 1 to 6 were taken from Forge NXT® (see Table 7.1)

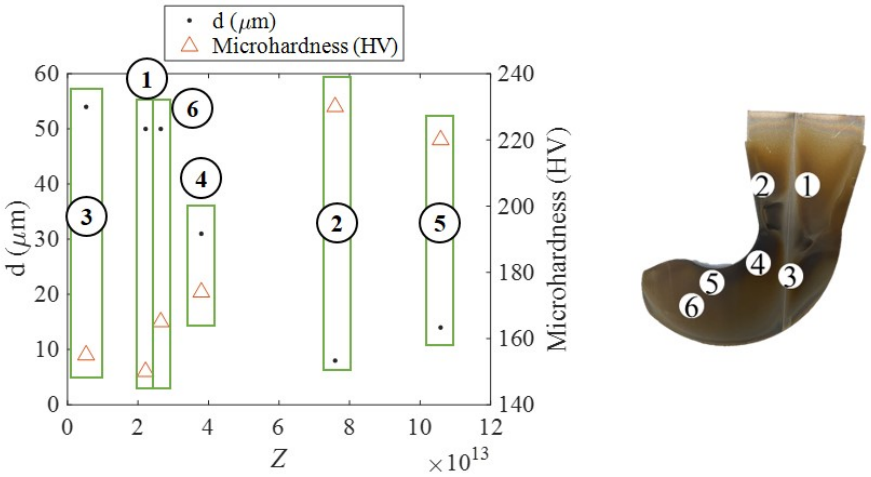

Figure 7.9: Microhardness variation throughout the part in comparison with grain sizes (trial at 1370°C)

This decision was taken based on the fact that the thermal exchange between the part at a very high temperature and the cool dies would be high, causing a notable reduction of the temperature of the billet especially in the external part. In Figure 7.10, the thermal profile of the bulk with the lowest and the highest value of the thermal exchange are shown.

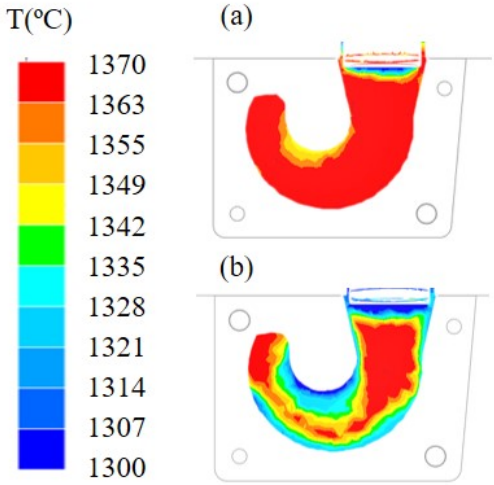

Figure 7.10: Temperature profile: (a) Low thermal exchange coefficient (b) High thermal exchange coefficient

As can be seen, slight differences in temperature were reported in the zones 1, 2, 3 and 6. However, the zones 4 and 5 were cooled to around 1300°C. For instance, the

microstructures observed in zones 4 and 5 were similar to those observed in Figure 6.11 but between 1200 and 1300°C, proving that other aspects such as the thermal exchange could be playing a role, as these samples were heated following a faster heating rate than the one used for the commercial case. The results are shown in Figure 7.11.

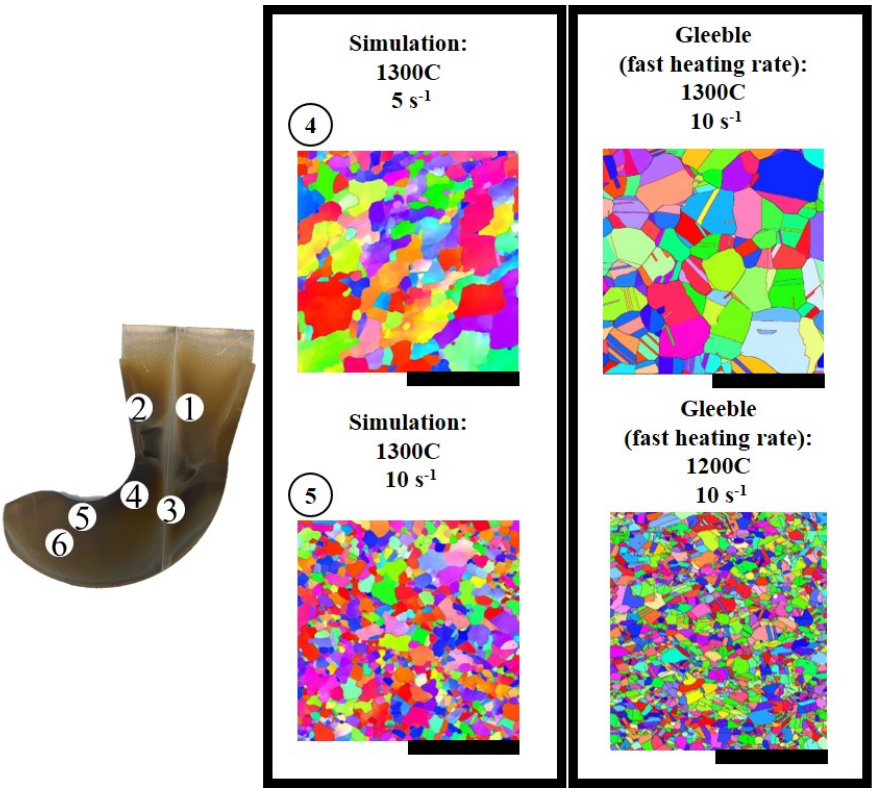

Figure 7.11: Comparison between microstructures of the final part at 1370°C (zones 4 and 5) and those obtained with the thermomechanical characterization following the fast heating rate. Conditions after changing the thermal exchange. Scale bar: 100µm

As can be seen, the microstructures observed in the hook part were closer to those at 1200 and 1300°C, probably being at an intermediate temperature. The value of 1300°C reported by the simulations should be taken with care as the real thermal exchange between the dies and the part is not characterized. Therefore, it can be assumed, due to the large difference in temperature between the part and the dies, that the sample would tend to cool down faster than was estimated by the numerical simulation.

In addition, the final microstructure may be notably influenced by the formation of delta ferrite which could affect grain growth and restoration mechanisms, and, thus, the final mechanical properties of the part, as was deeply analysed in Chapter 6. For instance, Figure 7.12 shows the optical microstructures at different zones of the hook, showing the presence of delta ferrite in all the regions.

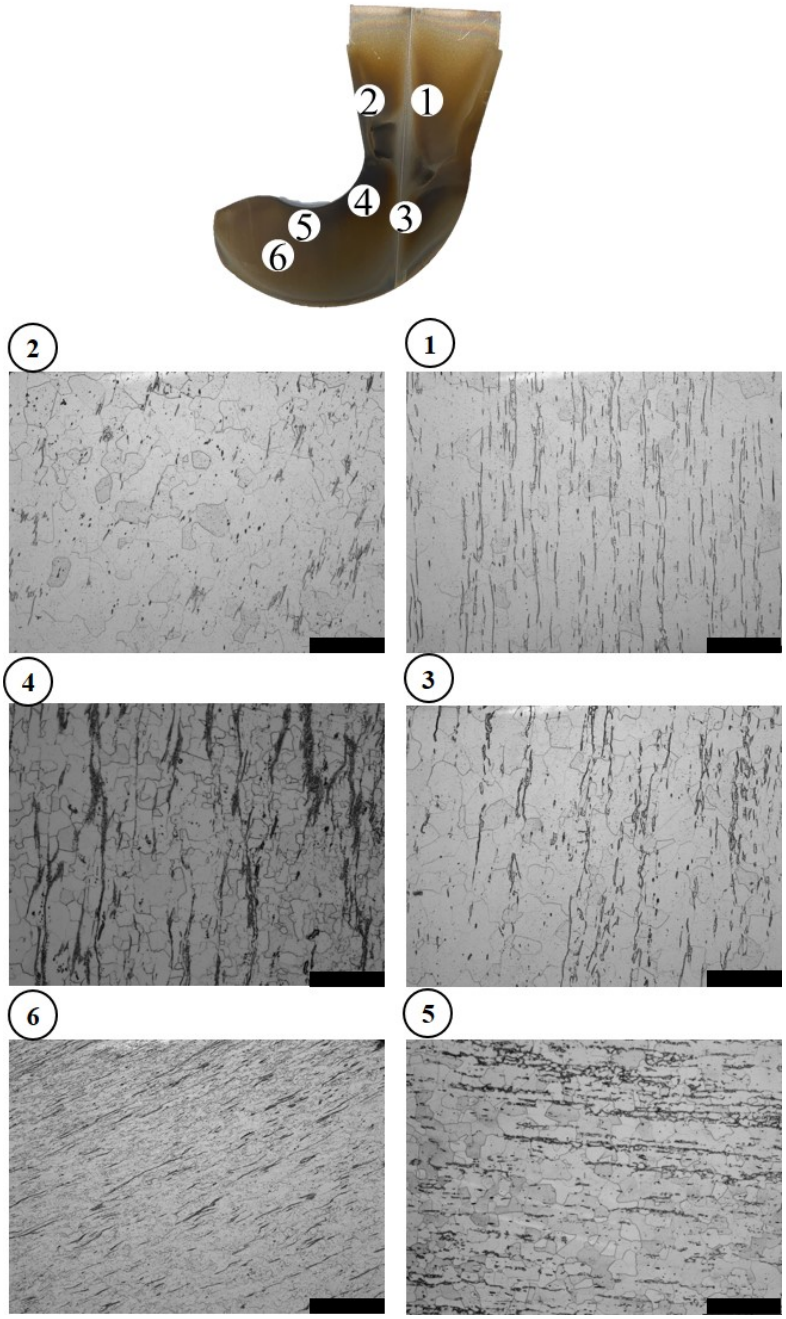

Figure 7.12: Optical microstructures of the lifting gear component at 1370°C. Scale bar: 200µm

7.2.2 *Experimental case II: 1330°C*

It would be of great interest to optimize the process window aiming to obtain lower grain sizes and to reduce the formation of delta ferrite. In Chapter 6 it was observed that the

higher the temperature and the holding time, the higher the amount of delta ferrite there was. Therefore, it would be necessary to find a compromise between being close to the solidus temperature as stated by Lozares et al., 2020 and reducing the amount of delta ferrite in the final part which was proven to affect the mechanical properties (as was analysed in Section 6.1). Therefore, a trial was carried out at 1330°C as a lower delta ferrite fraction was expected based on the results shown in Figure 6.7.

Table 7.2 summarizes the conditions reached of strain rate and temperature according to the numerical simulations using the highest value of the thermal exchange, taking into account the results shown in previous section.

Table 7.2: Strain rate and temperature in different zones throughout the part for the trial at 1330°C according to Forge NXT® simulation

Zones	1	2	3	4	5	6
T (°C)	1340	1300	1330	1280	1330	1280
$\dot{\varepsilon}$ **(s^{-1})**	5	25	3	15	5	20

Different samples were analysed from the bulk using the optical microscope and the EBSD method, measuring the grain sizes to be compared with those from the Gleeble following the commercial heating profile in a first approach (see Figure 7.13). It should be highlighted that the test in the Gleeble was carried out by preheating the sample up to 1370°C reproducing the commercial heating profile.

Based on the conditions shown in Table 7.2, similar microstructures to those from the Gleeble (the commercial ones) at 10 s^{-1} would be expected, similar to that analysed in the previous section. According to the simulation, under these conditions the strain rates reached were slightly higher. Nevertheless, the average value of 10 s^{-1} is still representative. The main similarities between the Gleeble microstructure and the experimental ones were found in the zones 1 and 2, and the differences in the grain sizes are assumed to be due to a slight variation in the temperature and strain rate.

Smaller grain sizes were observed in the zones 4 and 5, similar to what was found for the other hook. Therefore, microhardness measurements were also taken from the etched samples. As can be seen in Figure 7.14, the values of the microhardness tended to increase with the decrease of the grain size, leading to the same conclusion as in the previous case. It can be seen in Figure 7.14 that the grain sizes followed the expected trend, having higher grain sizes for the lower values of Z, although it is worth mentioning that the value of Z was calculated based on the results reported by the simulation.

As mentioned above, zones 4 and 5 reported the smallest grain sizes not being in agreement with those obtained from the thermomechanical characterization at 1330°C. In Figure 7.15, similar to what was shown in Figure 7.11, it can be seen that the microstructures observed in the hook part were closer to those obtained between 1200 and 1300°C (note that the samples were preheated to 1370°C).

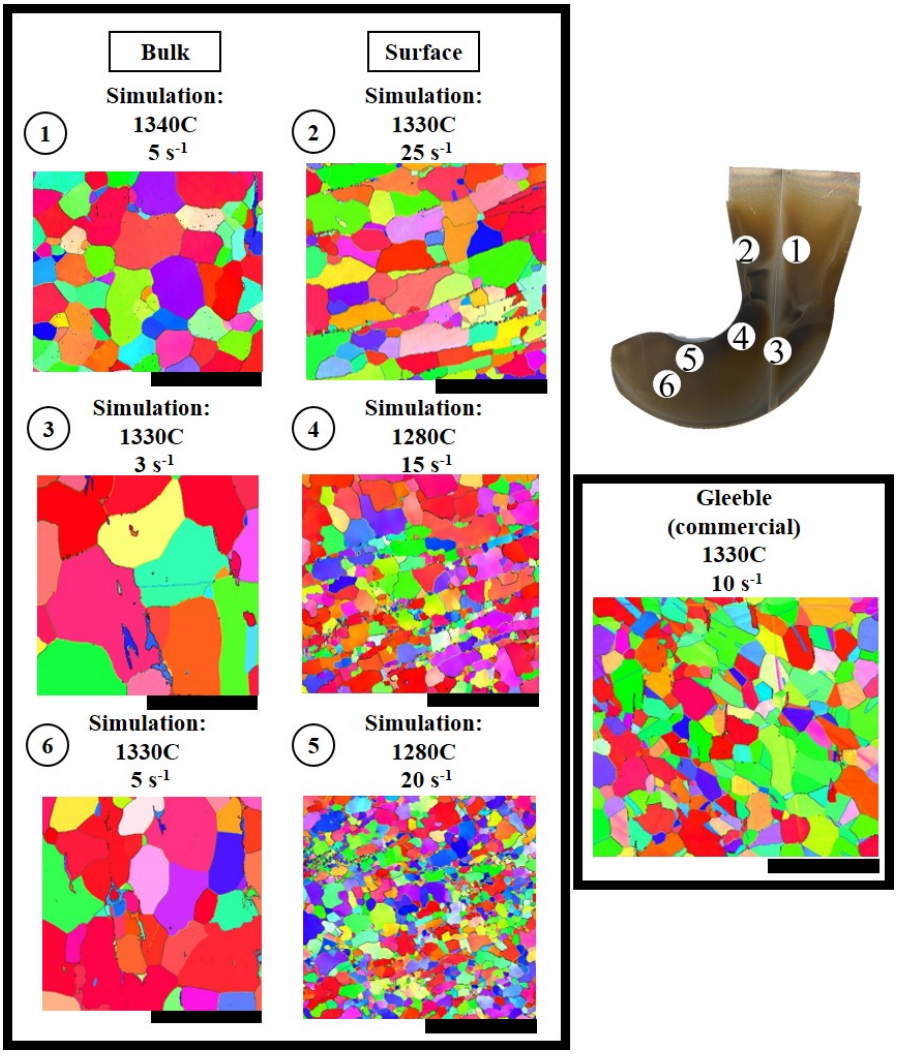

Figure 7.13: Comparison between microstructures of the final part and those obtained with the thermomechanical characterization at 1330°C. Scale bar: 100µm

It is worth mentioning that the numerical simulation showed that the temperatures could go down up to these values, although variations in the strain rates were also observed.

Although the aim of the test at 1330°C was to look for smaller grain sizes due to the fact that the temperature was lower, it was observed that, surprisingly, regardless of the zone analysed, the microstructures obtained were quite similar in spite of the fact that, according to the simulation, the conditions should be totally different. Figure 7.16 depicts these results.

On this basis, taking into account the results obtained, the possible formation of delta ferrite throughout the sample was analysed as can be seen in Figure 7.17.

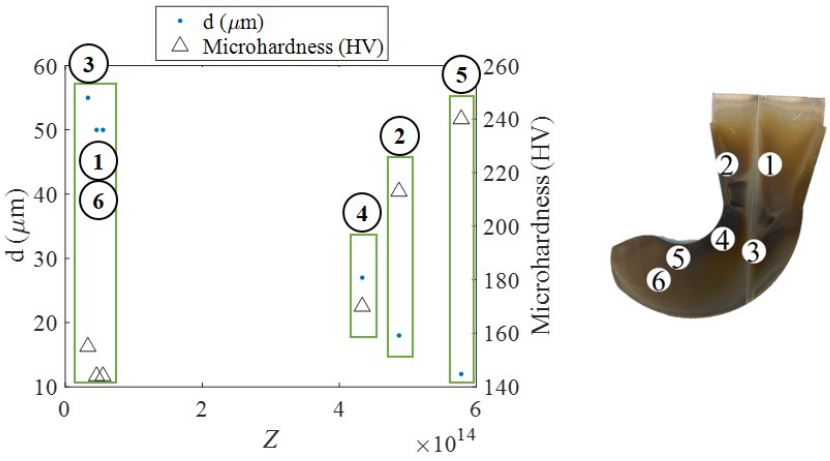

Figure 7.14: Microhardness variation throughout the part in comparison with grain sizes (trial at 1330°C)

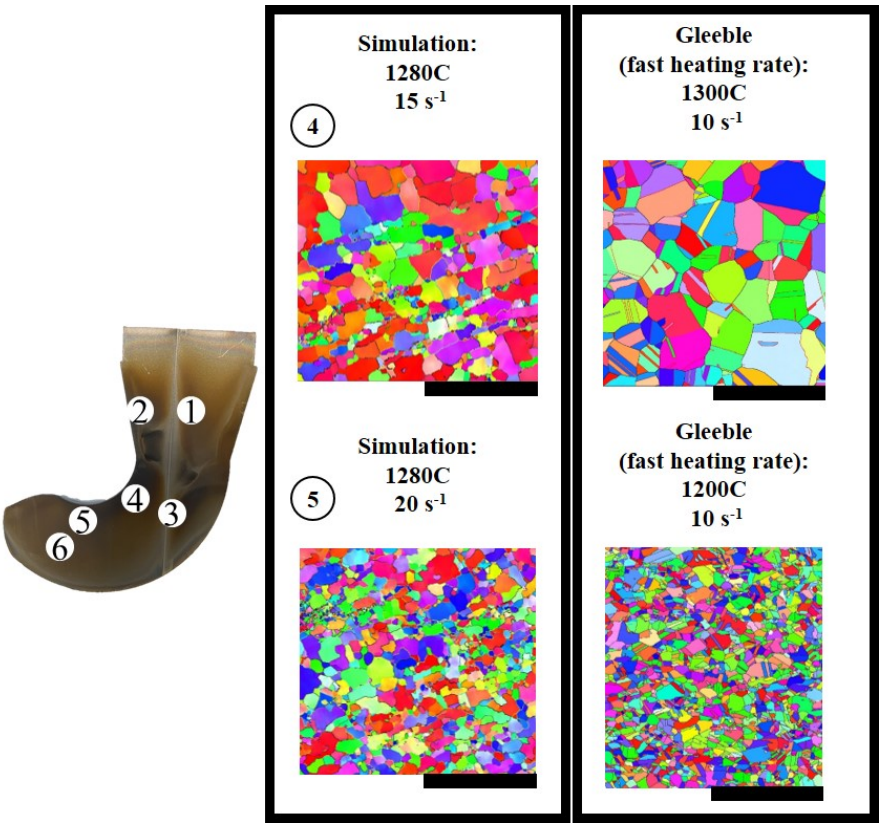

Figure 7.15: Comparison between microstructures of the final part at 1330°C (zones 4 and 5) and those obtained with the thermomechanical characterization following the fast heating rate. Conditions after changing the thermal exchange. Scale bar: 100µm

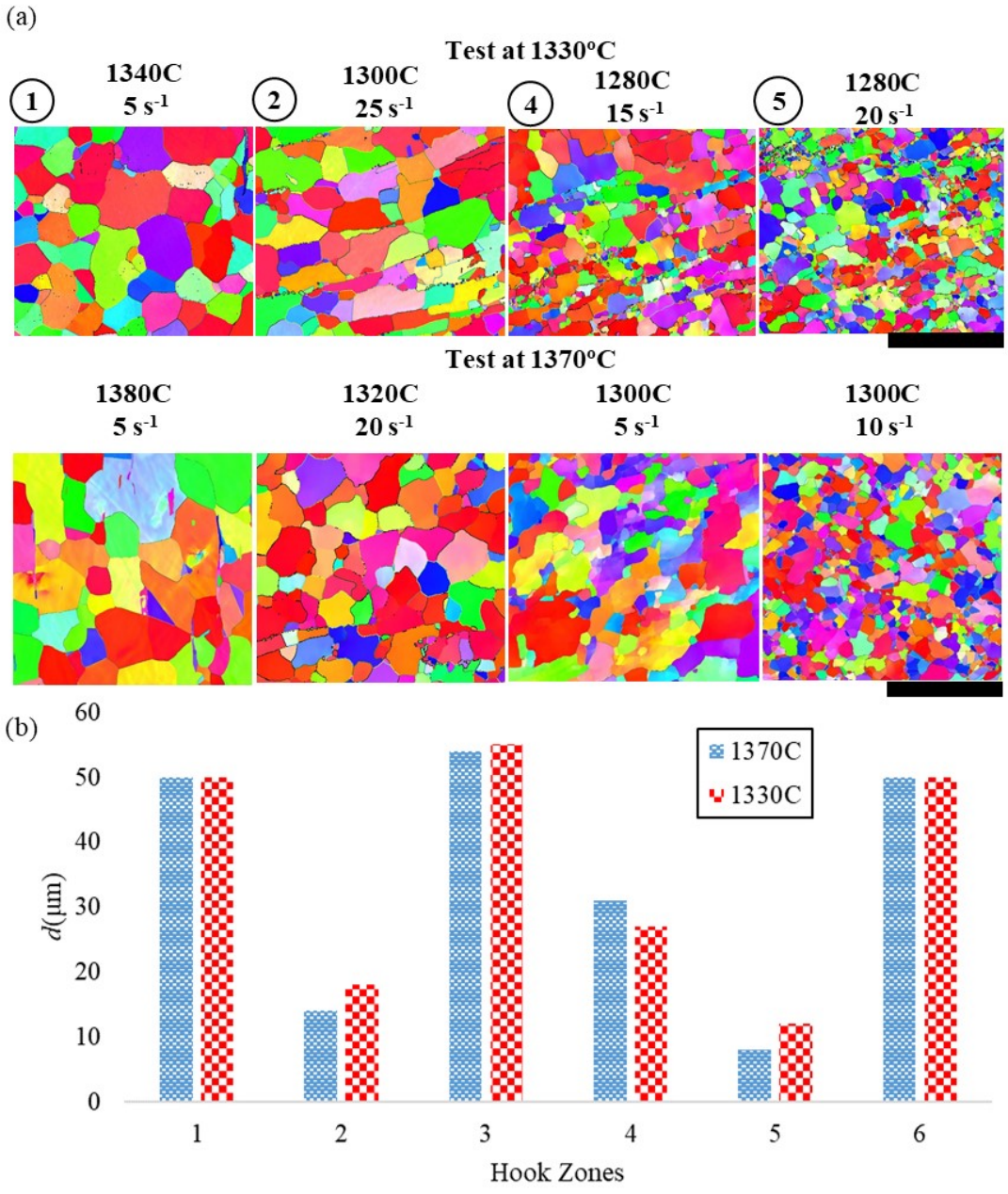

Figure 7.16: Grain sizes comparison for the hooks at 1330 and 1370°C. (a) Microstructural comparison (b) Grain sizes comparison. Scale bar: 100µm

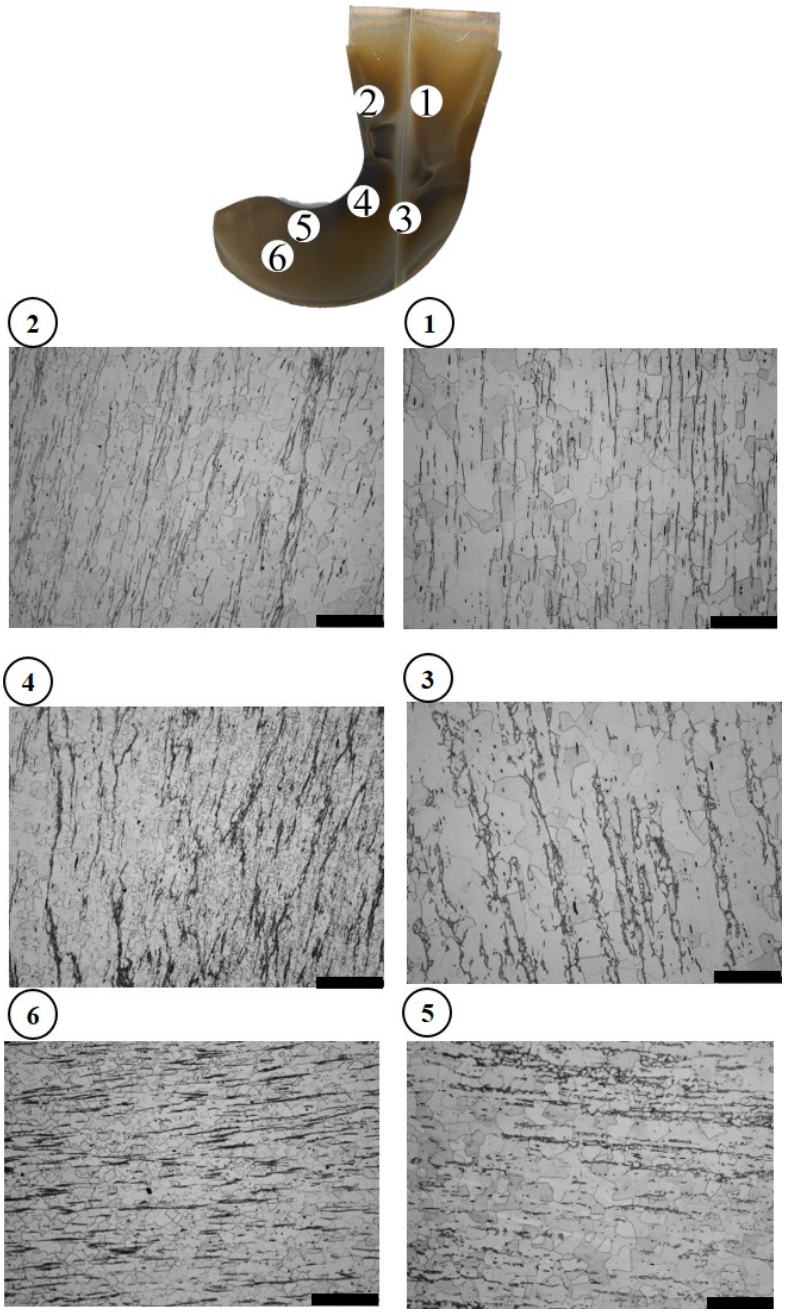

Figure 7.17: Optical microstructures of the lifting gear component at 1330°C. Scale bar: 200µm

Again, it seems clear that delta ferrite is playing a role in the microstructure evolution due to the NSF process. Comparing both conditions (see an example in Figure 7.18), it can be observed that not only the final grain sizes but also the amount of delta ferrite did not show remarkable differences. Although the aim of testing the billet directly heated up to 1330°C was to look for lower amount of delta ferrite, this was not reached as can be seen in Figure 7.18. It is assumed that, despite the fact that the temperature was lower, the billet remained around 20 minutes in the furnace at the set temperature in order to ensure temperature homogeneity throughout the sample. This holding time encourages the nucleation of delta ferrite. This amount of delta ferrite may explain why the obtained microstructures tended to be quite similar regardless of the temperature of the tests as it has been analysed in Chapter 6.

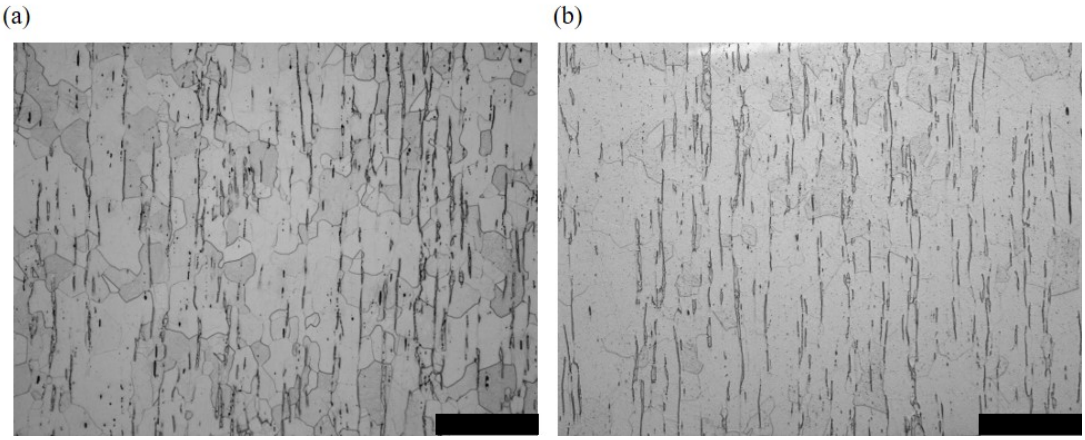

Figure 7.18: Comparison between the lifting gear component at: (a) 1330°C (b) 1370°C. Scale bar: 200µm

To summarize, the temperature of 1330°C was chosen looking for a compromise between the NSF temperature working range and microstructural aspects, that is aiming to facilitate recrystallization by reducing the amount of delta ferrite. According to the results shown in Section 6.1, just by heating the sample following the commercial heating profile in the muffle furnace, delta ferrite tended to appear at temperatures over 1300°C, becoming more prominent at higher temperatures close to the solidus. However, in spite of the temperature reduction, due to the slowness of the heating rate which leads to high holding times, there was enough time for delta ferrite to nucleate. Therefore, although it is clear that temperature in the NSF tests plays a relevant role there are much more aspects that need to be considered.

It was proven that the thermal exchange (in the case analysed consisted of the contact between the billet and the dies) is an important factor as it could cause the sample to cool down quickly even before the trial changing the material behaviour from what it could be expected. In addition, it should be highlighted that the simulation does not consider the time spent to transfer the billet from the oven to the dies which notably

causes a decrease in temperature as, at these high temperatures, radiation acts quickly. For instance, the cooling rate of the sample was measured through a S-thermocouple in the centre of the billet, obtaining an average cooling rate of 1.6°C/s.

Finally, the heating rate is another relevant aspect to be studied as it could reduce the formation of delta ferrite as has been analysed in Chapter 6, facilitating the recrystallization of the grains aiming to obtain lower grain sizes with a lower delta ferrite fraction which is assumed to lead to better material behaviour.

7.2.3 *Influence of the preheating and the heating rate*

One of the main findings of this work lies in the fact that the preheating and the heating rate at which the sample is subjected could have a notable influence on the expected results. For instance, in Chapter 5 it was observed that the flow stress behaviour varied from one sample to other which was heated faster. In a similar way, the final microstructure also varied remarkably as it was observed in Chapter 6.

The main reason explaining this behaviour was proven to be the formation of high amount of delta ferrite at the high temperatures employed in the trials. In Chapter 5 and 6 all the samples were previously heated up to 1370°C, aiming to homogenize the microstructure in order to have the same initial grain sizes and to reproduce the expected microstructure during the NSF process. This heating, especially in the case called as commercial, had a notable relevance as, because of its slowness, allowed delta ferrite to nucleate and precipitate to the austenite grain boundaries. Delta ferrite influences grain growth kinetics (see Section 6.1) but also the possible occurrence of restoration mechanisms such as recrystallization as stated in Section 6.3. The relevance of delta ferrite on the industrial process was also observed in previous sections as the same microstructure was obtained when manufacturing the lifting gear component regardless of the temperature. This was assumed to be due to the slow heating rate achievable in the muffle furnace.

Therefore, it seems clear that, although NSF process was proven to be able to manufacture stainless steel complex parts, the preheating temperature and the heating rate are two relevant aspects which will need more focus in further research.

For instance, after all the comprehensive analysis carried out, two more conditions were tested in the dilatometer (see Section 4.1.3.2) heating up the samples directly to 1300°C and 1330°C. Although it is known that at these temperatures delta ferrite could also be formed, especially because of the deformation conditions, it is assumed that, due to the fast heating profile, the generated amount would be much lower. The microstructures obtained can be seen in Figure 7.19.

As can be observed, both results reported lower grain sizes with less delta ferrite in comparison with the preheated test (see Figure 7.19-b). Thus, it was proven that by having a proper control of the temperature and the heating rate, much finer microstructures

with lower amount of delta ferrite would be obtained which may be a beneficial issue for the NSF process.

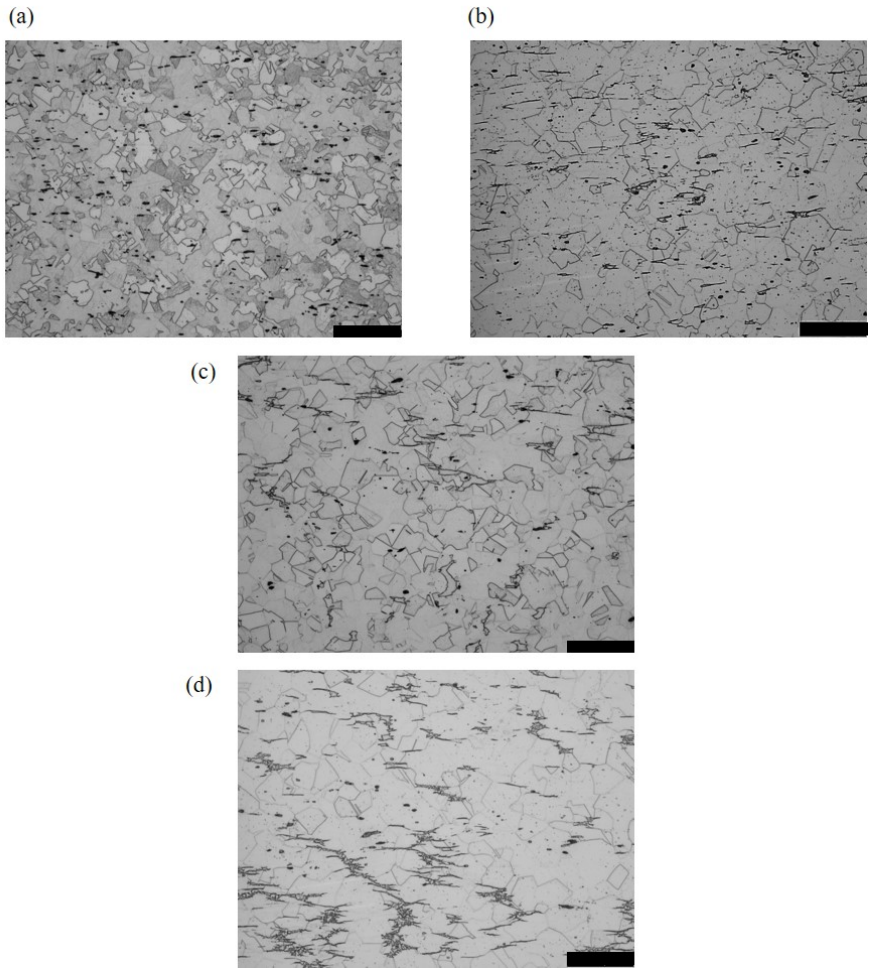

Figure 7.19: (a) 1300°C (b) 1370°C then 1300°C (c) 1330°C (d) 1370°C. Scale bar: 100µm

7.3 CONCLUSIONS

To sum up, the following can be concluded:

- The manufacturing of stainless steel parts, especially with regard to complex parts, is still a challenge as traditional forging operations are expensive and imply many steps, which results in a high amount of material waste. NSF was proven to be able to manufacture stainless steel complex parts in a single step.

- After proving the capacity for the NSF process, a lifting gear component was manufactured at two different temperatures to understand this process. The first microstructural analysis, together with numerical simulations, proved that the conditions would be enough to ensure recrystallization take place. The results were compared with those from the thermomechanical simulation observing high variability in the microstructure throughout the NSF part. This was proven to be due to a combination between the variability on the conditions reached and the strong differences in the heating profile that may appear between the surface and the bulk.

- Thermal exchange was proven to be an important factor to be taken into account. The microstructures observed in the hook part were not in agreement with those that were supposed to be obtained under the same conditions with the Gleeble but it was observed that they were closer to those between 1200 and 1300°C obtained with the fastest heating rate, implying that the real temperature of these zones could be notably lower than in the core.

- The aim of testing the NSF process at 1330°C was to look for an optimum process window, obtaining microstructures with a lower amount of delta ferrite. However, no clear differences were observed as, although the heating rate could be faster on the surface than in the bulk, the holding time needed to ensure thermal homogeneity throughout the sample was long enough to stabilize delta ferrite. Therefore, not only the temperature but also the heating profile are important factors when aiming to find the optimum conditions.

- It was proven, through dilatometer tests, that the amount of delta ferrite generated could be notably reduced by controlling the preheating temperature and the heating rate. Therefore, in case the heating for the NSF trials is made by induction effect instead of with the muffle furnace, NSF parts could be manufactured with a proper control of microstructural issues.

8

CONCLUSIONS

The main aim of this research work was to optimise the NSF process through the understanding of the material behaviour. To achieve this aim, an austenitic stainless steel was chosen in order to have a relevant material for industry purposes in which phase changes are not expected during the heating and the cooling.

After all the work carried out, the following conclusions can be drawn:

Thermomechanical behaviour of AISI 316

- The DSC analysis determined that the solidus temperature was around 1435°C, thus establishing the optimum temperature for NSF process around 0.9-0.95 times this value. These results were compared with FactSage® simulations showing good agreement. The analysis also showed that under equilibrium conditions delta ferrite tended to appear around 1400°C. The characterization of the appearance of delta ferrite is of great interest to understand material behaviour under NSF conditions and it could appear at lower temperatures under no-equilibrium conditions.
- The heating rate was proven to have an influence on flow stress behaviour. On the one hand, using the slowest heating rate (the commercial one), higher initial grain sizes were obtained being 55µm. On the other hand, this heating rate also allowed delta ferrite to have more time to nucleate in austenite grain boundaries. Both issues would cause a softening on the flow stress, which was observed to be around 15%. It is worth highlighting that although the heating profile was demonstrated to play a relevant role, it was not possible to be modified for the NSF trials as the commercial heating profile was defined based on a thermocouple placed in the bulk of the billet into the muffle furnace.
- The characterization of the flow stress behaviour under extreme conditions representative of the NSF process was proven to be needed as no research work was found reaching these extreme temperatures making extrapolation necessary. For instance, the flow stress law included in Forge NXT® software was proven to fail when moving up to high strain rates and temperatures. After optimising the flow stress parameters including the NSF conditions in the analysis, the prediction error was reduced by more than half taking into account all the conditions.
- Constitutive parameters were obtained according to Arrhenius equation to reproduce recrystallization behaviour. In general, the obtained parameters showed good

agreement with those reported in the literature. Nevertheless, it should be highlighted the activation energy, although it was close to the values found in the literature, was around 20% higher. This is assumed to be due to the formation of delta ferrite and, therefore, it can be stated that delta ferrite hampers recrystallization to take place as more energy would be needed to start the recrystallization process.

- After determining the onset for recrystallization for all the conditions a clear change in trend for low values of Z was identified, that is under conditions representative of the NSF process. This change was assumed to be due to delta ferrite formation, observed through microstructure measurements under all these conditions, proving that extrapolation to NSF conditions fails due to the change on material behaviour associated with the effect of delta ferrite phase.

Recrystallization analysis

- In contrast to what it would be expected, the grain size after heating the sample following the commercial heating profile, tended to decrease when the temperature was higher than 1300°C as delta ferrite influences grain growth kinetics (Zener pinning effect). In addition, microhardness increased over this temperature following the opposite trend. This finding is of great interest as these are the temperatures at which the NSF process works and the possible presence of delta ferrite shall be taking into account when looking for the optimum process window.
- The occurrence of dynamic recrystallization, analytically determined in Chapter 5, was experimentally validated. It was observed that when the test was stopped at 0.12 of strain, no recrystallization occurred. On the contrary, at 0.4 of strain smaller grain sizes were observed thanks to the recrystallization process.
- After proving the occurrence of DRX, the possibility of having metadynamic recrystallization was studied and it was observed to not occur. The analysis was made by comparing the microstructures directly obtained at 0.4 of strain with samples subjected to a certain holding time after being deformed up to 0.4 of strain. Higher grain sizes were observed due to this holding time.
- Recrystallization was studied in samples subjected to the commercial heating profile. In general, under NSF conditions, it can be stated that recrystallized microstructures were obtained as the final grain sizes were notably lower than the initial ones. However, it was also observed that the grain sizes remained almost constant (around 37μm) with the temperature, in contrast to what it could be expected. As the heating rate was slow, there was enough time for delta ferrite to nucleate and precipitate along austenite grain boundaries, having a negative impact on recrystallization.

Lifting gear component analysis

- First, the capacity for the NSF process of manufacturing austenitic stainless steel complex parts was proven. Then, a lifting gear component was manufactured at two different temperatures to understand the process and to analyse it microstructurally. Numerical simulations proved that the conditions reached were enough to ensure recrystallization to occur. The results were compared with those from the thermomechanical simulation but no clear agreement was found between them as the microstructure strongly varies along the part because of the variability of the reached conditions.
- After modifying the thermal exchange factor in the simulation, it was observed that some zones of the part could be cooled up to 1300°C (for the trial at 1370°C). It was observed that the microstructures on the surface after the NSF trial were closer to those obtained from the Gleeble at 1200°C and 1300°C but for the samples heated with the fastest heating rate. This highlights the relevance of the heating profile on the process.
- It is widely known that delta ferrite could negatively influence the performance of the final part. Therefore, the aim of testing two different temperatures was to look for reducing the amount of delta ferrite formed. However, due to the high temperatures and the slow heating rate, together with the holding time, it was proven to be formed under both conditions, not observing clear differences. Thus, not only the temperature but also the heating rate are important factors to ensure recrystallization and to obtain a part with proper material behaviour. The influence of the preheating temperature and the heating profile was proven through dilatometer tests and it was observed that with faster heating rates microstructures with lower amount of delta ferrite were obtained, thus leading to smaller grain sizes in the final microstructure.
- Aiming to look for the optimum process window, experimental parts were manufactured at 1330°C and 1370°C looking for a reduction on the delta ferrite phase in the 1330°C case based on the heating results shown in Section 6.1. However, no remarkable differences in the microstructure were observed under both conditions. This was assumed to be due to the fact that, although the temperature was lower, the holding time to ensure temperature homogeneity was too high facilitating the stabilization of the delta ferrite phase, explaining these slight differences.

9

FUTURE LINES

The aim of this dissertation started with the research work carried out first, by Lozares, 2013, who initiated the research of forging high melting point alloys at very high temperatures near the solidus and continued by Plata, 2018 who demonstrated the capacity for the NSF process of manufacturing steel parts with different advantages as has been summarized in previous chapters. However, in spite of all the efforts made in the past, there still was a lack of knowledge to explain why this process works.

On this basis, after this dissertation different attempts were made aiming to fill the aforementioned gap with a special focus on material behaviour through thermomechanical analysis and microstructural evolution. It was found, as stated in Chapter 8, that NSF is a promising manufacturing process to make stainless steel parts. However, an optimum process window needs to be defined taking into account not only mechanical aspects such as the filling and the shape but also aiming to obtain the best final microstructure. It was found that controlling the heating rate and the temperature could reduce to an acceptable amount the delta ferrite which could be formed during the heating and the deformation process, leading to, in principle, better microstructures in terms of grain sizes and delta ferrite fraction.

Therefore, a number of new research questions have arisen and further research in the following lines could be helpful to understand the NSF process in greater depth:

- It was demonstrated that material characterization under NSF conditions is necessary not only for microstructural issues but also for numerical purposes. During this work, the flow stress behaviour of the material was characterized and modelled according to the Hansel-Spittel equation. In a preliminary stage, thanks to the optimization carried out, the prediction error was reduced by more than half. It would be of great interest to carry out an in depth characterization to develop a robust model covering NSF conditions.

- All the samples were preheated up to 1370°C in order to have the same initial microstructure prior to deformation and to be representative of the NSF process. However, due to the slow heating rate, delta ferrite had enough time to nucleate and, depending on the testing temperature, it could not be totally diluted. Therefore, the influence of the heating rate and the preheating temperature were proven to be key factors in order to define the optimum process window as it is widely known that delta ferrite could have a detrimental effect on mechanical properties. Thus, although traditionally the heating of the NSF trials was made in a muffle furnace, it would be of great interest to test other heating techniques looking for faster heating

rates, ensuring the thermal homogeneity of the billet, aiming to reduce the delta ferrite.

- Apart from being detrimental in austenitic stainless steels, delta ferrite makes it difficult for recrystallization to occur and also prevents grain growth under specific conditions. Thus, it would be necessary to look for the optimum conditions which would make NSF possible, looking for a compromise between process conditions and the formation of delta ferrite which would negatively influence the properties of the NSF part.

- Based on the results reported by the numerical simulation it would be key to characterize the thermal exchange coefficient between the billet and the dies. This parameter has a notable impact on the temperature of the part during the process, making the surface to be substantially cooler than the bulk. These differences in temperature (and heating and cooling rate) could be remarkable in terms of microstructural issues. Therefore, it would be interesting to look for a way to characterize this thermal exchange coefficient in order to have a deeper knowledge of the temperature during the process.

- All the work was carried out for AISI 316. It would be of great interest to test the possibility of extrapolating the knowledge to other steel grades. However, it would be necessary to develop similar tests campaigns to do so (together with numerical simulations) in order to test whether the generated knowledge could be applied to other steel families.

10

POSSIBILITIES OF THE NSF PROCESS

As has been stated in Chapter 9, in spite of the efforts made to understand more in depth the reasons which lead the NSF process to work, new questions have arisen as a result of all the work developed.

For instance, all the work carried out was focused on AISI 316 and it would be of great interest to test whether the knowledge developed could be extrapolated to other material or not. In addition, the preheated temperature and the heating rate were found to be two main factors to be controlled during NSF process.

Therefore, together with all the comprehensive microstructural analysis of the AISI 316 subjected to NSF conditions presented in previous chapters, an analysis of the possibilities of the NSF process to manufacture other stainless steel parts and bimetal parts was also carried out to complete the findings of this work.

10.1 SPINDLE GEOMETRY

In a preliminary stage, the analysis of the results was focused on mechanical issues such as filling capability, force limit constraints and obtention of the final shape. Different conditions of stroke rate were also tested. This preliminary study will show the real possibility of using NSF process with austenitic stainless steel in more complex parts.

The spindle is responsible for connecting the wheel assembly to the steering system which rotates between the upper and lower frames. Moreover, the spindle works as the frame where the brake calliper is fixed. In order to support the vehicle weight, the component needs to be strong and durable, that is why it is forged. This R spindle weighs around 3 kg (see Figure 10.1). This geometry was chosen to carry out a preliminary analysis as it has shown promising results for manufacturing with other steel grades as it has been reported by Lozares et al., 2020 and Plata et al., 2020.

Thus, the purpose of these tests is to demonstrate the ability of NSF to fabricate other stainless steel parts and to compare experimental and numerical results. Different tests were carried out at dissimilar stroke rates in order to analyse the effect of this parameter on the industrial performance of the process at a temperature of 1370°C. The two stroke rates tested were 50% and 5% of the maximum. The billet dimensions were 95 mm in height and 70 mm in diameter.

The numerical forces were compared with the experimental ones as shown in Figure 10.2. The maximum load recorded for 50% of the maximum stroke rate was 296 tonnes. However, at 5% of the maximum stroke rate, the deformation cycle was incomplete and the load could not be registered. The manufactured parts appear in Figure 10.3.

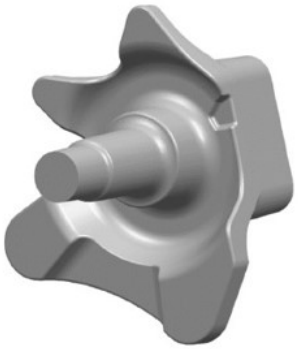

Figure 10.1: CAD of the R spindle (Plata, 2018)

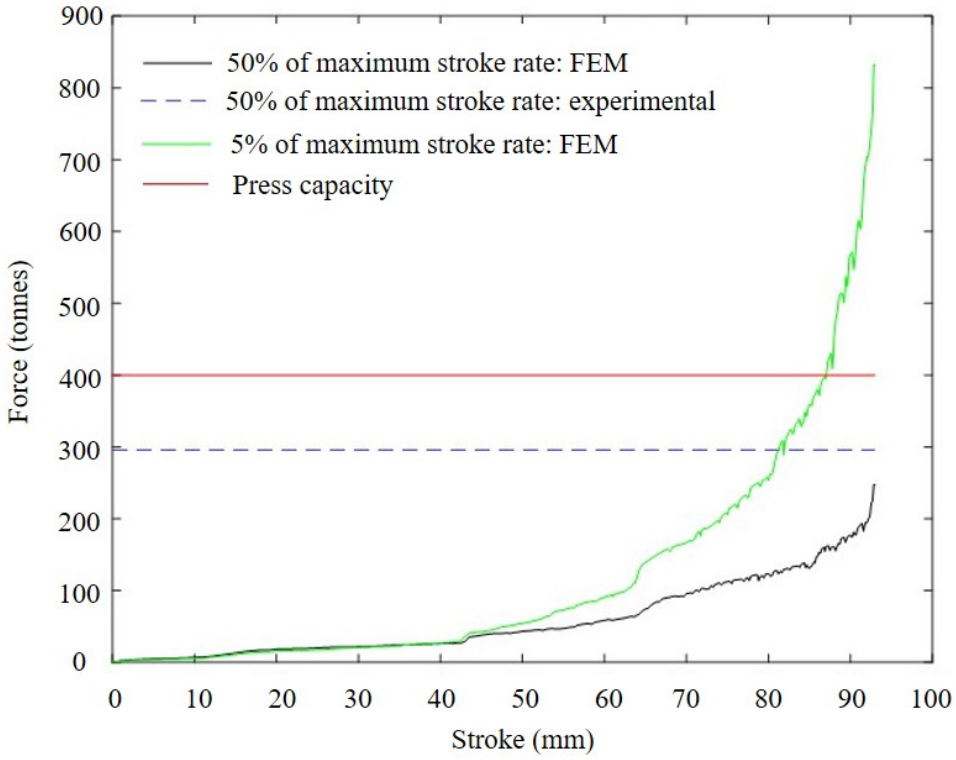

Figure 10.2: Comparison between FEM and experimental forces

As can be seen, the FEM model was able to predict that under 5% of the maximum stroke rate the press would not be capable of filling the cavity as more than 800 tonnes would be needed, which is more than two times the press capacity. In contrast, at 50% of the maximum stroke rate, both results are in agreement.

Figure 10.3: NSF components: (a) 5% (b) 50% of maximum stroke rate

As a preliminary study, the microstructure of the final part was briefly analysed and compared with the one from the material as received and quenched after being heated up to 1370°C.

First of all, the received material was analysed in two directions (radial and longitudinal). Then, the billet was heated up to 1370°C and quenched in order to analyse the microstructure just before deformation. Finally, different locations of the spindle were analysed in the axle zone and in an internal cross section. To reveal the microstructure, a reactive composed of 10 g of $FeCl_3$ hexahydrate, 100 mL of HCl and 100 mL of ethanol was used (see Figure 10.4). In the received material no significant differences were found between the locations analysed, that is why only one image is shown in Figure 10.4. The same behaviour was observed in the case of the quenched material.

It is worth noting the presence of delta ferrite in the quenched sample as Figure 10.5 shows. Furthermore, the NSF microstructure presents a grain refinement with the presence of delta ferrite. In addition, a high amount of manganese sulphides have been observed, whose shape follows the deformation direction.

To carry out a more in depth study of these elements, a SEM analysis was done. Figure 10.6 shows the presence of manganese sulphides (a) and delta ferrite (b) at 2000X and 3.0 of spot size.

Therefore, this preliminary study showed that NSF process is capable of manufacturing other austenitic stainless steel parts just considering mechanical issues related to this process such as temperature, filling and shape obtention, and grain refinement was observed under these conditions proving that recrystallization could play a role.

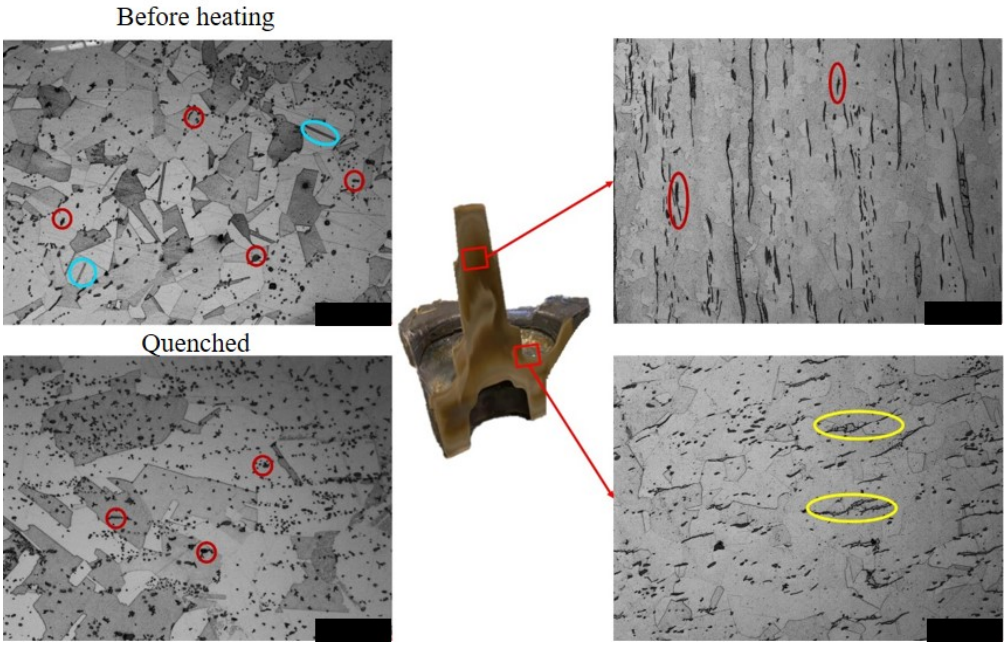

Figure 10.4: Microstructures before and after deformation: manganese sulphides (red), twin bands (blue) and delta ferrite (yellow). Scale bar: 100µm

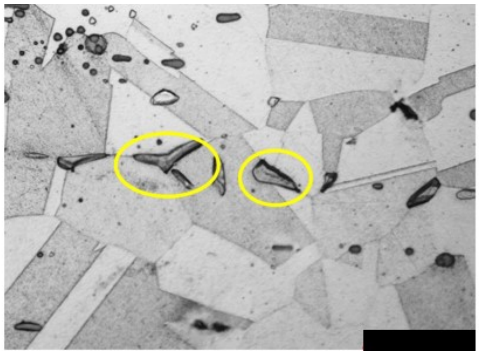

Figure 10.5: Microstructures after heating the material: delta ferrite (yellow). Scale bar: 50µm

10.2 BIMETAL COMPLEX PART

Apart from reaching complex shape parts, NSF process presents other advantages thanks to the extreme conditions of temperature, pressure and strain. Among all, one which is not widely studied is the chance of manufacturing bimetal parts. This would avoid the necessity of processes such as friction welding or diffusion bonding (Cheepu and Che, 2020; Slater et al., 2020), which are mainly restricted to simple geometries.

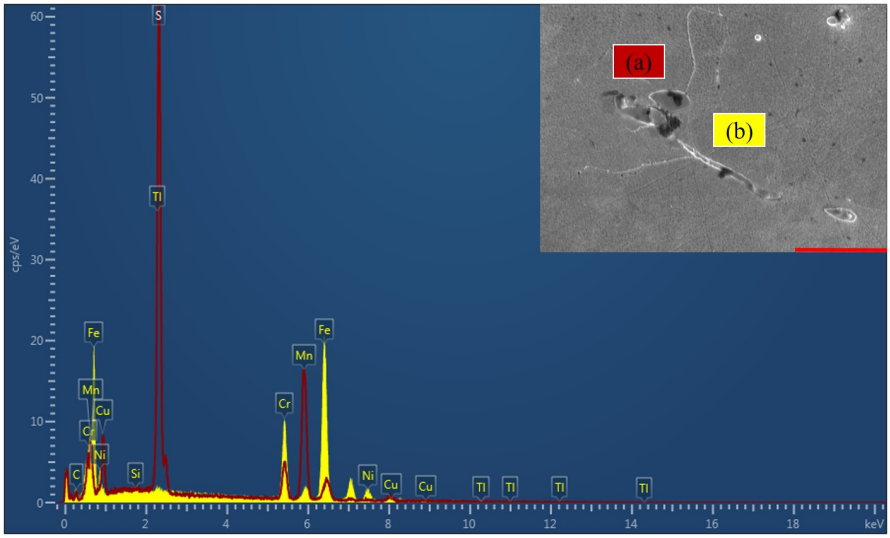

Figure 10.6: SEM analysis of MnS and delta ferrite (Scale bar: 20µm)

The two materials to be joined were AISI 304 and 42CrMo4. The solidus temperatures of both materials to define the temperature working window were around 1395 and 1425°C. That is why, the NSF temperature was chosen to be 1370°C.

To observe macro-differences in terms of composition, X-ray fluorescence (XRF) evaluation was carried out with a Bruker Tornado M4 applying 100 mm step size with a 100 ms dwell time. Also, electron microscopy was used using a FEI NovaNanoSEM 450 Scanning Electron Microscope (SEM) equipped with an Oxford X-max 50 X-Ray detector (EDX). The microstructure of the interface was then etched using different chemical etching. Nital was used to reveal the microstructure in the zone of 42CrMo4 and a reactive composed of $FeCl_3$ hexahydrate, HCl and ethanol in the same proportions as in previous section to reveal the stainless steel zone.

The load needed to manufacture the part was 277 tonnes, which is lower than the maximum one achievable. In addition, this load is substantially lower than the typical one employed on conventional forging, which could be around 2500 tonnes (Plata, 2018). The manufactured component can be seen in Figure 10.7-a. Just with a quick optical observation, it can be seen that the part was properly manufactured, both materials being joined. To ensure this, Figure 10.7-b shows the XRF map taken, in which, it can be seen that the AISI304 covers the outside of the component, which offers corrosion resistance to the final part together with a cost reduction thanks to the lower amount of stainless steel used.

A microstructural analysis was carried out to verify the joining between the two materials (see Figure 10.8). In Region 1, it can be seen a much smoother interface due to the unidirectional compression, which mainly governs in this region based on the Mn flow (see Figure 10.8-a). In contrast, in Region 2 the interface seems to be serrated (see

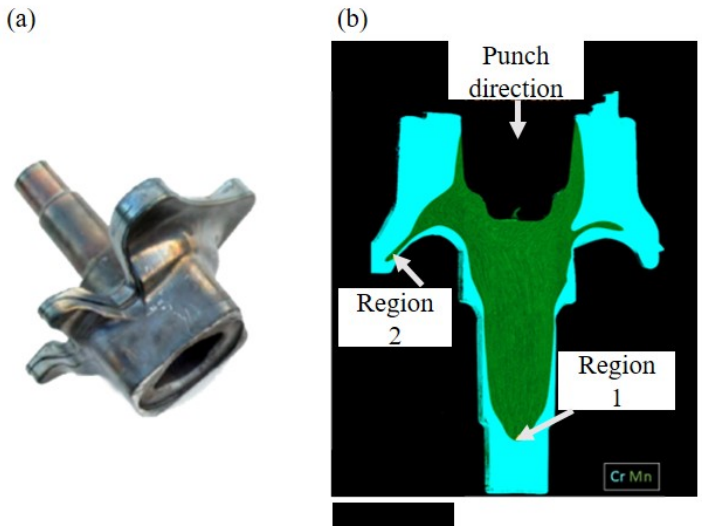

Figure 10.7: (a) Manufactured component (b) XRF analysis of the component. Scale bar: 3 cm (Adapted from Slater et al., 2020)

Figure 10.8-b) due to the shear stresses at which it is exposed. Nevertheless, it seems to be that no clear defects were formed during the process in both regions, with no porosity observable throughout the part.

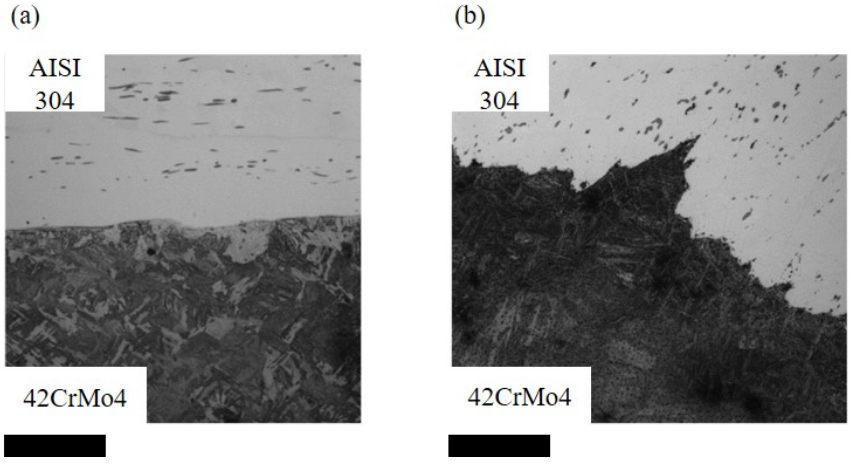

Figure 10.8: (a) Region 1 (b) Region 2. Scale bar: 100µm. (Adapted from Slater et al., 2020)

To corroborate the joining of the both steels, an EDX analysis was done (see Figure 10.9). Around 3 mm of cross diffusion prove this joining.

Therefore, this preliminary analysis shows the capacity for manufacturing bimetal complex parts through NSF process, allowing parts not achievable by traditional forming to be obtained, and needing much less force.

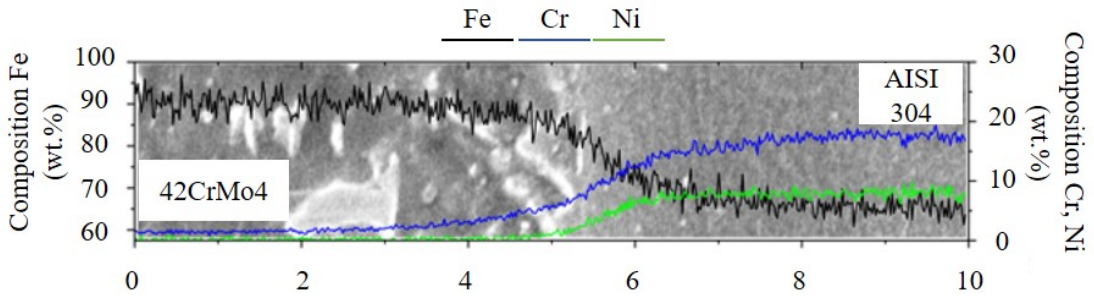

Figure 10.9: EDX analysis of the interface between the two join materials (Adapted from Slater et al., 2020)

BIBLIOGRAPHY

Aksenov, Sergey (2009). "Matematické modelování toku kovu a vỳvoje mikrostruktury při válcování v kalibrech." In: *Disertační práce. Vysoká škola báňská - Technická univerzita Ostrava.*

Anoop, CR et al. (2020). "Development and Validation of Processing Maps for Hot Deformation of Modified AISI 321 Austenitic Stainless Steel." In: *Materials Performance and Characterization* 9.2.

Ayers, Lauren Juliet (2012). "The hardening of Type 316L stainless steel welds with thermal aging." PhD thesis. Massachusetts Institute of Technology.

Azpilgain, Zigor et al. (2006). "Semisolid forging of 7000 series aluminum alloys." In: *Solid State Phenomena*. Vol. 116. Trans Tech Publ, pp. 758–761.

Babu, K Arun et al. (2018). "Hot-workability of super-304H exhibiting continuous to discontinuous dynamic recrystallization transition." In: *Materials Science and Engineering: A* 734, pp. 269–280.

Babu, K Arun et al. (2021). "Implication of initial grain size on DRX mechanism and grain refinement in super-304H SS in a wide range of strain rates during large-strain hot deformation." In: *Materials Science and Engineering: A*, p. 142269.

Bai, Yuanli and Tomasz Wierzbicki (2008). "A new model of metal plasticity and fracture with pressure and Lode dependence." In: *International journal of plasticity* 24.6, pp. 1071–1096.

Balachandran, G and V Balasubramanian (2013). "Stainless steel processing to meet advanced applications." In: *Advanced Materials Research*. Vol. 794. Trans Tech Publ, pp. 135–158.

Bao, Siqian et al. (2011). "Recrystallization behavior of a Nb-microalloyed steel during hot compression." In: *Applied Mathematical Modelling* 35.7, pp. 3268–3275.

Bayramin, Berkay, Caner Şimşir, and Mert Efe (2017). "Dynamic strain aging in DP steels at forming relevant strain rates and temperatures." In: *Materials Science and Engineering: A* 704, pp. 164–172.

Becker, Eric et al. (2010). "Impact of experimental conditions on material response during forming of steel in semi-solid state." In: *Journal of Materials Processing Technology* 210.11, pp. 1482–1492.

Bell, Colin et al. (2019). "Enabling sheet hydroforming to produce smaller radii on aerospace nickel alloys." In: *International Journal of Material Forming* 12.5, pp. 761–776.

Biswal, Smrutiranjan and S Tripathy (2021). "Effect of Process Variables in Closed Die Hot Forging Process: A Review." In: *Current Advances in Mechanical Engineering*, pp. 899–907.

Blanco, A et al. (2010). "Rheological characterization of A201 aluminum alloy." In: *Transactions of Nonferrous Metals Society of China* 20.9, pp. 1638–1642.

Calamaz, Madalina, Dominique Coupard, and Franck Girot (2008). "A new material model for 2D numerical simulation of serrated chip formation when machining titanium alloy Ti–6Al–4V." In: *International Journal of Machine Tools and Manufacture* 48.3-4, pp. 275–288.

Chadha, Kanwal, Davood Shahriari, and Mohammad Jahazi (2018). "An Approach to Develop Hansel–Spittel Constitutive Equation during Ingot Breakdown Operation of Low Alloy Steels." In: *Frontiers in Materials Processing, Applications, Research and Technology*. Springer, pp. 239–246.

Cheepu, Muralimohan and Woo Seong Che (2020). "Influence of friction pressure on microstructure and joining phenomena of dissimilar joints." In: *Transactions of the Indian Institute of Metals* 73.6, pp. 1455–1460.

Chen, Gang, Zhiming Du, and Yuansheng Cheng (2012). "Effect of mechanical conditions on the microstructures and mechanical properties of thixoformed AlCuSiMg alloy." In: *Materials & Design* 35, pp. 774–781.

Cho, Sang-Hyun and Yeon-Chul Yoo (2001a). "Hot rolling simulations of austenitic stainless steel." In: *Journal of materials science* 36.17, pp. 4267–4272.

— (2001b). "Metadynamic recrystallization of austenitic stainless steel." In: *Journal of materials science* 36.17, pp. 4279–4284.

Cho, W Gi and CG Kang (2000). "Mechanical properties and their microstructure evaluation in the thixoforming process of semi-solid aluminum alloys." In: *Journal of Materials Processing Technology* 105.3, pp. 269–277.

Cho, WG and CG Kang (2001). "An experimental study on thixoforging of semi-solid materials and solutions for avoiding defects." In: *Proceedings of the Institution of Mechanical Engineers, Part B: Journal of Engineering Manufacture* 215.9, pp. 1217–1227.

Curle, UA, JD Wilkins, and G Govender (2011). "Industrial semi-solid rheocasting of aluminum A356 brake calipers." In: *Advances in Materials Science and Engineering* 2011.

Dehghan-Manshadi, A, Mathew R Barnett, and PD Hodgson (2008a). "Hot deformation and recrystallization of austenitic stainless steel: Part I. Dynamic recrystallization." In: *Metallurgical and materials transactions A* 39.6, pp. 1359–1370.

— (2008b). "Recrystallization in AISI 304 austenitic stainless steel during and after hot deformation." In: *Materials Science and Engineering: A* 485.1-2, pp. 664–672.

Dehghan-Manshadi, A and PD Hodgson (2008). "Effect of δ-ferrite co-existence on hot deformation and recrystallization of austenite." In: *Journal of materials science* 43.18, pp. 6272–6277.

Douglas, Richard and David Kuhlmann (2000). "Guidelines for precision hot forging with applications." In: *Journal of Materials Processing Technology* 98.2, pp. 182–188.

Drozd, Kamil et al. (2011). "Study of development of strain in plane strain compression test." In: *International Conference on Metallurgy and Materials METAL*.

Dupin, Eduardo EV, Akira Yana, and Jun Yanag. (2014). "Modelling Static and Dynamic Kinetics of Microstructure Evolution in Type 316 Stainless Steel During Hot Rolling." In: *International Manufacturing Science and Engineering Conference*. Vol. 45813. American Society of Mechanical Engineers, V002T02A071.

El Wahabi, Mohamed et al. (2005). "Effect of initial grain size on dynamic recrystallization in high purity austenitic stainless steels." In: *Acta materialia* 53.17, pp. 4605–4612.

Faini, F, A Attanasio, and E Ceretti (2018). "Experimental and FE analysis of void closure in hot rolling of stainless steel." In: *Journal of Materials Processing Technology* 259, pp. 235–242.

Fan, Z (2002). "Semisolid metal processing." In: *International materials reviews* 47.2, pp. 49–85.

Flemings, MC, RG Riek, and KP Young (1976). "Rheocasting." In: *Materials Science and Engineering* 25, pp. 103–117.

Flemings, Merton C (1991). "Behavior of metal alloys in the semisolid state." In: *Metallurgical transactions A* 22.5, pp. 957–981.

Fu, Bin et al. (2020). "Strength and strain-hardening enhancement by generating hard delta-ferrite in twinning-induced plasticity steel." In: *Materials Science and Technology* 36.7, pp. 827–834.

Gao, Pengfei et al. (2019). "Formation mechanisms and rules of typical types of folding defects during die forging." In: *The International Journal of Advanced Manufacturing Technology* 104.1-4, pp. 1603–1612.

Garcia, C, R Ortubay, and Z Azpilgain (2006). "Accuracy in a 400 ton Fagor servomotor driven mechanical press." In: *The 2nd international conference on accuracy in forming technology, Chemnitz*, pp. 13–15.

Ghasemi, R, Behrooz Beidokhti, and M Fazel-Najafabadi (2018). "Effect of delta ferrite on the mechanical properties of dissimilar ferritic-austenitic stainless steel welds." In: *Archives of Metallurgy and Materials* 63.

Ghazani, M Shaban and B Eghbali (2018). "Characterization of the hot deformation microstructure of AISI 321 austenitic stainless steel." In: *Materials Science and Engineering: A* 730, pp. 380–390.

Gronostajski, Zbigniew et al. (2017). "The effect of the strain rate on the stress-strain curve and microstructure of AHSS." In: *Journal of Materials Processing Technology* 242, pp. 246–259.

Guo, Baofeng et al. (2012). "Research on flow stress during hot deformation process and processing map for 316LN austenitic stainless steel." In: *Journal of Materials Engineering and Performance* 21.7, pp. 1455–1461.

Hawryluk, Marek and Joanna Jakubik (2016). "Analysis of forging defects for selected industrial die forging processes." In: *Engineering Failure Analysis* 59, pp. 396–409.

Hirt, Gerhard and Reiner Kopp (2009). *Thixoforming: Semi-solid metal processing*. John Wiley & Sons.

Höhne, Günther, Wolfgang F Hemminger, and H-J Flammersheim (2013). *Differential scanning calorimetry*. Springer Science & Business Media.

Hu, Xin et al. (2021). "Effect of Pre-deformation on Hot Workability of Super Austenitic Stainless Steel." In: *Journal of Materials Research and Technology*.

Huang, Yung-Chien et al. (2019). "A study on the Hall–Petch relationship and grain growth kinetics in FCC-structured high/medium entropy alloys." In: *Entropy* 21.3, p. 297.

Jafari, M. and A. Najafizadeh (2008). "Comparison between the methods of determining the critical stress for initiation of dynamic recrystallization in 316 stainless steel." In:

Jafari, M, A Najafizadeh, and J Rasti (2007). "Dynamic recrystallization by necklace mechanism during hot deformation of 316 stainless steel." In:

Janudom, S et al. (2010). "Feasibility of semisolid die casting of ADC12 aluminum alloy." In: *Transactions of Nonferrous Metals Society of China* 20.9, pp. 1756–1762.

Johnson, Gordon R and William H Cook (1983). "A constitutive model and data for metals subjected to large strains, high strain rates and high temperatures." In: *Proceedings of the 7th International Symposium on Ballistics*. Vol. 21. 1. The Netherlands, pp. 541–547.

Jonas, John J. and Evgueni I. Poliak (2003). "The Critical Strain for Dynamic Recrystallization in Rolling Mills." In: *Materials Science Forum* 426-432, pp. 57–66. DOI: 10.4028/www.scientific.net/msf.426-432.57.

Kajberg, Jörgen and K-G Sundin (2013). "Material characterisation using high-temperature Split Hopkinson pressure bar." In: *Journal of Materials Processing Technology* 213.4, pp. 522–531.

Kang, J et al. (2017). "Hot Deformation Characteristics of 304 Stainless Steels by Tensile Test." In: *International Journal of Applied Engineering Research* 12.22, pp. 12415–12420.

Kapranos, P, DH Kirkwood, and CM Sellars (1993). "Semi-solid processing of tool steel." In: *Le Journal de Physique IV* 3.C7, pp. C7–835.

Kareh, KM et al. (2017). "Dilatancy in semi-solid steels at high solid fraction." In: *Acta Materialia* 125, pp. 187–195.

Kim, Sung-Il, Youngseog Lee, and Byoung-Lok Jang (2003). "Modeling of recrystallization and austenite grain size for AISI 316 stainless steel and its application to hot bar rolling." In: *Materials Science and Engineering: A* 357.1-2, pp. 235–239.

Kim, Sung-Il and Yeon-Chul Yoo (2001). "Dynamic recrystallization behavior of AISI 304 stainless steel." In: *Materials Science and Engineering:* 311.1-2, pp. 108–113.

Kirkwood, DH (1994). "Semisolid metal processing." In: *International materials reviews* 39.5, pp. 173–189.

Klančnik, Grega, Jožef Medved, and Primož Mrvar (2010). "Differential thermal analysis (DTA) and differential scanning calorimetry (DSC) as a method of material investi-

gation Diferenčna termična analiza (DTA) in diferenčna vrstična kalorimetrija (DSC) kot metoda za raziskavo materialov." In: *RMZ–Materials and Geoenvironment* 57.1, pp. 127–142.

Koç, Muammer, Sasawat Mahabunphachai, and Eren Billur (2011). "Forming characteristics of austenitic stainless steel sheet alloys under warm hydroforming conditions." In: *The International Journal of Advanced Manufacturing Technology* 56.1-4, pp. 97–113.

Kumar, Santosh et al. (2016). "Hot deformation and microstructural characteristics of nitrogen enhanced 316L stainless steel." In: *Key Engineering Materials*. Vol. 716. Trans Tech Publ, pp. 317–322.

Lan, Liangyun, Wei Zhou, and R.D.K. Misra (2019). "Effect of hot deformation parameters on flow stress and microstructure in a low carbon microalloyed steel." In: *Materials Science and Engineering: A* 756, pp. 18–26. DOI: 10.1016/j.msea.2019.04.039.

Lecomte-Beckers, Jacqueline et al. (2007). "Study of the liquid fraction and thermophysical properties of semi-solid steels and application to the simulation of inductive heating for thixoforming." In: *Advanced Methods in Material Forming*. Springer, pp. 321–347.

Lei, Bingwang et al. (2019). "Constitutive Analysis on High-Temperature Flow Behavior of 3Cr-1Si-1Ni Ultra-High Strength Steel for Modeling of Flow Stress." In: *Metals* 9.1, p. 42.

Lennon, AM and KT Ramesh (2004). "The influence of crystal structure on the dynamic behavior of materials at high temperatures." In: *International journal of Plasticity* 20.2, pp. 269–290.

Li, Longfei et al. (2017). "Influence of Mold Temperature on Microstructure and Shrinkage Porosity of the A357 Alloys in Gravity Die Casting." In: *Chinese Materials Conference*. Springer, pp. 793–801.

Lin, YC, Ming-Song Chen, and Jue Zhong (2008). "Constitutive modeling for elevated temperature flow behavior of 42CrMo steel." In: *Computational Materials Science* 42.3, pp. 470–477.

Lin, YC et al. (2016). "A new method to predict the metadynamic recrystallization behavior in a typical nickel-based superalloy." In: *Applied Physics A* 122.6, pp. 1–14.

Liss, Klaus-Dieter et al. (2009). "In situ observation of dynamic recrystallization in the bulk of zirconium alloy." In: *Advanced engineering materials* 11.8, pp. 637–640.

Liu, X G et al. (2013). "Study on hot deformation behaviour of 316LN austenitic stainless steel based on hot processing map." In: *Materials Science and Technology* 29.1, pp. 24–29. DOI: 10.1179/1743284712y.0000000083.

Liu, Yin Gang, Miao Quan Li, and Xiao Ling Dang (2013). "Effect of heating temperature and heating rate on Austenite in the heating process of 300M steel." In: *Materials Science Forum*. Vol. 749. Trans Tech Publ, pp. 260–267.

López, B and JM Rodriguez-Ibabe (2012). "Recrystallisation and grain growth in hot working of steels." In: *Microstructure Evolution in Metal Forming Processes*. Elsevier, pp. 67–113.

Loveday, MS et al. (2002). "Measuring flow stress in plane strain compression tests." In:

Lozares, Jokin (2013). "Semisolid forging of steel components for automotive industry." In:

Lozares, Jokin et al. (2020). "Near Solidus Forming (NSF): Semi-Solid Steel Forming at High Solid Content to Obtain As-Forged Properties." In: *Metals* 10.2, p. 198.

Mandal, Sumantra et al. (2009). "Constitutive equations to predict high temperature flow stress in a Ti-modified austenitic stainless steel." In: *Materials Science and Engineering: A* 500.1-2, pp. 114–121.

Marchattiwar, A et al. (2013). "Dynamic recrystallization during hot deformation of 304 austenitic stainless steel." In: *Journal of materials engineering and performance* 22.8, pp. 2168–2175.

Mataya, Martin C et al. (2003). "Hot working and recrystallization of as-cast 316L." In: *Metallurgical and materials transactions A* 34.8, pp. 1683–1703.

McQueen, HJ, WA Wong, and JJ Jonas (1967). "Deformation of aluminium at high temperatures and strain rates." In: *Canadian Journal of Physics* 45.2, pp. 1225–1234.

McQueen, HJ et al. (1995). "Hot working characteristics of steels in austenitic state." In: *Journal of Materials Processing Technology* 53.1-2, pp. 293–310.

Mirzadeh, H et al. (2011). "Hot deformation behavior of a medium carbon microalloyed steel." In: *Materials Science and Engineering: A* 528.10-11, pp. 3876–3882.

Mirzadeh, Hamed, Jose Maria Cabrera, and Abbas Najafizadeh (2011). "Constitutive relationships for hot deformation of austenite." In: *Acta materialia* 59.16, pp. 6441–6448.

Mirzadeh, Hamed, Abbas Najafizadeh, and Mohammad Moazeny (2009). "Flow curve analysis of 17-4 PH stainless steel under hot compression test." In: *Metallurgical and Materials Transactions A* 40.12, p. 2950.

Mohanty, ON (2017). "Forging Grade Steels for Automotives." In: *Automotive Steels*. Elsevier, pp. 413–453.

Moradi, M et al. (2009). "Defect control and mechanical properties of thixoformed AlSi alloy." In: *Journal of Alloys and Compounds* 487.1-2, pp. 768–775.

Nafisi, Shahrooz and Reza Ghomashchi (2016). *Semi-solid processing of aluminum alloys*. Springer.

Nagira, Tomoya et al. (2014). "In situ observation of deformation in semi-solid Fe-C alloys at high shear rate." In: *Metallurgical and Materials Transactions A* 45.12, pp. 5613–5623.

Najafizadeh, A. and J. Jonas (2006). "Predicting the Critical and Stress for Initiation and of Dynamic and Recrystallization." In: *ISIJ International, Vol. 46 (2006), No. 11, pp.*

Nidheesh, PV and M Suresh Kumar (2019). "An overview of environmental sustainability in cement and steel production." In: *Journal of cleaner production* 231, pp. 856–871.

Nisbett, Edward G (2005). *Steel forgings: design, production, selection, testing, and application*. ASTM International.

Nkhoma, Richard KC, Charles W Siyasiya, and Waldo E Stumpf (2014). "Hot workability of AISI 321 and AISI 304 austenitic stainless steels." In: *Journal of Alloys and Compounds* 595, pp. 103–112.

Omar, MZ et al. (2005). "Thixoforming of a high performance HP9/4/30 steel." In: *Materials Science and Engineering: A* 395.1-2, pp. 53–61.

Pandre, Sandeep et al. (2019). "Flow stress behavior, constitutive modeling, and microstructural characteristics of DP 590 steel at elevated temperatures." In: *Journal of Materials Engineering and Performance* 28.12, pp. 7565–7581.

Paquette, Arthur et al. (2021). "On the evolution of microstructure and mechanical properties of type 316 austenitic stainless steel during ingot to billet conversion process." In:

Park, N et al. (2013). "Effect of austenite grain size on kinetics of dynamic ferrite transformation in low carbon steel." In: *Scripta Materialia* 68.8, pp. 611–614.

Plata, Gorka (2018). "Semi-Solid Forging of Steels: New insights into material behaviour evolution and industrialisation." PhD thesis. Mondragon University.

Plata, Gorka et al. (2020). "Preliminary Study on the Capability of the Novel Near Solidus Forming (NSF) Technology to Manufacture Complex Steel Components." In: *Materials* 13.20, p. 4682.

Poliak, E.I. and J.J. Jonas (2003a). "Critical Strain and for Dynamic and Recrystallization in Variable and Strain and Rate Hot and Deformation." In: *ISIJ International*. Vol. 43. 5.

— (2003b). "Initiation of Dynamic and Recrystallization in Constant and Strain Rate and Hot Deformation." In: *ISIJ International, Vol. 43 (2003), No. 5, pp.*

Price, Lynn et al. (2002). "Energy use and carbon dioxide emissions from steel production in China." In: *Energy* 27.5, pp. 429–446.

Puettgen, Wolfgang et al. (2007). "Thixoforming of steels–a status report." In: *Advanced Engineering Materials* 9.4, pp. 231–245.

Radionova, Liudmila V et al. (2022). "Study on the Hot Deformation Behavior of Stainless Steel AISI 321." In: *Materials* 15.12, p. 4057.

Rathi, Mahendra G and Nilesh A Jakhade (2014). "An Overview of Forging Processes with their defects." In: *International Journal of Scientific and Research Publications* 4.6, pp. 1–7.

Razali, Mohd Kaswandee, Missam Irani, and ManSoo Joun (2019). "General modeling of flow stress curves of alloys at elevated temperatures using bi-linearly interpolated or closed-form functions for material parameters." In: *Journal of Materials Research and Technology* 8.3, pp. 2710–2720.

Romeo, Giovanni (2019). *Elements of Numerical Mathematical Economics with Excel: Static and Dynamic Optimization*. Academic Press.

Ryan, ND and HJ McQueen (1990a). "Comparison of dynamic softening in 301, 304, 316 and 317 stainless steels." In: *High Temperature Technology* 8.3, pp. 185–200.

Ryan, N.D. and H.J. McQueen (1990b). "Dynamic Softnening Mechanisms in 304 Austenitic Stainless Steel." In: *Canadian Metallurgical Quarterly, Vol. 29, No.2, , 1990*. Vol. 29. 2, pp. 147–162.

Sakai, Taku et al. (2014). "Dynamic and post-dynamic recrystallization under hot, cold and severe plastic deformation conditions." In: *Progress in Materials Science* 60, pp. 130–207. DOI: 10.1016/j.pmatsci.2013.09.002.

Samantaray, Dipti et al. (2011a). "Analysis and mathematical modelling of elevated temperature flow behaviour of austenitic stainless steels." In: *Materials Science and Engineering: A* 528.4-5, pp. 1937–1943.

Samantaray, Dipti et al. (2011b). "Flow behavior and microstructural evolution during hot deformation of AISI Type 316 L (N) austenitic stainless steel." In: *Materials Science and Engineering: A* 528.29-30, pp. 8565–8572.

Sellars, C Michael and WJ McTegart (1966). "On the mechanism of hot deformation." In: *Acta Metallurgica* 14.9, pp. 1136–1138.

Sellars, CM and WJM Tegart (1966). "Relationship between strength and structure in deformation at elevated temperatures." In: *Mem Sci Rev Met* 63.9.

Setyowati, VA, EWR Widodo, SA Hermanto, et al. (2019). "Normalising of 316L Stainless Steel using Temperature and Holding Time Variations." In: *IOP Conference Series: Materials Science and Engineering*. Vol. 462. 1. IOP Publishing, p. 012012.

Shaban, M. and B. Eghbali (2010). "Determination of critical conditions for dynamic recrystallization of a microalloyed steel." In: *Materials Science and Engineering: A* 527.16-17, pp. 4320–4325. DOI: 10.1016/j.msea.2010.03.086.

Shan, Zhongde et al. (2012). "Key manufacturing technology & equipment for energy saving and emissions reduction in mechanical equipment industry." In: *International Journal of Precision Engineering and Manufacturing* 13.7, pp. 1095–1100.

Slater, Carl, Nusrat Tamanna, and Claire Davis (2021). "Optimising compression testing for strain uniformity to facilitate microstructural assessment during recrystallisation." In: *Results in Materials* 11, p. 100218.

Slater, Carl et al. (2020). "A novel forming technique to coforge bimetal components into complex geometries." In: *Manufacturing Letters*.

Soleymani, S, OA Ojo, and N Richards (2015). "Effect of composition on the formation of delta ferrite in 304L austenitic stainless steels during hot deformation." In: *Journal of materials engineering and performance* 24.1, pp. 499–504.

Spencer, DB, R Mehrabian, and Merton C Flemings (1972). "Rheological behavior of Sn-15 pct Pb in the crystallization range." In: *Metallurgical and Materials Transactions B* 3.7, pp. 1925–1932.

Stornelli, Giulia et al. (2022). "Recrystallization and grain growth of AISI 904L super-austenitic stainless steel: A multivariate regression approach." In: *Metals* 12.2, p. 200.

Suker, DK et al. (2017). "Hot deformation characterization of AISI316 and AISI304 stainless steels." In: *IJMME* 17, pp. 1–14.

Sun, L et al. (2010). "Mapping microstructure inhomogeneity using electron backscatter diffraction in 316L stainless steel subjected to hot plane strain compression tests." In: *Materials Science and Technology* 26.12, pp. 1477–1486.

Sun, S, A Zhao, and Q Wu (2017). "Effect of strain rate on the work-hardening rate in high-Mn steel." In: *Materials Science and Technology* 33.11, pp. 1306–1311.

Tamanna, Nusrat, Carl Slater, and Claire Davis (2022). "Effect of Sample Geometry on Strain Uniformity and Double Hit Compression Tests for Softening Kinetics Determination." In: *steel research international*.

Taylor, A.S. and P.D. Hodgson (2011). "Dynamic behaviour of 304 stainless steel during high Z deformation." In: *Materials Science and Engineering: A* 528.9, pp. 3310–3320. DOI: 10.1016/j.msea.2010.12.093.

Tsun, Ko (1953). "The Overheating & Burning of Steel." In:

Venugopal, S, SL Mannan, and YVRK Prasad (1996). "Influence of strain rate and state-of-stress on the formation of ferrite in stainless steel type AISI 304 during hot working." In: *Materials Letters* 26.3, pp. 161–165.

Wang, Shenglong et al. (2016a). "Study on the dynamic recrystallization model and mechanism of nuclear grade 316LN austenitic stainless steel." In: *Materials characterization* 118, pp. 92–101.

— (2016b). "Study on the dynamic recrystallization model and mechanism of nuclear grade 316LN austenitic stainless steel." In: *Materials Characterization* 118, pp. 92–101. DOI: 10.1016/j.matchar.2016.05.015.

Wang, Zhiguo et al. (2021). "Transitional Behavior for Dynamic Recrystallization in Nuclear Grade 316H Stainless Steel during Hot Deformation." In: *Metallurgical and Materials Transactions A*. DOI: 10.1007/s11661-021-06520-1.

Xu, Shiguang et al. (2022). "Hot Deformation Behaviors and Dynamic Recrystallization Mechanisms of the 7mo Super-Austenitic Stainless Steel." In: *Available at SSRN 4135079*.

Zerilli, Frank J and Ronald W Armstrong (1987). "Dislocation-mechanics-based constitutive relations for material dynamics calculations." In: *Journal of applied physics* 61.5, pp. 1816–1825.

Zhang, R. H. et al. (2015). "Dynamic and Postdeformation Recrystallization of Nuclear-Grade 316LN Stainless Steel." In: *Strength of Materials* 47.1, pp. 94–99. DOI: 10.1007/s11223-015-9633-3.

Zhang, XF, H Terasaki, and Y Komizo (2011). "Correlation of delta-ferrite precipitation with austenite grain growth during annealing of steels." In: *Philosophical magazine letters* 91.7, pp. 491–497.

Zohrevand, Milad et al. (2021). “Microstructural evolutions under ultrasonic treatment in 304 and 316 austenitic stainless steels: impact of stacking fault energy.” In: *steel research international* 92.9, p. 2100041.